On the Impact of Adverse Weather Uncertainty on Aircraft Routing – Identification and Mitigation

Von der Fakultät für Mathematik und Physik
der Gottfried Wilhelm Leibniz Universität Hannover
zur Erlangung des Grades

Doktorin der Naturwissenschaften

Dr. rer. nat.

genehmigte Dissertation
von

M. Sc. Manuela Sauer

geboren am 27.12.1986 in Hannover

2015

Referent: Prof. Dr. rer. nat. Thomas Hauf

Korreferent: Prof. Dr. rer. nat. Dieter Etling

Tag der Promotion: 21. Dezember 2015

Abstract

Adverse weather poses a risk to aviation. It negatively affects safety and efficiency of operations and, thus, leads to monetary losses for aviation stakeholders. Adaptation to the weather situation so far is often reactive and on a short-term basis. Thunderstorms have been chosen as the representative adverse weather focused on in this study. They incorporate several atmospheric hazards and, consequently, require re-routings recommended by international regulations in order to prevent risk encounters.

In current procedures rather no proactive avoidance is envisaged. Diversion manoeuvres are initiated by pilots in correspondence with the air traffic controller (ATCO) in charge in reaction to storms obstructing the planned flight path. This increases the ATCO's workload. Future concepts, under elaboration in the Single European Sky ATM Research (SESAR) programme, foresee a transition from the currently operational airspace optimised handling to a four-dimensional (4D) trajectory (3D plus time) management. Routing is said to become more efficient and close to the ideal profile of the airspace user while being coordinated with the overall optimised flow. The planned 4D trajectory of a flight is shared between and agreed by all stakeholders before departure. Throughout the flight, all stakeholders will share a common view on it, get information on future positions and times which facilitates more effective planning of resources and increases predictability (SESAR JOINT UNDERTAKING 2014). The latter requires an early consideration of the atmospheric state.

Some parameters, relevant for flight performances, are better predictable than others. In case of thunderstorms, the onset is rather hard to predict because of its sensitivity to external and internal forcing conditions and its mostly stochastic occurrence. Once a cell exists, its development can be somewhat foreseen. Based on an observed cell stage, nowcast models provide short-term forecasts up to 1 to 6 hours. These forecasts are hardly ever perfect but bear an uncertainty which is analysed and quantified in this study, exemplary for the object-based nowcast product Rad-TRAM provided by German Aerospace Center (DLR) in Oberpfaffenhofen, Germany. Position and extent of each nowcasted cell are compared in four directions with respect to the cell movement to the respective later observed cell characteristics. Any deviation between nowcast and observation is assumed to represent the nowcast product uncertainty. In this study 563 individual cell cycles are analysed to determine their lead time-dependent spatial deviation which is merged into respective distributions.

Certain percentiles (e. g. the 90$^{\text{th}}$) of these distributions are then assumed to define a representative uncertainty measure for Rad-TRAM data. Nowcasted cells are then enveloped by the so determined uncertainty margin. The latter varies with direction and lead time. The new polygon defines an area that covers the respective actual cell with a certainty of 90 %. As the uncertainty margin enlarges the nowcasted cell significantly (up to more than 20 times the nowcast areas), its consideration may have substantial impact on aircraft routing and air traffic management (ATM) performance. Thus, the question arises what the best routing strategy looks like, in order to account for the available weather information and its uncertainty in an appropriate and efficient way.

To do so, the adverse weather diversion model DIVMET, developed at Leibniz Universität Hannover, is applied. Monte Carlo simulations are performed and trajectories are generated according to the first detected stage of each cell. Observational as well as nowcast information, the latter with and without application of the uncertainty margin, are used with varying update rates. Various simulation modes are then forced in subsequent model runs in order to cover several strategies that may help in identifying the best handling of weather data. Basically, the detour effects of an instant diversion initiation are compared with those arising from a postponed deviation from the planned trajectory. The understanding of consequences of each tactic regarding flight distance as a measure of ATM performance is improved.

An evaluation on whether a *wait and see* strategy is more beneficial than an instant consideration of the available nowcast is performed. An application of the latter strategy while accounting for nowcast data would facilitate efficient planning of 4D trajectories and increase predictability, at least when the nowcast is good. What is found is that consideration of the uncertainty margin reduces the risk of cell encounters to less than 10 % but for the prise of longer detours. The route is safe, at least with respect to the considered cell, but due to the limited lifetime characteristic of thunderstorm cells they very often shrink or even dissipate in the meantime. The early re-routing would not have been necessary in these cases and the flown detour is inefficient. To account for this life time uncertainty route adaptation would be an option which, when applied, should not consider uncertainty measures as these would elongate the route unnecessarily. When being limited to observational data, a deviation initiation horizon of about 30 minutes flight time distance to the storm was found to be beneficial. If being already closer to a just detected cell, an instantaneous deviation should be considered.

The results from this study will support decision makers to recognise consequences of their preferred kind of weather handling. Identification of an overall optimum is not possible, it is rather a trade-off between predictability and route efficiency.

Keywords: thunderstorm hazards, nowcast uncertainty, routing tactics, weather avoidance

Kurzzusammenfassung

Der Luftverkehr wird durch gefährdendes Wetter hinsichtlich seiner Sicherheit und Effizienz beeinflusst. Eine Anpassung der Verfahren, wie beispielsweise die Bestimmung einer Ausweichroute im Fall von Gewittern, erfolgt zumeist reaktiv und kurzfristig. Aufgrund ihrer starken Einflussnahme infolge einer Reihe einhergehender meteorologischer Phänomene, die den Flugverkehr beeinträchtigen, wurden Gewitter als repräsentatives gefährdendes Wetter ausgewählt. Durch Gewitter induzierte Turbulenzen stellen eine besondere Gefahr dar und erfordern die Einhaltung gewisser Abstände zu den erkennbaren Gewitterwolken.

Eine proaktive Routenführung ist in aktuellen Verfahren nicht vorgesehen. Vielmehr wird eine Routenanpassung vom Piloten angefragt und mit dem zuständigen Fluglotsen abgestimmt sobald ein Konflikt mit dem geplanten Flugweg erkannt wird. Dies erhöht die Arbeitsbelastung des Lotsen, der diese Veränderung mit dem übrigen Verkehr koordinieren muss. Aktuelle Entwicklungen zukünftiger Verfahren im Rahmen eines europaweiten *Single European Sky ATM Research* (SESAR) Programms sehen einen Rückgang der sektoriellen Luftraumüberwachung vor. Stattdessen soll mit sogenannten 4D Trajektorien eine effizientere Flugführung ermöglicht werden. Eine solche Flugroute, geplant in Raum und Zeit, wird allen beteiligten zur Koordination bereitgestellt – zunächst vor dem Abflug und weiterhin aktualisiert mit u. a. angepassten Überflugzeiten anzusteuernder Wegpunkte während des Fluges. Dieses Vorgehen ermöglicht eine effektivere Ressourcenplanung und erhöht die Vorhersagbarkeit des Verkehrssystems. Dazu werden jedoch frühzeitig Wetterinformationen über die zukünftige Wetterentwicklung benötigt.

Die Vorhersagbarkeit meteorologischer Parameter variiert sehr stark. Gewitter sind aufgrund ihrer starken Sensitivität bezüglich interner und externer Auslöse- und Entwicklungsmechanismen sowie ihrer meist zufälligen Verteilung nur begrenzt vorhersagbar. Sobald sie aber detektiert sind, kann ihre weitere Entwicklung mit Hilfe sogenannter Nowcastsysteme in Zeithorizonten bis 1 - 6 Stunden vorhergesagt werden. Eine Restunsicherheit bleibt jedoch immer. Eine Methodik diese auszuwerten wird anhand eines objektbasierten Datensatzes des am Deutschen Zentrum für Luft- und Raumfahrt in Oberpfaffenhofen, Deutschland, entwickelten Systems Rad-TRAM präsentiert. Zellen des Nowcasts werden mit durch Rad-TRAM in Radarbildern detektierten Zellen bezüglich ihrer Größe und Position verglichen. Ihre räumliche Abweichung wird in vier Richtungen bestimmt und als Unsicherheit des Nowcastprodukts verstanden. 563 Zellzyklen werden analysiert und in Verteilungen entsprechend ihrer Vorlaufzeit und betrachteten Richtung zusammengefasst.

Perzentile, wie z. B. das 90., dieser Verteilungen erlauben die Bestimmung eines repräsentativen Unsicherheitsmaßes für das Rad-TRAM Produkt. Um diese Unsicherheit in der Ausweichroutenberechnung zu berücksichtigen, werden vorhergesagte Zellen um den so bestimmten Unsicherheitsabstand vergrößert, welcher richtungsabhängig ist und mit dem Nowcasthorizont variiert. Das entstehende Polygon definiert ein Gebiet, welches, sofern es vermieden wird, die Gefahr eines Wetterkonflikts auf der Route auf 10 % reduziert. Flächenmäßig ist das Unsicherheitspolygon bis über zwanzig mal größer als die ursprünglich vorhergesagte Zelle. Eine Berücksichtigung der Unsicherheit nimmt damit deutlich größeren Einfluss auf das Luftverkehrsmanagement. Welche Ausweichstrategien existieren unter Berücksichtigung verschiedener Wetterinformationen und welche Einflüsse lassen sich ableiten?

Monte Carlo Simulationen werden mit dem Ausweichrouten Modell DIVMET, entwickelt an der Leibniz Universität Hannover, durchgeführt. Trajektorien werden auf Basis der Charakteristiken jeder erstmals detektierten Zelle kreiert. Beobachtungs- sowie Nowcastdaten – letztere sowohl mit als auch ohne Unsicherheitsberücksichtigung – finden Anwendung mit variierter Updaterate. Verschiedene Routingtaktiken werden dann in aufeinanderfolgenden Simulationen für jeden der 563 Zellzyklen durchgespielt, um optimale Verfahren zu identifizieren. Im Wesentlichen werden die resultierenden Umwege verschiedener Taktiken, wie beispielsweise des *wait and see*, dem Ergebnis einer sofortigen Ausweichrouteneinleitung gegenüber gestellt. So werden Konsequenzen dieser Taktiken auf das Verkehrsmanagement aufgezeigt. Generell besteht ein starker Zusammenhang mit der Lebenszeit der betrachteten Gewitter. Eine Anwendung der *wait and see* Strategie, die darauf abzielt das Ausweichen auf eine bestimmte Distanz zum Objekt zu verschieben, ermöglicht es, aktuellere Beobachtungen oder Vorhersagen zu berücksichtigen. Ist die betrachtete Zelle bereits nicht mehr existent, wird keine Ausweichroute berechnet. Der optimale Ausweichhorizont vor der Zelle umfasst etwa 30 Minuten. Je länger das Ausweichen darüber hinaus verschoben wird, desto länger können Umwege werden. Stehen Nowcasts zur Verfügung, können diese eine effiziente und proaktive Routenführung ermöglichen. Eine Berücksichtigung der Unsicherheit reduziert die Zahl der auftretenden Konflikte auf weniger als 10 %. Jedoch verlängert sich der Umweg, wobei ein Großteil der Ausweichrouten überflüssig ist, da sich die entsprechenden Zellen entweder verlagert und oder abgeschwächt haben und kein Konfliktpotential mehr darstellen. Sind Nowcastupdates im Cockpit vorgesehen und ist eine Anpassung der Route in jeglicher Hinsicht erlaubt, so kann die Unsicherheit unberücksichtigt bleiben, da sie zu unnötigen Umwegen führen würde.

Diese Dissertation wird Entscheidungsträgern eine Hilfestellung in Bezug auf die Handhabung des Wetters und denkbarer Routingszenarien geben. Eine Identifikation eines optimalen Szenarios ist jedoch nicht möglich. Vielmehr wird ein Trade-off zwischen Vorhersagbarkeit und Routeneffizienz erkannt.

Schlagworte: Gewitter, Nowcastunsicherheit, Routingtaktiken, Gewitterumfliegung

Contents

List of Figures

List of Tables

Abbreviations

ACARE	Advisory Council for Aeronautics Research in Europe
AMS	American Meteorological Society
ANSP	Air Navigation Service Provider
ATM	Air Traffic Management
ATC	Air Traffic Control
ATCO	Air Traffic Control Officer
ATIS	Automatic Terminal Information Service
BADA	Base of Aircraft Data
CAPE	Convective Available Potential Energy based on temperature
CAPV	Convective Available Potential Energy based on virtual temperature
CAPPI	Constant Altitude Plan Position Indicator
Cb	Cumulonimbus
Cb-TRAM	Cumulonimbus Tracking and Monitoring
CEST	Central European Summer Time
CIN	Convective Inhibition Energy
CINS	Convective Inhibition Energy based on temperature
CINV	Convective Inhibition Energy based on virtual temperature
CPDLC	Controller-pilot data-link communication
CTAS	Center/TRACON Automation System
CWIS	Corridor Integrated Weather System
DIVMET	*Divert Meteorology*: Adverse weather diversion model
DLR	Deutsches Zentrum für Luft- und Raumfahrt (German Aerospace Center)
DWD	Deutscher Wetterdienst (German Weather Service)
DWR	Dynamic Weather Routes
EFB	Electronic Flight Bag
EPS	Ensemble Prediction Systems
FAA	Federal Aviation Administration
FACET	Future ATM Concept Evaluation Tool
IR	Infra-Red
ITCZ	Inner Tropical Convergence Zone
LCL	Lifting Condensation Level
LFC	Level of Free Convection
LNB	Level of Neutral Buoyancy

MET2ROUTE	Static Path-finding Algorithm in DIVMET
MODE	Method of Object-based Diagnostic Evaluation
NAS	US National Airspace System
NAVSIM	*Navigation Simulation*: Global 4D air traffic simulation model
NEXRAD	Next-Generation Radar
NM	Nautical Miles
NWP	Numerical Weather Prediction
OPSNET	US Operations Network
PPI	Plan Position Indicator
Radar	Radio Detection and Ranging
Rad-TRAM	Radar Tracking and Monitoring
RBT	Reference Business Trajectory
RHI	Range Height Indicator
RX product	Extended German radar composite
SESAR	Single European Sky ATM Research
SEVIRI	Spinning Enhanced Visible and Infra-Red Imager
SFC	Surface
SigWX	Significant Weather
SWIM	System Wide Information Management
SWIRLS	Short-range Warnings of Intense Rainstorms in Localized Systems
TMA	Terminal Manoeuvring Area
US	United States of America
USD	US Dollar
UTC	Universal Time Coordinated
VOLMET	Meteorological information for aircraft in flight
WAF	Weather Avoidance Fields
WGS84	World Geodetic System 1984

1 Introduction

1.1 The weather impact on aviation

Weather significantly affects aviation in terms of safety and efficiency. Airport as well as en-route operations are impaired by various meteorological phenomena (HAUF *et al.* 2013). Visibility reductions and wind inhomogeneities, for instance, have large impacts on airport capacity as staggering is increased and, as a result, landing and departure rates drop. Winter weather affects ground operations and forces de-icing measures of aircraft and ground surfaces which may lead to capacity declines and costly delays. Volcanic ash and icing layers in the atmosphere have to be avoided. Thunderstorms in the vicinity of an airport can even necessitate halting all ground operations in order to ensure safety (KULESA 2002). For airborne aircraft deep convection and thunderstorms incorporate nearly all kinds of hazardous phenomena to aircraft. Downbursts and wind shear affect aircraft in low levels during approach and take-off. Strong turbulence, icing and hail pose a risk especially in higher altitudes and at cruise level. All these adverse weather phenomena exhibit a high degree of unpredictability (DWD 2012).

The impact dimension varies significantly, from minor impact as e. g. by wet or iced airport pavements that cause slower ground movements and longer runway occupancies due to decreased braking action (ASHFORD *et al.* 1984), to large-scale events. Single events, like the unfamiliar strong winter weather in north-western Europe in December 2010 and January 2011 widely interrupted connectivity and caused thousands of stranded passengers (BUDD and RYLEY 2012). Though, the impact record to European aviation was set just months before by the Icelandic Eyjafjallajökull volcanic ash eruption in April 2010. Air traffic was terminated completely over Europe and in consequence, led to 100000 cancelled flights, more than 10 million stranded passengers and lost revenues of 1.8 billion USD for airlines (BOLIĆ and SIVČEV 2011). Generally, the impact strongly depends on geographical location and season (HAUF *et al.* 2013).

Regarding efficiency, weather is said to be the reason in half of all delays at Frankfurt Airport (MARKOVIC *et al.* 2008). In Europe, weather related costs currently amount to about 0.9 to 1.0 billion Euro per year (EUROCONTROL 2009). According to FAA (2015) statistics, which are based on OPSNET Standard Reports of 2008 to 2013, 69 % of all delays in the US National Airspace System (NAS) are caused by weather. KULESA (2002) estimates the resulting total national costs to about 3.0 billion USD. These include delay costs and unexpected operational costs as well as those to compensate accident consequences. Following statistics of KULESA (2002), FAA (2010) and BOEING (2011), in 10 to 30 % of all accidents weather was at least a contributing factor. EUROCONTROL (2013) even states that 12 out of 22 accidents between 2009 to 2011 were weather-related.

"We cannot control it but we need to learn to live with the elements and steadily eliminate the service disruption that they may cause" is the weather-related task formulated by the ACARE community (ARGÜELLES *et al.* 2001, p. 16). It implies that mitigation strategies to fit operations to the variable atmospheric condition need to be investigated in order to minimise the impact of adverse weather on aviation.

One of the largest impairing adverse weather phenomena are thunderstorms as they, at least in summer months, cause about 40 % of all US NAS delays (FAA 2015) and occurred on half of all weather affected days detected at European airports (EUROCONTROL 2013). In flight, an encounter may cause passenger injuries and aircraft structural damage. International regulations recommend to avoid thunderstorms by certain distances (up to 20 nautical miles (NM)) whenever possible (NATS 2010). Precise information on thunderstorm occurrence and location is not yet provided in weather forecasts currently used for trajectory planning. The latter is usually performed days to weeks before the actual flight (CHEUNG *et al.* 2014). Thus, re-routing around thunderstorms, so far, is in the responsibility of the pilot who tactically decides whether or not and how to deviate from the planned trajectory. His decision making is mainly based on visual impression and, if available, the on-board radar display that gives information on the actual situation ahead of the aircraft. Steady correspondence with the responsible air traffic control officer (ATCO) who need to give clearance to envisaged manoeuvres, however, ensures coordination with other traffic. Aircraft routes in the vicinity of convective cells are very often reactively adapted to the changing situation. Proactive avoidance is seldom possible as information on the further development of single cells is typically not provided. ATCO work load in such situations is highly increased as complex traffic patterns have to be resolved. The coordination of several deviating flights requires a lot of verbal communication – at least one request and the respective clearance for each heading change. Very often thunderstorms block larger airspace around which crowding effects may occur (EUROCONTROL 2014).

Increasing numbers of passengers and flights even compound the former effects. Aviation suffers from a general capacity problem and requires changes in air traffic management (ATM). The Single European Sky ATM Research (SESAR) programme faces these problems. It will "facilitate a high-performance air traffic management infrastructure which will enable the safe and environmentally friendly development of air transport" (European ATM Master Plan by SESAR JOINT UNDERTAKING (2012), p. 5). As stated in the same document, SESAR originally aimed to

- enable a 3-fold increase in capacity on the ground and in the air
- improve safety by a factor of 10
- enable a reduction of the environmental impact of flights by 10 %
- reduce ATM service costs by at least 50 %.

These goals had been first defined in 2005 and were revised in the meantime. They should be met by 2020 when traffic movements are expected to have been grown by 30 % compared to 2005 (SESAR JOINT UNDERTAKING 2012). In order to reach these goals current procedures are stepwise transferred to time-based, trajectory-based and, finally, performance-based operations while sharing all relevant flight information with the aviation system stakeholders (system wide information management, SWIM). Especially the step from currently operational airspace optimised handling to a four-dimensional (4D) trajectory management will enable more efficient routing. A planned route, close to the ideal profile of an airline is coordinated with other traffic and becomes the reference business trajectory (RBT) shortly before departure (SESAR JOINT UNDERTAKING 2014). It should already incorporate mitigation strategies to compensate weather effects strategically. Proactive measures to avoid adverse weather regions need to be applied then in order to keep changes of the actual trajectory to a minimum. However, the initiation of such strategies to mitigate the adverse weather impact in order to ensure safe and efficient operations strongly depends on accurate forecasts. Early effectiveness of measures enable to maintain stable operations. At the same time decision makers, such as pilots, airport management or ATM, take a risk that the expected impact fail to appear whereby financial losses emerge that are brought about by the introduced regulations. Thus, there is a demand for action to identify reasonable weather information, give advice on handling and evaluate mitigation strategies.

1.2 Motivation

The increasing awareness of adverse weather as an influencing factor to air traffic operations and its negative effects on safety and efficiency lead to a demand of appropriate weather information. Despite of the partly inherent chaotic nature of weather, numerical weather prediction (NWP) still provides useful information on the future state of the atmosphere (CHEUNG *et al.* 2014). Depending on the meteorological phenomenon, its scales and features, forecast skill varies and accuracy drops at different rates (WILKS 2011). Uncertainty grows with increasing forecast time and, thus, reliability is significantly reduced. In order to counteract, NWP underwent a transition from single deterministic model runs to ensemble prediction systems (EPS) in recent years. The latter try to build a representative sample of the future atmospheric state by providing several numerical predictions performed either by different models, with slightly disturbed initial conditions or varying model physics (WMO 2012). The frequency of certain conditions in the emerging ensemble allows for probabilistic statements on the likelihood of the occurrence of an event (COIFFIER 2011). Still, uncertainty increases with lead time which is perfectly noticeable in the visualisation of ensemble results in so called spaghetti plots (WILKS 2011) as exemplary shown in Figure 1.1. Starting at a narrow position the lines, each representing one ensemble member, spatially depart with forecast time. The appar-

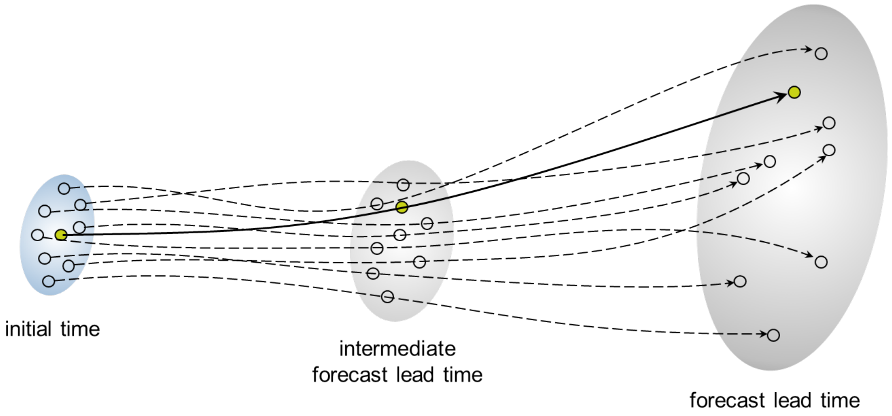

Figure 1.1: Spaghetti plot indicating the increasing forecast uncertainty with lead time visualised by the spread of several deterministic forecast members of an EPS (based on WILKS 2011).

ent spread represents the difference between minimum and maximum value given by the ensemble at a certain time. This spread is equivalent to the uncertainty of the atmospheric future state usable for risk assessments (COIFFIER 2011). The IMET project investigates an optimal approach for future trajectory prediction systems to use meteorological uncertainty information given by EPS for pressure, temperature and wind. Equivalent to the meteorological data ensemble in Figure 1.1, the resulting set of trajectories first remained in close neighbourhood but spread out the larger the lead time became. Thus, the variation of simulated flight times increases with the latter (CHEUNG *et al.* 2014).

In contrast to the continuous meteorological parameters considered in IMET, thunderstorm prediction in numerical models of EPS often features only limited accuracy. With grid sizes of several kilometres single storm cells are not precisely resolved. This is due to their small-scale occurrence in time and space, as well as because of convection initiation which may be triggered by slightest instabilities and is rather chaotic in nature (COIFFIER 2011). Whereas regions where convection is likely to occur in certain periods are more or less forecastable, neither the exact time and location of the onset of single cells nor their storm path and lifetime is precisely predictable (DWD 2012).

For a small-scale event, such as a thunderstorm cell, once it exists and has been recognised, nowcast systems can be consulted as they provide more precise information on the cell development for one to six hours ahead. Extrapolation techniques are applied to successive observations of the regarded phenomenon obtained by remote sensing methods like radar and satellites. Equivalent to NWP, the longer the lead time, the larger the uncertainty (WILSON *et al.* 1998). Cells may grow or shrink, they may dissipate or be located at different positions than nowcasted. Thus, to enhance ability and accuracy of the system, the nowcast is typically updated with rapid rates of radar and satellite products which are provided with maximum rates of up to 5 minutes. This enables a steady adaptation to the actual situation and allows for consideration of cells that just arose to relevant intensities.

This information, when being available in the cockpit by data-link techniques, may enhance the situational awareness of pilots and increases the decision horizon compared to current weather avoidance strategies (Stich *et al.* 2013). At the time being, navigation around adverse weather is mostly, especially at night, based on convective cells recognised by the on-board radar. However, the scanned area is typically limited to an 80° to 120° circular sector with a radius up to 200 NM covering a flight time of about 25 minutes at speeds of $250\,\mathrm{m\,s^{-1}}$ (Airbus 2007). While approaching the relevant area, the cell shape and intensity may change and the final state yielding the necessity to avoid is only recognisable when the cell is already reached. Thus, the uncertainty, as introduced in the ComplexWorld Position Paper (2014) and as defined here as being a condition of limited knowledge about the future outcome, decreases with the shrinking approach horizon, as shown in Figure 1.2.

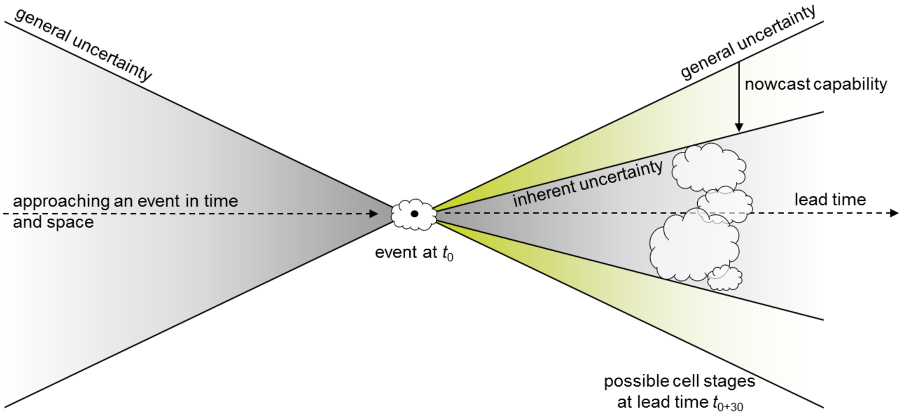

Figure 1.2: Schematic cones representing the decreasing uncertainty when approaching an event, e. g. a thunderstorm cell, in time and space (left of the event) or when considering a nowcast (right of the event) that ideally reduces the general uncertainty to what is inherent to thunderstorm development (based on Sauer *et al.* 2014, Sauer *et al.* 2015a).

Important to note is that nowcasts may significantly reduce the general uncertainty (see right side of Figure 1.2). Still a certain degree of uncertainty remains which naturally is product-dependent. Though a nowcast is assumed to represent the best knowledge about the further development of the weather situation, the remaining product specific, unavoidable uncertainty has to be taken into account for any application such as weather avoidance routing by pilots in the cockpit. Once the uncertainty distributions have been determined, they may supplement a nowcast to yield a probabilistic nowcast.

Apart from the weather information itself the decision made by pilots concerning weather avoidance significantly influences the overall ATM performance. This holds for total flown detour miles as well as for integrated delay minutes. Different tactics can be applied regarding diversion initiation – even with current procedures when being limited to the on-board radar. The pilot may deviate instantly when a conflict is detected at the far end of the display. Alternatively he may continue on the planned trajectory, monitor the situation and decide what to do when approaching the conflicting cell, as it will develop and perhaps dissipate in the meantime. Having nowcast data on hand, even more options are available which have not been evaluated yet.

Thus, the following questions attract to perform studies on this field of aviation:

1. How to determine the nowcast uncertainty in an appropriate way to further apply it in weather avoidance routing?
2. What are the typical scales of the spatial uncertainty of a nowcast system?
3. What is the effect of different routing tactics applied to either observational or nowcast data, the latter with or without uncertainty consideration, on detour length?

1.3 Objectives

Nowcasts are the most accurate short-term information available for already existing thunderstorm cells. As a representative nowcast the Radar Tracking and Monitoring (Rad-TRAM) system provided by the German Aerospace Center (Deutsches Zentrum für Luft- und Raumfahrt, DLR) is chosen. Its quality and a concept for product-independent uncertainty determination will be elaborated. The methodology derived in the study should ideally be suited for application also to other meteorological parameters that need to be accounted for as being impenetrable airspace areas, like icing regions or volcanic ash clouds.

The lead time-dependent measures found when applying the elaborated concept to the nowcast data set should then be reviewed using a cone as indicated in Figure 1.2. This allows for estimating the growth rate of the nowcast uncertainty.

The found uncertainty, which however is determined from a limited data set, shall then broaden the probable handling strategies of available weather data in weather avoidance routing in order to evaluate their effects on ATM performance. As a measure, the flown detour length is considered that emerges from any weather diversion. Monte Carlo simulations will reveal the range of deviation manoeuvres and resulting detours by varying the weather information as well as the routing tactic. A set of scenarios should be defined that differ in those parameters. Either observational data or nowcasts can be used, the latter with or without consideration of the determined uncertainty. Additionally, routing tactics should be designed that depict a broad field of possible solutions. The study aims then to reveal respective effects on the resulting route length which is assumed here as being one out of a set of measures representing ATM performance.

1.4 Methodology

In order to fulfil the scope of the study entitled *On the Impact of Adverse Weather Uncertainty on Aircraft Routing – Identification and Mitigation*, basically two subjects need to be touched subsequently. The first aspect is the uncertainty of adverse weather for which thunderstorms are taken as a representative. As stated previously, the onset of such is rather hard to predict, whereas their development can be somewhat foreseen by nowcast models once they exist. Based on observed thunderstorm cell stages the models provide a short-term forecast up to one to six hours. Object-based nowcasts over Germany with lead times up to 60 minutes generated by Rad-TRAM are analysed with respect to their uncertainty. The nowcasted cell for a certain lead time is assumed to be the best knowledge about the then probable cell stage. It is compared to the later, if still existing, observed cell at the respective time. Any spatial deviation of the two cells is assumed to define the uncertainty of the nowcast product. Uncertainty is evaluated in four directions with respect to the cell movement (FORWARD, BACKWARD, LEFT and RIGHT). A complete data set of 15 July 2012 consisting of 563 individual cell life cycles is used. All found values are merged into frequency distributions for each of the four directions and twelve lead times (5, 10, ..., 60 minutes). Percentiles of the distributions (WILKS 2011) are used to define representative measures of the uncertainty development with lead time.

In order to mitigate the uncertainty of the nowcast, the 90th percentile is chosen and then applied to each nowcasted cell development itself when being used in weather avoidance routing. Thunderstorm cells, typically outlined by a certain reflectivity threshold, e. g. 37 dBZ (TAFFERNER and FORSTER 2012), in radar images or, if for future times, provided by nowcast systems are treated as 2D horizontal polygonal airspace sections. For modelling purposes these polygons are assumed to range from the surface to the upper atmosphere such that they force a lateral deviation around each cell. The previously determined uncertainty measure can now be applied to the nowcasted cells. One of the latter cells is enlarged in all directions pursuant to the weighted four uncertainty values (one for each direction) of the respective set valid for the considered lead time. The larger the lead time, the larger becomes the new polygon. It defines an airspace that covers the later observed cell with 90 % certainty. In the remaining 10 % of all analysed nowcast cells it may happen that one or the other edge was further away in the given direction as stated by the considered value. Thus, if this uncertainty polygon is avoided by aircraft, actual cell encounters are limited to 10 % maximum.

As it is the second major part of this thesis, weather avoidance route simulations are performed and analysed. The adverse weather diversion model DIVMET, originally developed by HAUF and SAKIEW at the Institute of Meteorology and Climatology of the Leibniz Universität Hannover is used for that purpose. The effect of individual cell behaviour on aircraft routing is evaluated based on a large set of simulations, similar to Monte Carlo simulations. The simulation set-up is as follows. According to the first detected state and the respective movement direction of each of the 563 individual cell cycles of the sample day, a respective generic trajectory is generated. It is orientated along the great circle while heading behind the cell until the aircraft will eventually outruns it. The aircraft departure distance varies between flight times of 5 to 60 minutes to the cell. While leading directly through the original cell gravity centre, the trajectory ends at two hours flight time downstream. The defined scenarios vary in the reaction to the seen weather situation. Among instant diversion initiation, a kind of *wait and see* tactic is accounted for in which the deviation initiation is postponed. When varying the weather

data type and going on from observational to nowcast data different tactics can be applied as well. Nowcasts are deployed either in conjunction with or without uncertainty margins. They may be provided to pilots only once before departure or may be updated which is associated with a shrinking uncertainty margin if this is considered.
The evaluation of simulation results focuses primarily on the detour length. Individual detours as well as such integrated over all simulations of one scenario are analysed to account for pilot and airline perspectives. Counts of cell encounters and markers for unnecessary deviations allow for an assessment of the utility of a tactic.
An identification of the *optimum* strategy is not expectable as it strongly depends on the needs and requirements of the airspace user which tactic fits best. If predictability is the key parameter with highest priority, a totally different strategy will be appropriate than if efficiency is most important.

Innovations arising from this study and introduced in this thesis are:

1. the spatial uncertainty determination method which, compared to traditional and spatial verification methods that are typically applied to nowcasts or forecasts, accounts for direction-dependent deviations in four directions with respect to the cell movement.
2. an identification of an appropriate uncertainty measure and its application to nowcast cells for weather avoidance routing.
3. an systematic analysis of the effect different routing tactics applied to a sample set of real thunderstorm cell life cycles have on detour length.

Thesis organisation
The thesis is structured the way that first an introduction to thunderstorms, including their hazards posed to aviation, their evolution and specific characteristics, is given in Chapter 2. In the same Chapter an overview of monitoring techniques and thunderstorm forecasting with special emphasise on nowcasting is provided. A description of the Rad-TRAM nowcast system together with an outline of forecast verification methods can be found there as well. Nowcast data provided by Rad-TRAM is described and analysed regarding its uncertainty in Chapter 3. After having given there an indication on how to apply the found uncertainty in diversion route calculation, current re-routing procedures and decision support tools for navigation around or through a field of adverse weather are shortly outlined in Chapter 4. There, the adverse weather diversion model DIVMET is described in detail as well. Routing tactics in adverse weather situations and the Monte Carlo simulation set-up are defined in Chapter 5. In order to identify coherences of the applied tactics, also an analytic consideration is preceded to the analysis of the simulation results which follows in Chapter 6. Summary and conclusion together with an outline of probabilities to transfer found results and methodologies to other phenomena finally end this thesis in Chapter 7.

2 Thunderstorms – threats, characteristics and nowcasting

A thunderstorm is a convective cumulonimbus cloud (Cb) characterised by lightning and thunder which are the final phenomena resulting from building mechanisms of the cloud itself (GATES 1979). Even before the occurrence of these two effects, the convective cloud may incorporate the most threatening phenomena for aviation, which are among others turbulence and icing.

Because of their severity, thunderstorms are exemplary chosen in the scope of this work as being the representative adverse weather event. First a detailed overview on their risks posed to aviation will be given. Afterwards a short introduction in convection and thunderstorm formation including the somewhat unpredictable initiation conditions as well as details on thunderstorm evolution and types are given in this Chapter. Finally monitoring techniques, state of the art nowcasting methods as well as verification techniques are introduced.

2.1 Hazards to aviation

Thunderstorms are one of the most threatening events in the earth atmosphere. Lightning and related thunder upset the public, heavy precipitation with hail often leads to flash floods and costly damage. For airborne aircraft even more phenomena associated with thunderstorms are of relevance. That is why pilots rank thunderstorms as the primary weather phenomenon comprising flight safety (GERZ *et al.* 2012). The hazardous processes associated with thunderstorms and their influence on aviation are discussed in the following.

Turbulence. Thunderstorms are dominated by vertical motions. The main updraught with speeds of $65\,\mathrm{m\,s^{-1}}$ reaches diameters of one kilometre. In close proximity downdraughts at $25\,\mathrm{m\,s^{-1}}$ are possible. Thus, when flying through a storm cell the aircraft may experience hazardous forces due to strong horizontal gradients in the vertical acceleration (HAUF *et al.* 2004). It is rather impossible to hold constant altitude; instead it may change significantly. The encounter of considerable turbulence in clear air well away from the cell itself is also not unusual (LANKFORD 2000). This may happen not only anywhere around the cell but also above it triggered by the overshooting updraught. That is why international regulations recommend not only to avoid a cell but to account for certain safety distances to it. In rare cases where overflying a developing cell could be an option, a vertical spacing of at least 5000 ft should be considered (NATS 2010). Therefore, overflying mature cells is generally rather not possible as they reach up to maximum flight levels and above (HAUF *et al.* 2004).

Downburst. Beneath the cell downdraughts continue and spread out circularly when touching the surface. The resulting wind field is characterised by shear that is hazardous to landing and departing aircraft flying below thunderstorm cells (HAUF *et al.* 2004). This is even compounded by the fact that heavy rain and poor visibility prevail below the cell (LANKFORD 2000). In quick succession the aircraft will experience headwind that increases lift, followed by downdraught and tailwind when having traversed the cell. Both latter conditions reduce lift and require an instantaneous counteraction of the pilot in order to prevent a too strong loss of height that may end in uncontrolled touching the ground surface or any obstacles (HAUF *et al.* 2004).

Hail and heavy precipitation. The strong vertical movements in a cloud lead to a strong growth of droplets. As a result heavy precipitation and hail may occur. The former process poses a risk of engine flame out (HAUF *et al.* 2004). Hail is especially strong within severe storms in their mature stage. Even if hail is not observed at ground it may occur within the cloud or beneath the anvil (LANKFORD 2000). Hail stones reach sizes of a fist and fall at speeds of up to $30\,\mathrm{m\,s^{-1}}$ (HAUF *et al.* 2004). When hitting an aircraft in flight they cause structural damage. Cracked windscreens, damages on the aircraft nose and leading edges of the wings as well as engine power loss are the most risky results of an hail encounter and may force the pilots to land (LANKFORD 2000).

Icing. Water in the atmosphere can remain liquid until -40°C. This is due to a lack of ice nuclei (HAUF *et al.* 2004). Because of the strong vertical transport huge amounts of water circulate in the cell. Water in altitudes above freezing level is supercooled (LANKFORD 2000). Such droplets freeze as soon as they hit the cold body of the aircraft (GERZ *et al.* 2012). Even though the horizontal extent of a thunderstorm and, thus, the flight time within the cell is limited, ice aggregation may become severe (LANKFORD 2000). It may block air intakes of flight control devices and sensors what results in misleading instrument indications (GERZ *et al.* 2012). Modified aerodynamics due to iced leading edges as well as the additional weight of ice, significantly modify the aerodynamics and reduce manoeuvrability of the aircraft.

Lightning. Separation of electrical charges in thunderstorms is caused by strong up- and downdraughts in the centre of a convective cell (BFGOODRICH AEROSPACE 1997). Electrical discharges that characterise a thunderstorm as such may strike aircraft. The latter can even trigger discharges. Passengers and crew are protected as the metallic body of the aircraft function as a Faraday cage. However, due to temperatures of several thousand Kelvin within the lightning channel, considerable thermal damage may occur at entry and exit points on the aircraft (HAUF *et al.* 2004). Electrical instruments can get damaged and pilots may be temporally blinded, hindered at reading the instruments and consequently may lose control about the aircraft (LANKFORD 2000).

Tornados. Severe thunderstorms can produce rotating funnel-shaped clouds. High wind speeds and extremely low pressure within the vortex create turbulence that poses a risk to aviation (HAUF *et al.* 2004). The frequency of tornado occurrence is rather low in Europe but of significant relevance in the US.

Due to these multi-layered risk to aviation that are posed by thunderstorms, pilots are encouraged to avoid cumulonimbus clouds while accounting for least distances in order to prevent encountering any of the just described processes that may also occur in the vicinity. Overflying or a traverse below the storm are not recommended – again because of some of the discussed processes (see e. g. NATS 2010). Nevertheless, several incidents and accidents are recorded, in which thunderstorms and associated processes were at least a contributing factor. A summary of weather-related accidents is provided by FAA (2010).

The conditions under which thunderstorms may form and where and when this actually occur are discussed in the following Section.

2.2 Thunderstorm generation

Thunderstorms form by deep convection – a process that in meteorology usually describes a vertical and buoyant transport of a property like heat or mass (STICH 2012). Necessary conditions for convection initiation are the availability of moisture in lower levels, the provision of lift and atmospheric instability. The latter is favoured by a rapidly decreasing temperature with height and should reach throughout large parts of the troposphere to enable deep convection (ZINNER and GROENEMEIJER 2012).

2.2.1 Larger scale conditions for thunderstorm formation

Information on atmospheric instability required for deep convection can be deducted from vertical temperature profiles plotted in a so called skew T – log p diagramme as exemplary shown in Figure 2.1. Recordings of temperature and dew point temperature as shown here on a logarithmic pressure ordinate are obtained by a radiosonde sounding in Milan at 00 UTC on 15 July 2012. However, such profiles can equally be extracted from 3D forecast fields of numerical weather prediction (NWP).

The course of such profiles relative to coloured lines in the background reveal insights in the actual or forecasted atmospheric state. Blue straight, skewed lines from bottom left to top right represent isotherms, i. e. lines of equal temperature. Purple lines indicate equal mixing ratio (isohumes). Curved lines display temperature changes in adiabatic lifting processes.

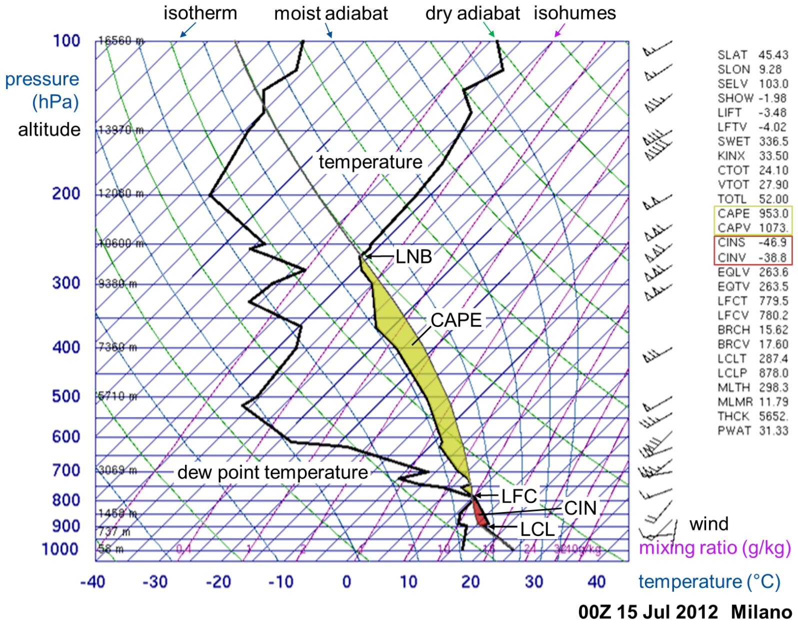

Figure 2.1: Skew T–log p diagramme obtained from a Milan sounding at 00 UTC on 15 July 2012. Vertical profiles of temperature and dew point temperature (solid black lines) given on a logarithmic pressure ordinate. Dry adiabats (green lines) indicate temperature changes in vertical motion of a parcel below the LCL. Above that level temperature change along the moist adiabats (blue up-left lines). The first intersection with the environmental temperature profile marks the LFC which bounds the CIN area (red). Above this level the CAPE area (light green) classifies the vertical range of potential buoyancy which is limited by the LNB. Blue rightward skewed lines give isotherms, purple lines represent isohumes (lines of equal mixing ratio). Wind in different altitudes as well as characteristic values calculated from the profiles are given on the right side. Diagramme taken from (University of Wyoming 2012) and style adapted from (Stich 2012).

The theory of a lifted parcel, invented by Bjerknes (1938) and further discussed by Manzato and Morgan (2003), can be used in conjunction with such a diagramme to describe thunderstorm development. Following the idea of an air parcel, processes result from any difference of the parcel state compared to its surrounding. An air parcel at surface level has the same temperature as observed. If this parcel is then triggered to rise (potential triggering mechanisms will be discussed in Section 2.2.2), its temperature will first decrease according to the dry adiabatic lapse rate of -9.8 K km^{-1} which is reflected in the green upward left line. Vapour pressure increases until the parcel gets saturated and condensation occurs in a level that is referred to as lifting condensation level (LCL). The formation of a cumulus cloud starts at this level which defines the bottom height of the cloud. Latent heat is released in the condensation process and helps to keep up the temperature difference of parcel and environment. The latent heat release reduces the further cooling to the moist adiabatic lapse rate. The latter varies with temperature and leads to a cooling between 5 and 9 K km^{-1} along the blue upward left lines. If, as in Figure 2.1, the atmospheric condition is warmer than the air parcel, forcing for further rise is required to overcome the convective inhibition energy (CIN) indicated by the red area between LCL and LFC. The latter indicates the level of free convection and is defined by the intersection environmental temperature curve and the considered moist adiabat. Once this level is reached, the parcel is always warmer than its surrounding and an unstable condition is reached. The parcel is naturally buoyant and, thus, will ascent without any further triggering. If then the moisture condition allows for, a deep convective cloud forms. The latter is vertically bounded; its cloud top is defined by the level of neutral buoyancy (LNB) where the air parcel temperature is again equal to the ambient air. This is usually close to the tropopause, in about 10 km as given in Figure 2.1, where stratospheric warming supersedes tropospheric cooling with height (ZINNER and GROENEMEIJER 2012).

The green marked area between LFC and LNB, enclosed by the environmental temperature curve and the moist adiabat, defines the convective available potential energy (CAPE). It is proportional to the kinetic energy a parcel may gain from its environment (MARKOWSKI and RICHARDSON 2010) and gives information on whether the moisture content of air is high enough that parcels may become buoyant (DOSWELL 2001). According to MARKOWSKI and RICHARDSON (2010), CAPE is defined as

$$CAPE = \int_{LFC}^{LBN} B\,\mathrm{d}z \quad \approx \quad g\int_{LFC}^{LBN} \frac{T_\mathrm{v}'}{\overline{T_\mathrm{v}}}\,\mathrm{d}z \tag{2.1}$$

with gravitational constant g and buoyancy B. The latter is expressed by the virtual temperature perturbation of the air parcel T_v' relative to the virtual temperature $\overline{T_\mathrm{v}}$ of the environment. That of the parcel is $T_\mathrm{v} = \overline{T_\mathrm{v}} + T_\mathrm{v}'$ and is defined as the temperature dry air would have when pressure and density are equal to those of the moist air parcel. T_v is always higher than the actual measurable air temperature T (BAILEY *et al.* 2000).

The work that has to be spend to bring the air parcel to its LFC is described by the CIN. It is a negative area defined by

$$CIN = \int_{0}^{LFC} B\,\mathrm{d}z \quad \approx \quad g\int_{SFC}^{LFC} \frac{T_\mathrm{v}'}{\overline{T_\mathrm{v}}}\,\mathrm{d}z \tag{2.2}$$

wherein the surface (SFC) is at $z = 0$. Opposite as in Equation 2.1, here buoyancy is negative as CIN reflects the area between the warmer environment temperature profile and the cooler moist adiabat. The parcel temperature changes along the latter from which a negative virtual temperature perturbation T_v' of the parcel results.

CAPE $\leq 1000\,\mathrm{J\,kg^{-1}}$ is usually considered as being small whereas values $\geq 2500\,\mathrm{J\,kg^{-1}}$ are rather large in typical severe storm environments (MARKOWSKI and RICHARDSON 2010), e. g. in the US during summer time (BROOKS *et al.* 2003). In Europe, CAPE hardly exceeds values of $2000\,\mathrm{J\,kg^{-1}}$ (ROMERO *et al.* 2007). CIN is considered as being a small barrier if $\geq$ -10 $\mathrm{J\,kg^{-1}}$ and rather convection prohibiting if values are $\leq$ -50 $\mathrm{J\,kg^{-1}}$ (MARKOWSKI and RICHARDSON 2010). Thunderstorm initiation is likely if CAPE is large while CIN is close to zero. However, the application of distinct thresholds and the pure presence of CAPE in conjunction with CIN that is close but not equal to zero is no sufficient condition for thunderstorm formation (STICH 2012). Instead, consideration of moisture is an often underappreciated aspect when calculating both values (MARKOWSKI and RICHARDSON 2010). As recognisable from the list right in Figure 2.1, CAPE and CAPV as well as CINS and CINV are given which are based on temperature and virtual temperature, respectively (UNIVERSITY OF WYOMING n.Y.). The likelihood of thunderstorm initiation is usually increased if the latter is applied what is nicely presented by MARKOWSKI and RICHARDSON ((2010), Fig. 2.9).

2.2.2 Trigger mechanisms

Whether or not free convection and, thus, thunderstorm formation is initiated, is rather a direct result of local processes that may trigger lift (ZIMMER *et al.* 2011). In any case it is crucial to overcome the CIN and to reach the LFC (STICH 2012). Lift can either be thermally induced or forced by upgliding processes at orographic obstacles.

Thermally induced convection emerges as a result of increasing moisture and differential heating near the surface or along a sloped terrain in the course of a day (ZINNER and GROENEMEIJER 2012) is a typical process observed in summer time (GEORGII 1927). The required temperature that triggers enough lift to reach the LFC in the ambient environmental condition can be determined. Whether or not this temperature will be reached depends on solar heating and can be forecasted with great certainty for a region. Likewise the expected time at which the trigger temperature is reached can be provided by NWP. Nevertheless, these forecasts are made on grids with sizes much larger than those of initial triggering processes (see Section 2.5). The resulting so called air-mass or thermal thunderstorms do occur isolated and randomly. Where and when exactly the initial lift is triggered is not precisely forecastable but remains as the major uncertainty of thunderstorm forecasting.

Mechanical induced convection occurs on obstacles that force air to deviate vertically. Such an obstacle might be a geographically fixed mountain range but it can also be much smaller, like a coastline where surface friction increases abruptly. Whether or not lifting can be expected due to such obstacles strongly depends on the atmospheric flow and is more or less predictable. Meteorological conditions that trigger lifting in a mechanical way are, for instance, convergence lines and cold fronts. The latter occur on synoptic scales in conjunction with advection of colder air in mid-latitudes. As the latter has higher density, it slides under the warmer and lighter air and forces it to ascent along the front. At the same time colder air rushes ahead of the surface front, destabilise the atmosphere and, thus, enable convection initiation of the upgliding air. Such air mass boundaries as well as low level convergence, which occur due to sea breezes or along dry lines (ZINNER and GROENEMEIJER 2012), introduce upward motion that may lead to thunderstorm formation throughout the year. According to the condition from which they are built, this kind of storms is referred to as frontal thunderstorms that often feature a linear arrangement of cells. In conjunction with the synoptic-scale flow, convection and

the formation of new thunderstorms maintain constant over a rather long period while travelling with the front and introducing a break in the weather (GEORGII 1927).
As this type of triggering is related to synoptic scales, which are usually accounted for in NWP, predictability regarding the strength of potential forcing as well as the resulting location and time of convection initiation is increased. A longer lifetime of these thunderstorms facilitate their forecasting.

2.3 Thunderstorm characteristics

Major knowledge about the structure and detailed characteristics of thunderstorms was obtained under large effort in the *Thunderstorm Project* performed in the US in the summer seasons of 1946 and 1947. A detailed description of that project performed by four U.S. Government Agencies (Air Force, Navy, National Advisory Committee for Aeronautics, and Weather Bureau) can be found in BYERS and BRAHAM (1949). Most of their findings are still state of the art and, thus, some of which are summarised in the following.

2.3.1 Evolution of thunderstorm cells

Three characteristic stages each cell passes through during its lifetime were identified by BYERS and BRAHAM (1949). These are 1) cumulus stage, 2) mature stage and 3) dissipating stage as shown in Figure 2.2.

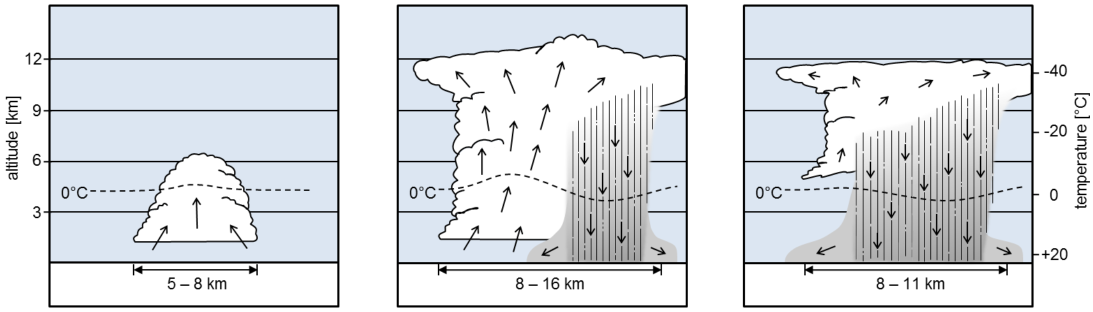

(a) Cumulus stage. (b) Mature stage. (c) Dissipating stage.

Figure 2.2: The three stages of a thunderstorm life cycle with associated vertical motions and precipitation (based on MARKOWSKI and RICHARDSON (2010) who adapted the figure from BYERS and BRAHAM (1949) and DOSWELL (1985)).

Cumulus stage. In its initial stage the cumulus cloud is dominated by updraughts that are increasing to the centre of the storm and with altitude as indicated in Figure 2.2(a). Condensation of water vapour leads to a strong swelling of the cloud and formation of a towering cumulus. Starting from first identification of a fair weather cumulus cloud with a diameter of about 2 km the cell grows to about 5 to 8 km in diameter and reaches up to 8 to 10 km in this stage which lasts 10 to 15 minutes. Intensity of the updraught increases with time and may exceed speeds of 15 m s^{-1} which bears up precipitation droplets that start to form when the freezing level is reached. Unless this level is reached a radar echo can hardly be obtained by cells in the early cumulus stage (BYERS and BRAHAM 1949).

Mature stage. From a large number of cumulus clouds in the initial phase forming on a warm summer day due to instability of the atmosphere, only a small number actually continue their growth throughout the maturing stage. Whether they do or do not is determined by peculiarities in the immediate environment of the cell. It needs to feed the cloud with water vapour to support condensation for further swelling to higher levels. At the same time condensation increases the number and size of drops and ice crystals that start falling. When rain is first identified at the earth surface, BYERS and BRAHAM (1949) defined the cell to be in the mature stage. Due to the still prevailing strong warm and moist updraughts – now locally exceeding $30\,\mathrm{m\,s^{-1}}$ – the cloud is further towering through the stage of a cumulus congestus to levels of typically 12 km (occasionally up to 18 km) and reaches its greatest extent in the mature stage (BYERS and BRAHAM 1949). The maximum height is limited by the LNB which is usually close to the stable layered tropopause characterised by a temperature inversion which starts in an altitude of about 12 km in mid latitudes (7 km in polar and about 16 km in equatorial regions). Moist air transported upwards by moderate currents is decelerated by the stable layer and deviates to the sides. In a temperature environment usually below -40 °C the characteristic iced anvil of the thunderstorm is formed below the covering inversion (ZINNER and GROENEMEIJER 2012). The central main updraught may be strong enough to even push the moist air into the stable layer where it forms the so called overshooting top, as recognisable in Figure 2.2(c) (BEDKA 2011). The then existing thunderstorm is referred to as a cumulonimbus cloud (Cb) (ZINNER and GROENEMEIJER 2012).

As precipitation starts when entering the mature stage, falling droplets put drag on the ascending air forcing the introduction of a downdraught in central parts and lower levels of the cloud. Simultaneously prevailing warm updraughts and cold downdraughts characterise the mature stage of the cell in which the horizontal and vertical extents increase gradually (BYERS and BRAHAM 1949). Due to these side by side counter-movements, the cloud top is thought to become positively charged while the lower section is negatively charged. Having reached a critical value of electrical potential that depends on the conductivity of air, discharges may occur that become recognisable by lightning and thunder (GATES 1979).

The cold air descends with up to $12\,\mathrm{m\,s^{-1}}$ and spreads out horizontally in radial direction forming the so called gust front when hitting the earth surface. In association with the airflow, temperature drops and pressure rises in low altitudes. The gust front may trigger the development of new cells (RAUBER *et al.* 2005) as will be detailed in conjunction with multicell storms. Within the cloud, turbulence is strongest in this stage, especially where maximum speeds of up- and downdraughts meet. After 15 to 30 minutes in this stage the downdraught area exceeds over the entire storm in low levels and, thus, introduces the final dissipating stage of the thunderstorm.

Dissipating stage. In the final stage (see Fig. 2.2(c)) the downdraught spreads rapidly due to precipitation falling from the remaining updraught which is weakened by the drag of raindrops. This process continues over about 20 minutes until downdraughts prevail the cell or no vertical motion at all can be found. Turbulence is possible to be classified as heavy in the early dissipating stage but decreases with time. The same holds for temperature variations due to warm up- and cold down-winds. The latter first cools the air of the cell further down before it finally heats and reaches the environmental conditions again. Shedding precipitation continuously reduces the amount of water in the cloud what results in diminishing precipitation and dissipation of diverging winds at the earth surface (BYERS and BRAHAM 1949).

2.3.2 Types of organisation

Thunderstorms are typically categorised by three types depending on their size and appearance, whether it is an isolated cell or a cluster. Each of which passes through the three stages of cell development that were previously discussed.

Single cell. An isolated thunderstorm cell is a rather small and rare type of storm compared to the following ones. It typically develops from thermal convection on warm and humid summer days. An isolated cell usually has a lifetime of 20 to 30 minutes while producing a radar echo (for further reading on radar measurements please refer to Section 2.4.1), i. e. overcomes a certain intensity, for an average of 20 minutes (BYERS and BRAHAM 1949). The single cell is seldom strong enough to produce real severe weather. Instead, it rather includes brief periods of heavy rainfall and marginally severe hail or brief microbursts. Weak tornadoes can occasionally occur. The gust front of a cell often triggers the growth of new cells leading to the formation of a multicell storm.
As they are often thermally induced, single cells are poorly organised. Their occurrence in time and space seems to be random which makes their forecast difficult. Whether or not and when the required trigger temperature will be reached in a certain region can be forecasted. However, when and where exactly a triggering process is induced and if then the ambient moisture content is sufficient to allow for deep convection cannot be predicted. The short life character of these isolated cells even increase the difficulty of their prediction.

Multicell. This type describes thunderstorm cells that emerge and develop in clusters or lines. They are typically self-sustaining, as new cell generation is triggered by the existing cells, what will be detailed in Section 2.3.3. Each cell in the cluster behaves individually with a lifetime of about 20 minutes while the whole system may move as a unit. Line arrangements, so called squall lines are often, but not exclusively, related to cold fronts, develop on or ahead of it and travel with the front. As multicells in general, the line structure may persist for several hours as the cold outflow ahead of the line forces the warm unstable air to feed the updraught and keep the squall line alive. It may have a great extent of up to several hundred kilometres along the front and travels perpendicular to its line orientation (ZINNER and GROENEMEIJER 2012). The multicell dissipates when the formation of new cells ended, e. g. due to a lack of moisture or lift, and the last cell disappeared (ISRAËL 1964). During their lifetime, individual cells or other cell cluster may merge and split again.

Such systems often incorporate severe weather including heavy rain, moderate-sized hail and strong downbursts. Tornadoes can be expected (BYERS and BRAHAM 1949).

Many multicells follow from single cells. Therefore, their general predictability is equally limited. In contrast to that, the occurrence of some multicells, such as squall lines, is often related to larger scale processes in the atmosphere. As these processes are forecastable, also the associated thunderstorm arrangements are rather predictable than single cell storms, especially regarding their movement and lifetime.

Supercell. A supercell is a rare but long-living thunderstorm that is organised around one strong central updraught which is rotating in contrast to the types discussed before. The rotating updraught is also called a mesocyclone and is responsible for the timely stability of the cell. It supports the production of extreme severe weather with heavy rainfall including large-sized hail, strong downbursts and tornadoes (BYERS and BRAHAM 1949).

2.3.3 Self-sustaining thunderstorm development and resulting effects

The cold outflow of a single thunderstorm cell interacts with the environmental condition, may reinforce triggering processes and, thus, enable the emergence of new cells as visualised in a 2D vertical cross section in Figure 2.3.

While the front spreads out horizontally in all directions, it interacts differently with the met surrounding conditions. Typically one can find shear in the lower atmosphere which

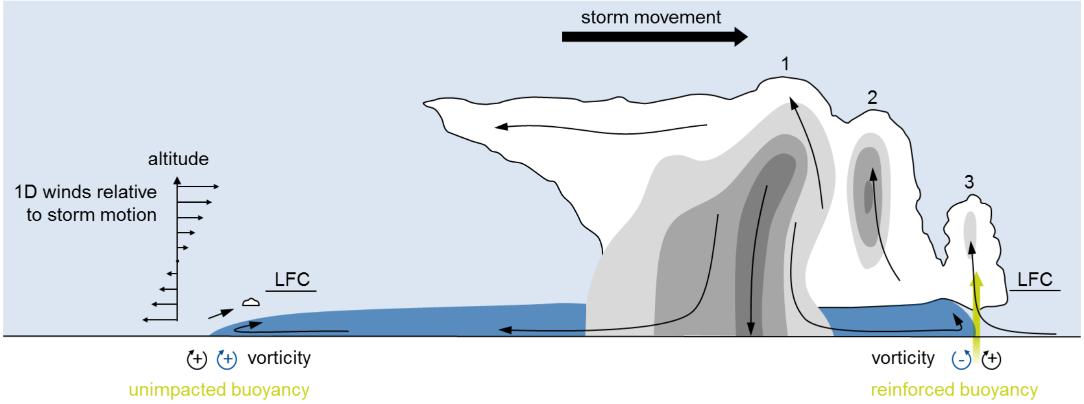

Figure 2.3: Generation of new cells in a multicell in a shear situation (left). Clouds are white, with rain and hail indicated in grey. The mean movement of the three included cells is to the east. The most right of which is just about to emerge, triggered by the cold pool (blue) of the gust front with indicated streamlines (arrows). Converging air rises on the leading edge of the gust front what is additionally supported by vorticity resulting from shear (black circular arrow) and the cold outstreaming air (blue one). Based on MARKOWSKI and RICHARDSON (2010).

is due to friction at the ground (ETLING 2008). Thus, surface winds are rotated and might be opposite to the mean motion of the cells. Vorticity induced by the environmental wind shear as well as such due to the cold pool of air in the gust from mature cell 1 is indicated by black and blue circular arrows, respectively. When these are opposed they reinforce buoyancy and support lifting of air to the LFC (MARKOWSKI and RICHARDSON 2010). Free convection starts and a new cell (1) forms.

Having started from a single cell, a multicell emerges that grows mainly with the number of simultaneously existing cells. Each cell traverse through the cluster while undergoing the typical life cycle of thunderstorm cells until it dissipates on the opposite edge. The multicell is self-sustaining as long as the environmental conditions provide moisture. From radar data analyses it was found that the maximum height attained by each successive cell in a multicell increases (BYERS and BRAHAM 1949).

Each individual cell of such a cluster moves with the mean wind at steering level which is usually in a height of 500 hPa (HAUF *et al.* 2013). However, observations show that new cells often emerge on the leading right flank of the cluster, are in the mature stage while crossing the centre of the cluster and dissipate at its left flank as shown in Figure 2.4.

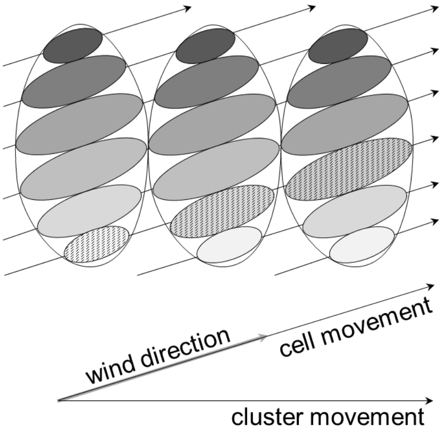

Figure 2.4: Scheme of an analysed multicell storm indicating cell and storm motion as well as wind direction (based on MARWITZ (1972)). New cells (light objects) develop on the right flank of the cluster and seem to travel through it (dotted area) while maturing (darkling blue) until they dissipate on the left flank. Due to new emerging cells the overall storm movement is deviated to the right of individual cell motion.

Pressure gradient forces as well as linear and non-linear effects are discussed as being responsible for this characteristic cell generation location. For further reading please refer to e. g. WEISMAN and ROTUNNO (2000), DAVIES-JONES (2002) and BLUESTEIN (2013) as well as references given there.

Due to the characteristic location of cell generation the storm motion given by the entire cluster varies from the individual cell movement direction. Independent from the actual wind direction the cluster motion is deviated to the right of the cells motion as analysed by MARWITZ (1972) who based the study on BROWNING and LUDLAM (1960). Cells behaving as described before are referred to as right movers. Occasionally left movers are observable (BROWNING 1986).

Apart from the general uncertainty of the onset of thunderstorms their evolution is individual and might differ from the mean life cycle. Depending on the environmental condition uncertainty in storm size and movement – direction and speed – as well as in its individual lifetime differs. Moreover, uncertainty varies with the geographical location. In some region on earth, as e. g. along the inner tropical convergence zone (ITCZ), thunderstorms occur regularly as the main ingredients – moisture, lift and instability – are abundant. In other places they only occur occasionally. Techniques to monitor thunderstorms and gain information that facilitates nowcasting are presented in the following.

2.4 Monitoring of thunderstorms

To monitor deep convection and thunderstorms several devices can be used. Ground-based as well as airborne radar measurements enable identifying intense cells according to their strong reflectivity which is given by numerous large and scattering rain drops and hail stones. Satellite observations allow additionally for early detection of just developing cells. In turn, lightning detectors help to monitor the development of mature and active parts of thunderstorm areas. A short insight in available measurement principles is given as follows.

2.4.1 Weather radar observations

Monitoring the atmosphere concerning precipitation and associated meteorological phenomena like severe thunderstorms is of interest of many people and required in order to issue warnings in a timely manner. Radio detection and ranging (radar) measurements provide a detailed view on hydrometeors in the atmosphere. Precipitation components like drizzle – the smallest falling droplets with diameters between ~ 0.2 mm (AMS 2012a) and 0.5 mm (AMS 2012b) –, dry snow, dry hail, wet snow, rain and wet hail act as scattering objects to radar signals in microwave frequencies, as e. g. 3000 MHz (S-band) and 10000 MHz (X-band). The intensity of the returning signal is directly proportional to the size and amount of scatterer. Thus, the return is increasing according to the list order above (AIRBUS 2007).

In order to convert the return signal given by the reflectivity Z to the rainfall rate R a basic $Z - R$ relation is applied (GEÇER 2005):

$$Z = a \cdot R^b \qquad \rightarrow \qquad R = \left(\frac{Z}{a}\right)^{\frac{1}{b}} \tag{2.3}$$

with constants a and b specific for the radar system and dependent on the assumed droplet size distribution which varies with the atmospheric precipitation phenomenon (e. g. thunderstorm: $a = 500$ and $b = 1.5$ defined by JOSS *et al.* (1970) or $a = 486$ and $b = 1.37$ defined by JONES (1956)).

Ground based radar observations enable to extensively imaging the spatial distribution of hydrometeors. Different radar modes and scanning methods can be applied to allow for monitoring multiple properties of precipitation in the atmosphere. Either pure information on precipitation kind and intensity can be obtained or Doppler shifts are additionally analysed to evaluate the radial velocity of the scattering objects relative to the radar (DWD 2011). The latter are especially valuable when monitoring atmospheric phenomena associated with circulating winds such as for instance storm cells with radially spreading outflows at the surface as well as tornadoes or hurricane spiral bands (CoCoRaHS n. Y.).

The scanning procedure can be varied so that specific information can be deducted. In so called PPI (Plan Position Indicator) scans the area around the device is monitored along a fixed elevated path of the signal. Variation of the elevation enables to obtain volume information up to 12 km height. A full scan, however, takes 15 minutes and, thus, may scan different cell stages of a short living thunderstorm (DWD 2011). A rapid vertical scan, referred to as Range Height Indicator (RHI) may provide vertical cross sections of individual cells. Based on this method, structure and properties of the cell, such as its maximum altitude can be analysed to evaluate whether overflying could be an option (Geçer 2005). Different radar products are deducted from such scans. One among others is the so called CAPPI (Constant Altitude Plan Position Indicator) product that extracts data from the volume scan and maps the situation in a constant altitude (Douglas 1990). As the range of a single radar system is between 120 km and 230 km for Doppler and intensity mode, respectively, radar composites are created. These achieve a complete coverage of a region by composing measurements of several devices to a single image (DWD 2011).

Airborne weather radar systems allow for a steady monitoring of the always current situation ahead of the aircraft as shown in Figure 2.5(a) (Airbus 2007). It supplements the poor weather information obtained by the flight dispatcher before departure. That information is often already obsolete or in case of significant weather (SigWX) charts feature only low timely and spatial resolution regarding convective weather. ATIS (Automatic Terminal Information Service) or VOLMET (meteorological information for aircraft in flight) inform the crew in flight about potential weather. Ground based radar information is not available for pilots in flight as data-link techniques and their capacity are limited to provide steady radar information uplinks to the cockpit.

The weather radar device, placed in the nose of the aircraft – the radome below the cockpit – performs PPI scans. It covers a circular segment with a horizontal opening angle between 90° and 120° ahead of the aircraft (Higdon 2008 - 09). In this segment the radar provides information on the horizontal cross section of the cell in a limited vertical range. The latter is determined by the radar beam width, which is several degrees, and the distance to the cell as shown in Figure 2.5(a).

Depending on the antenna size, scan ranges of up to 240 NM or 320 NM (Higdon 2008 - 09), flown through in less than 40 minutes at a speed of 250 $\mathrm{m\,s^{-1}}$ ae reached. However, ranges of 80 to 200 NM are typically set. The range as well as antenna tilt and radar gain can be individually modified in order to reveal certain characteristics. So, for instance, sensitivity can be reduced by varying the radar gain which widens the beam (Trammell 2010). As a result, only cells exceeding certain reflectivities are displayed in the cockpit

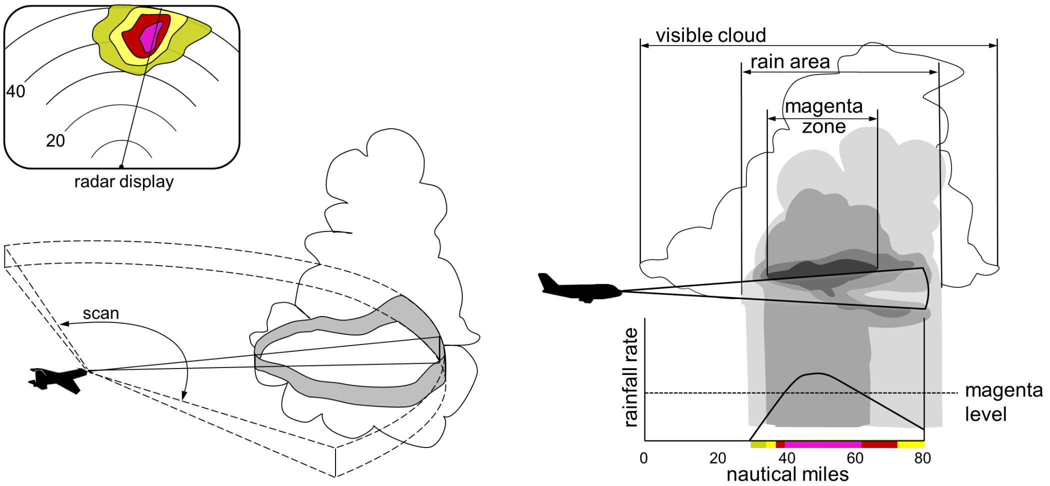

(a) Airborne weather radar scanning a slice of a thunderstorm cell.

(b) Radar return signal of a cloud mass along track.

Figure 2.5: Airborne weather radar measurements. (a) Horizontal scanning of a slice of a thunderstorm cell and visualisation in the on-board radar display. The black line represents the current radar path. (b) Different echo intensities of a cloud mass. Both figures are based on HONEYWELL (2006).

(HONEYWELL 2006). Otherwise, a calibrated colour scale (green, yellow, red, magenta) indicates increasing intensity reflected by areas where snow, ice crystals, wet turbulence, rainfall and hail occur, respectively (AIRBUS 2007). An example of a cell scan is shown in Figure 2.5(b). Respective rain rates and expected turbulence when encountering these areas are given in Figure 2.6(a). Typically, a reflectivity of 37 dBZ (= 8.1 mm h^{-1}) is rated by pilots as being worth to avoid (TAFFERNER and FORSTER 2012).

Equal to ground based radar observations, measurements can be influenced by the thunderstorm situation itself. Intense cells with heavy precipitation (magenta level in Figure 2.6(a)) may attenuate the signal significantly or block the return completely and, thus, conceal even stronger weather. The return signal is then weak in aft parts indicating only minor risk areas (AIRBUS 2007). A manual setting of the device also incorporates the risk to not detect certain characteristics. Reducing the displayed radar range, for instance, may lead to a blind alley effect visualised in Figure 2.6(c). Compared to the complete situation given in Figure 2.6(b), the blocking structure behind the two smaller cells is not recognised so that the route straight ahead seems to be safe (HONEYWELL 2006).

When being used correctly (e. g. according to guidelines provided by AIRBUS 2007), the on-board radar provides valuable information and enables weather avoidance. Navigation through a field of convective cells is not recommended. Instead, the "line of least risk" is the route that should be followed when avoiding cells in-flight based on weather radar (SKYBRARY AVIATION SAFETY 2013).

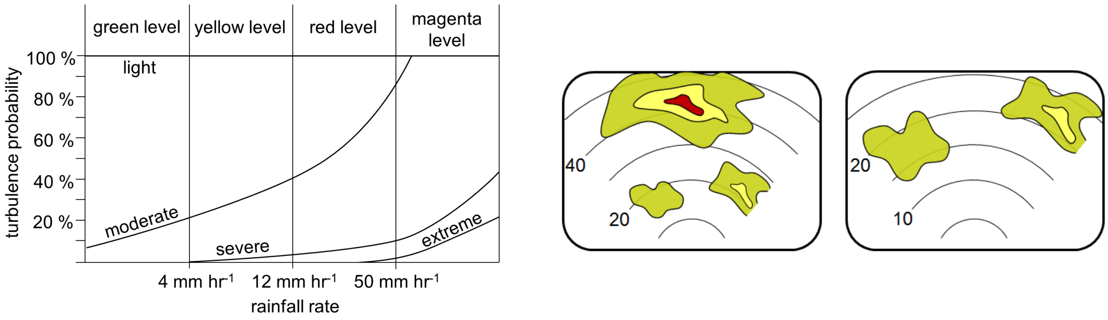

(a) Turbulence probability. (b) Long range setting. (c) Short range setting.

Figure 2.6: (a) Probability of encountering different turbulence intensities in certain rain rate classes and radar levels. (b) A normal range setting of the on-board radar device enables early risk identification. (c) Blind alley effect that may emerge from a short-range setting. All Figures based on HONEYWELL (2006).

2.4.2 Lightning detection

So called stormscopes detect the electrical activity of a cell even though no visually recognisable lightning strike is observable (BFGOODRICH AEROSPACE 1997). Information provided by these either ground-based or airborne passive devices supplement radar measurements. They use radio direction-finding techniques and analyse characteristic frequencies emitted by lightning as well as their attenuation relative to a reference signal. Thereby distance and direction of discharges are located and displayed in real time within a range scalable from 25 NM up to 200 NM around the aircraft (HIGDON 2008 - 09). The previously discussed blind alley effect holds equivalently for stormscope displays.

2.4.3 Satellite observations

Satellite observations provide a top view on earth, are able to identify clouds and, thus, give information on their tops. Eleven geostationary meteorological satellites orbiting the earth in an altitude of 35880 km above respective points on the equator while providing images for different regions.

A Spinning Enhanced Visible and Infra-Red Imager (SEVIRI) imaging radiometer on the newest European operational Meteosat Second Generation satellite (Meteosat-10) scans the full disc of the earth in 12 spectral channels, some of which in the visual others in the infra-red (IR) spectrum (SCHMETZ *et al.* 2002).

Compared to radar observations, convection monitoring based on satellite images enables meteorologists to identify convective cells in all stages (at least during daytime) starting with the initial instability of the atmosphere to the mature cell and its properties. A carefully selected channel combination enables to identify and tease certain information on convective cell stages. An overview of applied channel combinations for detection of cells and further processing in the cumulonimbus tracking and monitoring algorithm Cb-TRAM can be found in STICH (2012), who summed up and supplemented information given by ZINNER and BETZ (2009).

Data-link techniques for weather data provision to the cockpit are currently investigated. It should enable up-linking of small packages of tailored data to provide an enlarged view and enhance the situational awareness of pilots (HIGDON 2008 - 09). First tests to upload observational as well as nowcast data to electronic flight bags (EFB) of airborne aircraft crossing the ITCZ were evaluated by pilots as being beneficial. This information helped to find a gap in the band of deep convection, however, pilots still must confirm the recognised information of the sent data by those observe with the on-board radar. Nevertheless, a targeted search for a gap became possible and extreme detours that may have led to fuel shortages were prevented (STICH *et al.* 2013)

In general, information on the future development of thunderstorms is welcomed by pilots and the ATM community in order to optimise trajectories earlier than on short notice. Time horizons of up to two hours (MCNALLY *et al.* 2015) are of special interest to enhance traffic flow and decrease delays significantly. If, however, accurate thunderstorm nowcasts, which will be introduced in Section 2.5, will become available for such time horizons in spite of the previously discussed uncertainties, remains to be seen.

In addition to pure weather information provision by data-links, routing suggestions in such situations may even facilitate safe and efficient manoeuvres to avoid hazardous airspaces. Mutual understanding of pilots and ATC is enhanced if all stakeholders receive the same information. Path-finding algorithms and avoidance route models can be applied to generate this information. A short overview as well as an introduction to one of such models, the adverse weather diversion model DIVMET, is given in Chapter 4.

2.5 Thunderstorm nowcasting

Numerical weather prediction (NWP) usually provides forecasts for various meteorological parameters and several days. Its suitability, however, varies with the scale of the considered phenomena. Thunderstorms with their small scale occurrence in time and space are, however, not or only in parts explicitly resolvable on spatial grids of several kilometres (minimum 2.8 km in local models) applied in NWP as indicated in Figure 2.7(a). Thus, convection is a sub-grid process that is introduced by parametrisation, i. e. consideration of a statistical feature (HEISE 2002). Moreover, NWP is identified as being an initial value problem (BJERKNES 1904). A good forecast, thus, depends on the assimilated initial data set. This, however, is never complete and 100 % perfect (WILKS 2011). Especially information on small scale features like convection is missing. Its integration via radar data in local models is only recently investigated (DWD 2015a). Due to the use of a set of non-linear partial differential equations, to which some simplifications are applied in order to make them resolvable, small errors in the initial conditions may grow to finite size. The smaller the scale of the process or phenomenon, the larger is the growths rate, which holds especially for thunderstorms (CRAIG 2012).

Processes not covered in the initial data need to be created by the model itself in the so called spin-up time which is about six hours. In that time horizon NWP is usually

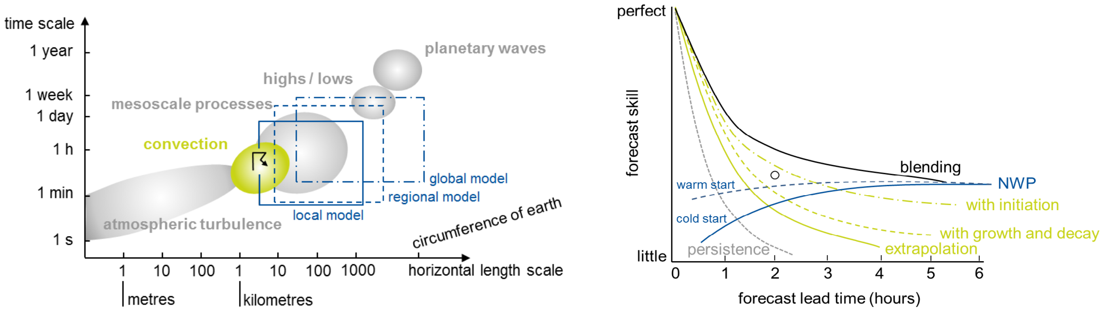

(a) Scales of atmospheric processes in NWP.

(b) Forecast skill of nowcast and NWP.

Figure 2.7: (a) Scales of atmospheric processes (bubbles) and scales covered in different NWP models (boxes) (adapted from DWD 2015b). (b) Forecast skill of different nowcast (green lines) and NWP (blue lines, 'warm start' indicates models that assimilate radar data) techniques over lead time. A blending (black line) of both forecast types may facilitate a much better thunderstorm prediction in the transition time from the superior nowcast in early hours to NWP mastering after hours. Blending of several data and model sources in CoSPA results in a 2-hours forecast skill given by the black circle (adapted from Wolfson *et al.* 2008).

not reliable (Wilson *et al.* 1998). Afterwards, regarding convection, the model output allows for identification whether or not the atmospheric condition in principle features the required ingredients. When and where exactly triggering occurs is mostly determined by much smaller scales and is thus not predictable. Even the application of ensemble prediction systems (EPS)[1] does not help in this issue. It only increases certainty on the region where convection possibly occurs.

Apart from the forecast horizons of hours and days, detailed information on small-scale phenomena like individual thunderstorms with an average lifetime of about 20 minutes is of interest on short time horizons (Wilson *et al.* 1998). For that purpose, nowcasting is an appropriate technique that "comprises the detailed description of the current weather along with forecasts obtained by extrapolation for a period of 0 to 6 hours ahead" (WMO 2015). The analysis of individual structures in observational data enables forecasters and expert systems to predict the further development with reasonable accuracy on limited time scales. The particular strength of nowcast products, as mentioned by WMO (2015), is due to their location-specific ability to provide information on storm initiation, growth, movement and dissipation.

2.5.1 Nowcast techniques

Based on observational data obtained by the previously introduced primary tools like weather radar, satellite imagery and lightning detectors, nowcast systems perform short-term forecasts (Wilson *et al.* 1998). Because of thunderstorms being quickly evolving

---

[1] EPS are based on several model runs of the same or various NWP models with slightly modified initial conditions or varied model physics. Such systems aim to sample the possible range of solutions which is introduced by the incomplete and inaccurate initial information and simplifications in the numerical calculation. At the same time it tends to represent the chaotic behaviour of the atmosphere. For further information on ensemble prediction see e. g. Wilks (2011), Coiffier (2011) and Craig (2012).

and vanishing meteorological phenomena, initiation data with high spatial and temporal resolution is meaningful. Most nowcast systems use extrapolation techniques obtained by analyses of recent observational images which are then applied to the latest identified structures. Different extrapolation methods are shortly introduced in the following. A detailed overview on nowcast evolution and milestones can be found in WILSON *et al.* (1998).

Persistence method. This is the simplest form of a nowcast. It assumes exactly the same situation present in the data for any future time. Neither any shifting nor changing is considered and the situation is first redefined with new observational data (MAZALEVSKIS *et al.* 2013).

Advection method which is also referred to as steady-state assumption by WILSON *et al.* (1998) accounts for an object shift with its propagation speed. Thunderstorms mostly move with the mean wind that is approximately equal to wind speed in the 500 hPa level (HAUF *et al.* 2013). In this method at least two subsequent digitised radar or satellite images taken at different times t_{-1} and t_0 are correlated and a mean motion vector of the echo is determined either by cross-correlation or the displacement of the cell gravity centre. The found vector is then applied to the latest observed gravity centre position to further shift the latest shape of a cell, which remains as observed, for future times. So again no change in size or intensity is considered (WILSON *et al.* 1998). Reapplication of the vector to the nowcast creates additional lead times (MAZALEVSKIS *et al.* 2013).

Morphing method. Instead of a single mean motion vector, a field, consisting of individual vectors, one for each pixel, is determined by image processing. Applying the vector motion field to the latest images shifts each pixel individually. Thus, growing and shrinking processes, if identified before, can be nowcasted (MAZALEVSKIS *et al.* 2013). Size trending is the terminology originally used by WILSON *et al.* (1998) who summarised early studies from the late 20th century that showed only minor improvements by this feature. Nowadays several systems, one of which is Rad-TRAM which will be detailed in Section 2.5.2, use this methodology.

Depending on the nowcast technique the forecast skill drops at different rates as shown in Figure 2.7(b). Nowcasting (green lines) is superior to NWP in the tactical phase, i. e. the first hours (BOWLER *et al.* 2006, KOBER *et al.* 2012). However, NWP (blue lines) starts mastering the thunderstorm forecast skill after some hours when the model is spun-up. Due to the fact that nowcast systems are based upon observational data products, mostly provided by either radar or satellite measurements that are limited to certain regions, a large number of such systems is under development or in operation and run for the respective limited region. Some of which are, for instance, the Short-range Warning of Intense Rainstorms in Localized Systems (SWIRLS) operated by Hong Kong Observatory

(LI *et al.* 2000), NCAR's Thunderstorm Identification, Tracking, Analysis, and Nowcasting system TITAN (DIXON and WIENER 1993), the Radar Tracking and Monitoring (Rad-TRAM) system developed at DLR and operated at DWD as well as the there developed system KONRAD (*Konvektive Entwicklung in Radarprodukten*, convective development in radar products). All of the former systems are based on radar data, use 2D or 3D information and account for different detail levels. Cb-TRAM is DLR's equivalent system based on satellite data.

Further systems, such as the NowCastMIX product of DWD, combine several observations, nowcasts and model output statistics (MOS, GLAHN and LOWRY (1972)) applied to NWP while providing nowcasts up to 2 hours ahead (HOFFMANN 2008, DWD 2014). Blending techniques of nowcasts and NWP are also applied in the GANDOLF (Generating Advanced Nowcasts for Deployment in Operational Land surface Flood forecasting) tool that uses nowcasts provided by NIMROD (Nowcasting and Initialization for Modeling using Regional Observation Data) (PIERCE *et al.* 2000). Both tools are developed at UK Met Office, apply a conceptual life cycle model and provide predictions of deep convection for 3 to 6 hours ahead (HAND 1996).

Such a blending of extrapolation techniques and NWP, as done in these models is currently under elaboration in several tools to close the gap that exists between nowcasting (one to three hours) and NWP with spin-up times of six hours. The approach is to gradually combine radar-based, or more general observation-based nowcasting in the first hours with probabilistic NWP later on to provide better forecasts in the transition hours (KOBER *et al.* 2012). In the US, large effort on this topic is already made in CoSPA (Consolidated Storm Prediction System) for storm prediction in horizons of 0 to 8 hours (WOLFSON *et al.* 2008, PINTO *et al.* 2010).

Insights and examples of blending techniques are provided by (HWANG *et al.* 2015). An overview on nowcast systems is given by WILSON *et al.* (1998). Further on, an introduction to one of such nowcast systems, namely Rad-TRAM, is given as it provided data for the analysis presented in Chapter 3.

2.5.2 The Rad-TRAM nowcast system

At the Institute of Atmospheric Physics at DLR thunderstorm nowcasting is investigated for years. The purpose was to develop an intuitive representation of hazardous areas to aviation posed by thunderstorms. The latter are referred to as weather objects that can be divided into top and bottom volumes as shown in Figure 2.8.

Top volumes are extracted from Meteosat-10 SEVIRI satellite data by Cb-TRAM, the Cumulonimbus Tracking and Monitoring algorithm. Different channel combinations, detailed by STICH (2012) and based on ZINNER, MANNSTEIN and TAFFERNER (2008), allow for automatic detection of three different stages of thunderstorm development: (1) convection initiation, (2) rapid vertical development and (3) mature stage (FORSTER and TAFFERNER 2012). Such identified cells are then tracked in subsequent images and nowcasted up to one hour ahead as detailed below.

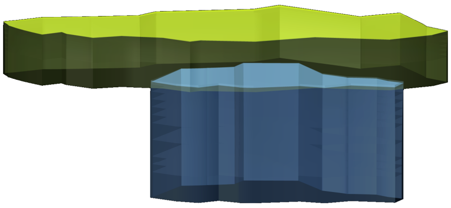

Figure 2.8: Top and bottom volumes of a thunderstorm as provided by Cb-TRAM and Rad-TRAM, respectively (based on SCHARF 2013).

The radar tracking and monitoring (Rad-TRAM) nowcast system provides information on bottom volumes extracted from ground-based radar products that reveal intense rain areas. Cells with a reflectivity higher than 37.0 dBZ are identified and extracted, as shown by black contours in Figure 2.9 (FORSTER and TAFFERNER 2012). Pilots mostly avoid cells of this intensity as they often incorporate moderate to heavy rain, hail and turbulence. These bottom volumes identified by Rad-TRAM represent hazards especially relevant for landing and take-off (LAU 2012). Nevertheless, they indicate the existence of deep convection which typically reaches up to high altitude.

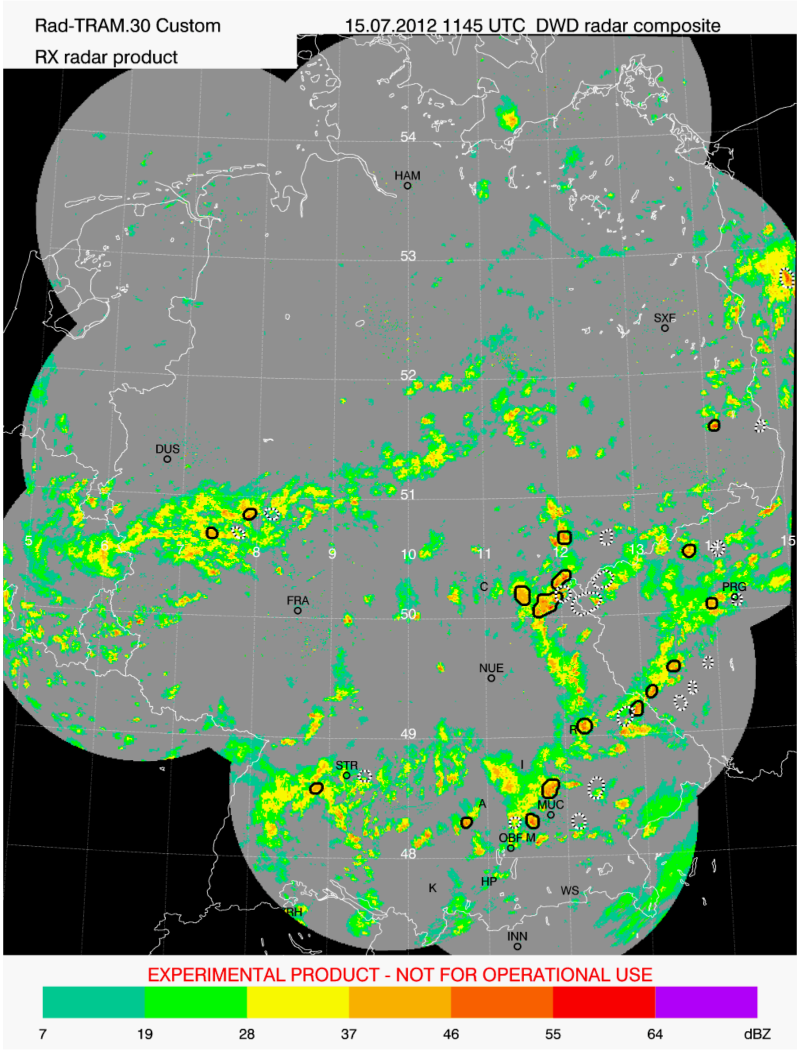

Figure 2.9: The Rad-TRAM product providing information on bottom volumes overlaid to the colour-coded DWD radar product of 1145 UTC at 15 July 2012. Detected cells are given by solid black contours. Dashed contours represent nowcasts with a lead time of 30 minutes (FORSTER 2015).

Cells of a size of at least three pixels are considered and extended to 21 pixels by applying a circular smoothing. The latter technique also accounts for smoothing of the cells edges (see difference between orange patches and black contour in Fig. 2.9), to avoid a suggestion of such a detailed knowledge about the hazardous area (KOBER and TAFFERNER 2009).

Depending on the applied product, resolution and update rate vary. Rad-TRAM data used in this study are based on the extended German radar composite (RX product) issued by DWD. The radar product gives radar reflectivities in dBZ with a horizontal resolution of 1 km x 1 km obtained in surveillance scans at lowest elevation by various radar devices across Germany and bordering areas (DWD n. Y.). An updated RX product is published every 5 minutes and serves as input for Rad-TRAM (DLR n. Y.).

Both algorithms, Cb-TRAM and Rad-TRAM, process three steps with the object-based data: Detection, tracking and nowcasting. First, the detection depends on the product and was already discussed. Secondly, a pixel-based motion field is determined based on subsequent radar images covering a time span of 30 minutes. A *pyramidal image matcher* was developed to account for different, especially small, scale developments within a cell (KOBER and TAFFERNER 2009). Starting with a coarse resolution of subsequent pictures, larger pixels are correlated and the motion vector is determined. An approximate match is obtained by displacing all pixels according to the just found vectors. The vector field is then revised for still existing fine-scale differences. To do so, the resolution is stepwise increased to identify the individual motion of smaller pixels. For further details on the distinct description of the procedure, please refer to ZINNER *et al.* (2008). In the third step, the derived motion vector field is applied to the detected cells and a short range forecast is generated that provides deterministic cell contours in a spatial resolution of 2 km x 2 km for up to 60 minutes ahead (FORSTER and TAFFERNER 2012). Characteristic attributes like moving speed and direction as well as the gravity centre are provided with each cell contour in XML format files (LAU 2012). A cell-specific ID allows for tracking and life cycle identification of individual cells as shown in Figure 2.10. Blue filled objects show all subsequently detected stages of a cell that was first observed at 08:45 CEST on 15 July 2012. To each detected cell stage, i. e. every 5 minutes, a nowcast set consisting of twelve lead times between 5 and 60 minutes is issued and given by grey objects in the respective column. Cell dissipation in the meantime is not considered. Ultimately, the nowcast set includes predictions for times at which the actual cell is not detected any more (light grey). Cell dissipation in the observational data set might either be due to the fact that the cell intensity has weakened below an equivalent reflectivity of 37 dBZ or because it merged with another, larger cell. Merging as well as splitting processes are detected in the image matching procedure. The former ID of a splitting cluster remains with the largest resulting cell while new IDs are created for other cells. If two or more cells merge, the ID of the largest continue whereas such of the smaller merging cells are discarded. The latter seems to dissipate from the data set, however, it is listed with another ID further on (KOBER 2006).

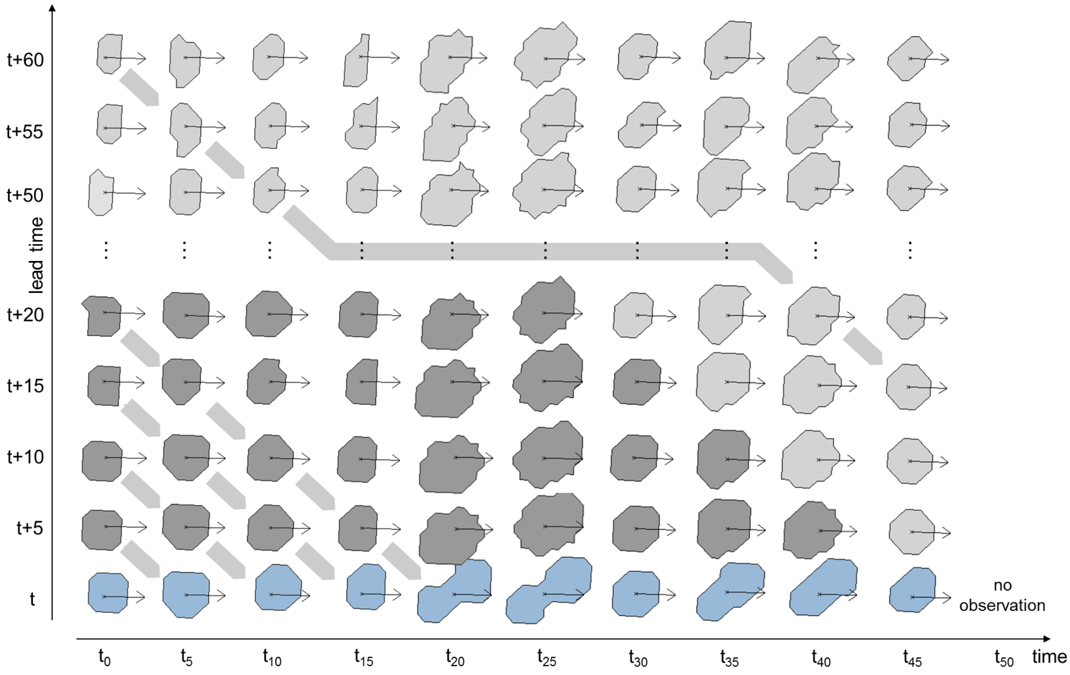

Figure 2.10: For each observed cell (e. g. left blue object in bottom row) twelve stages for lead times between 5 and 60 minutes (grey cells in column above) are nowcasted by Rad-TRAM. With each cell gravity centre (cross) and movement direction (arrow) are provided. The set of nowcasts is updated when the new observation (next column) is published every 5 minutes. The blue objects show a life cycle of a cell observed between 08:45 UTC and 09:30 UTC on 15 July 2012. Seems as if the cell has merged with another one in the fifth observation (after about 20 minutes) and split again after 25 to 30 minutes. Whether the cell weakened below the threshold of 37 dBZ or if it merged with another, larger cell, does not come out of the data. Bold grey arrows reveal related cells. Nowcasts for lead times when the actual cell is not any more detected as such are marked in light grey. Dark grey indicates nowcasted stages for lead times at which a actually detected cell exists. Based on SAUER *et al.* (2014, 2015a).

Further information on Rad-TRAM can be found in TAFFERNER and FORSTER (2012) and FORSTER and TAFFERNER (2012).

2.5.3 Thunderstorm nowcast verification

Verification of a forecast or nowcast gives information on the quality of the applied system. Numerous verification methods have been developed that all are based on comparisons of a forecast and the related observation. Measures that describe the relationship of both are used to evaluate the quality of a nowcast product (WILKS 2011). For binary forecasts (yes/no) like such provided by Rad-TRAM, to which WILKS (2011) refers as "non-probabilistic and discrete" (p. 306), mainly 2 x 2 contingency tables are applied (see Fig. 2.11(a)). According to FORSTER and TAFFERNER (2012) either object-to-object or pixel-to-pixel comparisons are performed as visualised in Figures 2.11(b) and (c).

In the object-based analysis (Fig. 2.11(b)) a hit (green) is counted if nowcast and observation do overlap. Otherwise the observation is regarded as a miss (blue) and the nowcast counts as a false alarm (grey). When applying a pixel-based analysis all three categories may emerge in the comparison of nowcast and observation of one object. This way, a

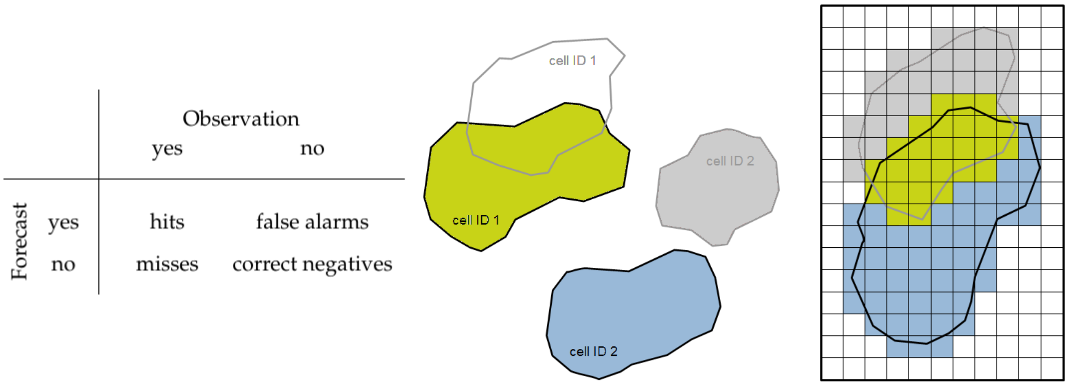

(a) Contingency table. (b) Object-based verification. (c) Pixel-based verification.

Figure 2.11: Rad-TRAM verification based on (a) a contingency table method while accounting for an either (b) object- or (c) pixel-based comparison of nowcasted (grey contour) and observed (black contour) object. Hits, misses and false alarms are indicated in green, grey and blue, respectively. Based on FORSTER and TAFFERNER (2012).

double penalty, once for missing parts of the observation and again for false alarms is imposed to the nowcast (GILLELAND *et al.* 2009).

The fourth member of the contingency table is a correct rejection or correct negative. However, when forecasting rare events as deep convection, it is common to only forecast the event instead of also explicitly predicting no-event cases. Thus, correct negatives are either not given or would be of magnitudes larger than the other entries, if forecasted (STICH 2012 based on JOLLIFFE and STEPHENSON (2003)). Several quality measures without correct negatives can be derived by relating the remaining members (WILKS 2011). Such used by FORSTER and TAFFERNER (2012) for validation of Rad-TRAM are:

- Probability of detection $POD = \frac{hits}{hits+misses}$
  which is the fraction of correctly forecasted events. The perfect score is 1.

- False alarm ratio $FAR = \frac{false\,alarms}{hits+false\,alarms}$
  is the fraction of the forecasted events not observed which ideally approaches 0.

A Rad-TRAM nowcast evaluation was based on all thunderstorm days in 2011. Results of *POD* and *FAR* for four different lead times and object-as well as pixel-based analyses are presented in Table 2.1. Recognisable from all modes is a decreasing nowcast quality with lead time (*POD* declines, *FAR* increases). Best results are presented in the second row. These are obtained by accounting for only those cells for which a nowcast was available. This means, all first detections of a cell, i. e. its transgression of 37 dBZ, are not considered here as these do not have a former related nowcast. These cells were regarded as misses in the regular evaluation. The modification lead to weaker criteria and, thus, increases the skill scores. Strongest criteria, namely a perfect match is required in the pixel-based analysis. In that light FORSTER and TAFFERNER (2012) rank even these results as being still encouraging.

Table 2.1: Verification skill measures *POD* and *FAR* of a Rad-TRAM data set covering all thunderstorm days of 2011 (data extracted from FORSTER and TAFFERNER 2012).

	lead time [minutes]			
	15	30	45	60
POD / *FAR* object-based	0.74 / 0.25	0.65 / 0.35	0.56 / 0.43	0.48 / 0.52
POD / *FAR* object-based, pairs	0.98 / 0.01	0.95 / 0.03	0.89 / 0.09	0.75 / 0.23
POD / *FAR* pixel-based	0.65 / 0.36	0.47 / 0.53	0.34 / 0.65	0.27 / 0.73

However, according to GILLELAND *et al.* (2009) the "double penalty can become problematic in judging the true quality of a forecast" (p. 1417). The authors remark that inflation of the spatial extent of a feature may resist the penalty of small differences and even lead to better scores. (STICH *et al.* 2013) applied a method of fuzzy verification by adding a search radius of 20 km around cells nowcasted by Rad-TRAM for 15-minutes lead time (50 km for 60-minutes lead time) in which an overlap would still be rated as a hit. For cells in the initial stage another method had been applied as these are often quasi-stationary, whereas Rad-TRAM applies the determined motion vector field and, thus, displaces the nowcasts much faster than observed. Here the whole nowcast track, built of former nowcasts, is taken for overlap identification. In both variations the area is significantly enlarged to get a better verification result. Nevertheless, the result is a single value – an overall skill score, which, as identified by (DROSDOWSKY and ZHANG 2003), is not always sufficient. Forecast skills will rather vary temporally or spatially.

GILLELAND *et al.* (2009) refer to the former methods as traditional verification scores, for which comprehensive overviews are given by JOLLIFFE and STEPHENSON (2003) and WILKS (2011). New technologies are developed that especially focus on spatial verification of gridded forecast and observational data. GILLELAND *et al.* (2009) group the wide variety of new methods in four categories: 1) neighbourhood or fuzzy, 2) scale separation, 3) feature-/object-based and 4) field deformation. While the first two categories mainly include filter methods, those in classes 3 and 4 aim to "fit the forecast to the observation as well as possible" (ib. p. 1417). One of such feature-based techniques is the Method of Object-based Diagnostic Evaluation (MODE) which relates forecasted and observed objects extracted from 2D fields even if they do not overlap. Therefore, no forecast skill would have been attested by traditional scores. Instead, MODE applies fuzzy logic and defines a score referred to as *total interest*. It combines a number of derived parameters among which the minimum boundary distance, the overlap area, the separation of object centroids as well as the object orientation relative to the grid (see Fig. 2.12) are related. Nevertheless, the final output is again a one-value score (DAVIS *et al.* 2009).

Another feature based technique is developed by EBERT and MCBRIDE (2000). It is referred to as the Continuous Rain Area (CRA) approach in which the authors analyse intensity, area and location differences in longitudinal and latitudinal direction to identify systematic forecast errors from the sum of the mean square root of each parameters.

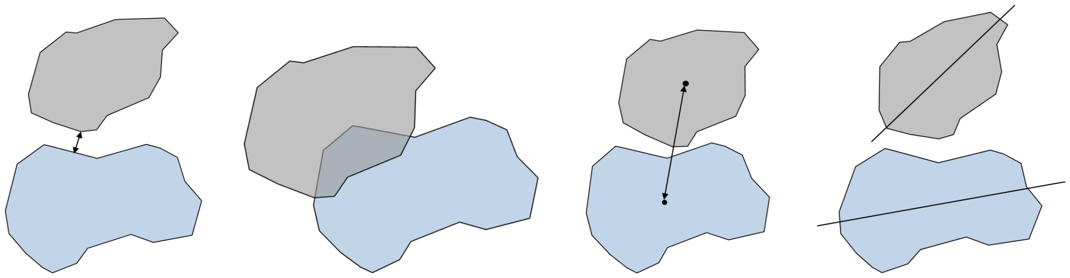

(a) Minimum boundary distance.

(b) Overlap.

(c) Centroid distance.

(d) Orientation.

Figure 2.12: Attributes of forecast (grey) and observation (blue) combined by fuzzy logic in MODE (based on GILLELAND *et al.* 2007).

In that method the displacement error is determined as a vector that results from moving the forecast over the observed field and searching for the best fit.

In contrast to that, field deformation verification techniques as such provided by (KEIL and CRAIG 2009) aim to manipulate the forecast by an optical flow field of distortion vectors so that the former appears like the observation. The forecast quality is then evaluated by metrics incorporating the vector field characteristics like amount of movement and intensity change (GILLELAND *et al.* 2009).

Nevertheless, all these as well as far more techniques summarised and referenced by GILLELAND *et al.* (2009), aim to score the forecast or nowcast quality by single values that enable to compared the performance of different systems while accounting for the individual uncertainty of such (GILLELAND *et al.* 2007). However, a general deduction of measures applicable to future nowcasts to account for and especially counteract the identified uncertainty is not included. This, however, is the objective of this study. Thus, a new method that is partially based on the former techniques is proposed in the following Chapter.

3 Analysis of a Rad-TRAM data set

A validation of the Rad-TRAM system has been performed by FORSTER and TAFFERNER (2012) based on traditional verification methods. An uncertainty determination accounting for the spatial displacement of the object edges of nowcast and later observation, however, has not yet been done. Thus, a general methodology of such an uncertainty evaluation for deterministic object-based nowcast and forecast techniques is presented in the scope of this thesis. It aims to identify measures applicable to the nowcast itself in order to facilitate consideration of nowcast uncertainty in aircraft routing. The proposed methodology is exemplary applied to a one-day Rad-TRAM data set provided by the Institute of Atmospheric Physics at DLR Oberpfaffenhofen, Germany.

After a short description of the data set and the respective weather situation, the methodology is detailed in this Chapter. Results regarding the identified uncertainty are discussed and a reasonable consideration of such in weather avoidance routing is presented.

3.1 Data set description

In 2012, between April and September, thunderstorms were recognised over Germany on 69 days, one of which is the 15 July (GARZ 2012). On this day the synoptic situation was dominated by several low pressure systems as can be seen in the surface weather map of 06:00 UTC (08:00 CEST) in Figure A.1 in the Appendix. The major low pressure system was located over the Northern Atlantic, a second large one over Northern Europe. A couple of others with much smaller extent were arranged east and south of Germany and adjacent areas covered by the used radar data (RX product) in Rad-TRAM. This area was influenced by inclement weather. As typical for air-mass-induced thunderstorms, plenty of small hyetal areas with embedded thunderstorms occurred kind of randomly distributed without any structural arrangement. Rad-TRAM detected 2857 objects exceeding reflectivities of 37 dBZ and clustered these in 563 individual cell life cycles. Cell tracks crossed the country eastwards (see gravity centre tracks given in Figure A.2 in the Appendix). According to GARZ (2012) the Rad-TRAM tool operated well and without any failure on that day and the propagation of thunderstorm nowcasts was evaluated as being of good agreement with observations.

The total number of cells detected at a time shows a typical daily course for air-mass thunderstorms, whose origin in convection initiation strongly depends on the available surface forcing. According to Figure A.3(a) in the Appendix, the total number of detected cells rises in the morning hours and alternates between about 15 to occasionally 25 in the period between 10:00 and 20:00 UTC. The detection of new cells supports this trend and is maximum between noon and the late afternoon when up to nine new cells are identified in a radar image updated at 5-minutes rates. Lifetime ranges of the newly detected cells are given in Figure A.3(b) but do not show any characteristic trend. It is assumed that the detection of a cell in a radar image is equivalent to a lifetime of 5 minutes, however, the cell might just have reached the required intensity threshold shortly before it is scanned and subsequently weakens again. Under this assumption and except of one cell cycle that lasts almost 300 minutes, maximum lifetimes stay below 200 minutes. Short lifetimes are much more frequent as recognisable in the bar plot provided in Figure 3.1. On 15 July 2012 cell lifetimes average to 25.4 minutes what is in good agreement with the literature (see e. g. BYERS and BRAHAM 1949). Blue points (related to the right ordinate) indicate the relative number of cells with the respective or a larger lifetime. 50 % off all cells disappeared already before being detected in the third subsequent radar image as indicated by the dotted distribution. The dashed exponential fit with $a \cdot e^{b \cdot c}$ is based on a non-linear least squares method. Its coefficients are given in the legend. The inverse of b reveals the so called time constant τ of the development, describing the time in which the distribution drops to $1/e \approx 36.8\,\%$ of the original value. It results in $\tau = 22.29$ minutes which is about the mean lifetime of the cells. A lifetime of at least 65 minutes, for which nowcasts are generated by Rad-TRAM according to the first detected cell stage, is reached by about 10 % of all cells. All other cells weaken below the threshold of 37 dBZ in the meantime.

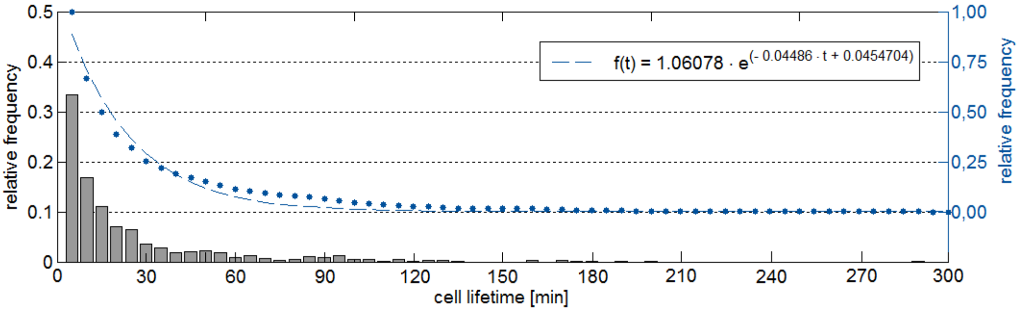

Figure 3.1: Lifetime distribution of all 563 cell life cycles (bars, left ordinate) and frequency of cells with lifetimes equal or larger than the respective value on the abscissa (points, right ordinate). An exponential fit of the latter distribution is given by the dashed blue line. Its formula with time t in minutes is given in the legend.

During their lifetime, cells typically undergo a cycle in size. Such cycles of observed cells are visualised in Figure A.4(a). Maximum cell areas of 1000 km^2 and 1200 km^2 are reached on the considered day. A scatter plot positively correlating the maximum cell size with its lifetime is presented in Figure A.4(b). The cell diameter averages to about 15 km (see each sides mean extent summarised in Tab. A.1 in the Appendix) and occasionally reaches values of 60 to above 80 km.

3.2 Methodology of nowcast uncertainty determination

The deterministic and object-based nowcasts of thunderstorm cells, exemplary provided by Rad-TRAM, are assumed to represent the best knowledge about the future development (Sauer *et al.* 2014). A cell-specific ID enables to identify cell affiliations that allow for matching and direct comparisons of a nowcasted stage and the related observation. Similar as applied in the spatial verification methods introduced in Section 2.5.3, any spatial deviation between the former and the latter can be interpreted as the inherent uncertainty of the nowcast. To determine the spatial difference, the shape of cells is simplified to a box marking the maximum extent in four directions. In contrast to the overall minimum distance between the objects edges that is determined by Davis *et al.* (2009) in MODE, here, the spatial difference of the boxes edges in each of the four directions is accounted for. The found distance is declared as being a sample of the direction-dependent uncertainty and is merged in a large distribution arising from a number of cell comparisons. The precise methodology is detailed following some general comments on the nowcast uncertainty.

The uncertainty of a nowcast is comprised of two superimposed processes: (1) advection uncertainty and (2) cell development uncertainty. In Rad-TRAM, both processes are extrapolated from the latest radar image. Based on motion vector fields derived from up to six successive images by a pyramidal image matching algorithm, the detected cells are displaced with the found mean vector while finer resolved vectors account for the individual cell development, its shrinkage or growth. Even though one process is totally correct depicted, any inaccuracy in the second process introduces an uncertainty as the cells either are misplaced or have a different shape or size. Traditional scores would impose a double penalty in this case. Similar as other advanced spatial verification methods, the approach proposed here, enables to evaluate whether or not a systematic misplacement or size prediction can be found. If so, a separated consideration of uncertainty would be possible. The related methodology is shortly touched in the following. However, it will be proved necessary to consider the overall uncertainty that emerges from both superimposed processes.

Despite the individual pixel consideration in Rad-TRAM, a cell in the nowcast will never disappear within the 60 minutes lead time. Thus, as actual cells often feature far shorter lifetimes an additional uncertainty is introduced, which is not analysed here.

3.2.1 Cell shape simplification and maximum extent determination

To compare nowcasted and actual cells a rectangular hull box aligned in direction of cell propagation is constructed. The easiest way is to determine the latter in cardinal directions by picking out maximum and minimum of the latitudinal and longitudinal coordinates of a cell as indicated in Figure 3.2(a). Rather suitable for moving objects, whose development and nowcast ability might depend on the movement characteristics, is to apply natural coordinates. As shown in Figure 3.2(b) points most FORWARD and BACKWARD, with respect to the movement direction, are determined by projecting all points on the motion vector plane. A projection on a plane perpendicular to the motion vector enables to identify the outer most points of the object contours LEFT and RIGHT of the movement direction.

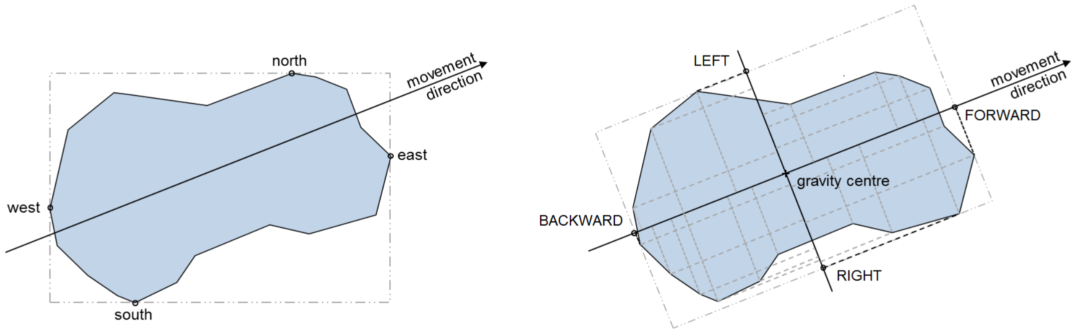

(a) Cardinal directions.

(b) Natural coordinates.

Figure 3.2: Relevant, most outer points (circles) of the polygon forming a wrapping box that describes the maximum extent of a convective cell (a) in cardinal directions and (b) with respect to the cell movement direction.

In the upcoming uncertainty analysis the individual cell motion is accounted for and the extents of the comparative nowcasted and related actual cells are considered with respect to the observed movement direction as visualised in Figure 3.2(b). To each observed cell the availability of former nowcasts is checked. Except of the first detection of a cell, a related nowcast should always be available, which e. g. would be one of the diagonally up-left arranged nowcasts in Figure 2.10. The further comparison is successively performed for all found pairs of actual cell and related nowcasts, e. g. observation at t_{15} and nowcast $t_0 + 15$ (issued at t_0 for 15 minutes lead time), respectively. Thus, all nowcasted cells along the diagonal are compared against the same observed cell if the latter exists. Remember that nowcasts are always provided for the next hour though the cell lifetime often is much shorter. On 15 July 2012 it averages to 25.4 minutes, so for a number of nowcasts, the light grey marked cells in Figure 2.10 (e. g. those > $t_0 + 50$), no comparison is possible as the actual cell dissipated in the meantime (after 50 minutes). These nowcasts are left out in the uncertainty determination. All identified pairs of cells are further processed as presented in SAUER *et al.* (2014) and detailed in the following.

3.2.2 Separated uncertainty of cell displacement and development

According to the uncertainty introducing components, the analysis first focusses on the separated components of cell displacement and cell development. This enables to identify whether Rad-TRAM systematically tends to displace the cells more to one side or faster or slower than observed.

Equivalently as done by DAVIS *et al.* (2009), the displacement error is determined based on the centroids, hereafter referred to as gravity centres. These are given by Rad-TRAM weighted with the radar reflectivity of each pixel of the cell. The dashed-dotted arrow in Figure 3.3(a) pointing from the gravity centre of the observed cell (blue object) to that of the nowcasted cell (grey object) indicates the vector determined for this measure. With respect to the movement direction the displacement error vector for this example is directed forward-left as will be relevant in discussion of Figure 3.5.

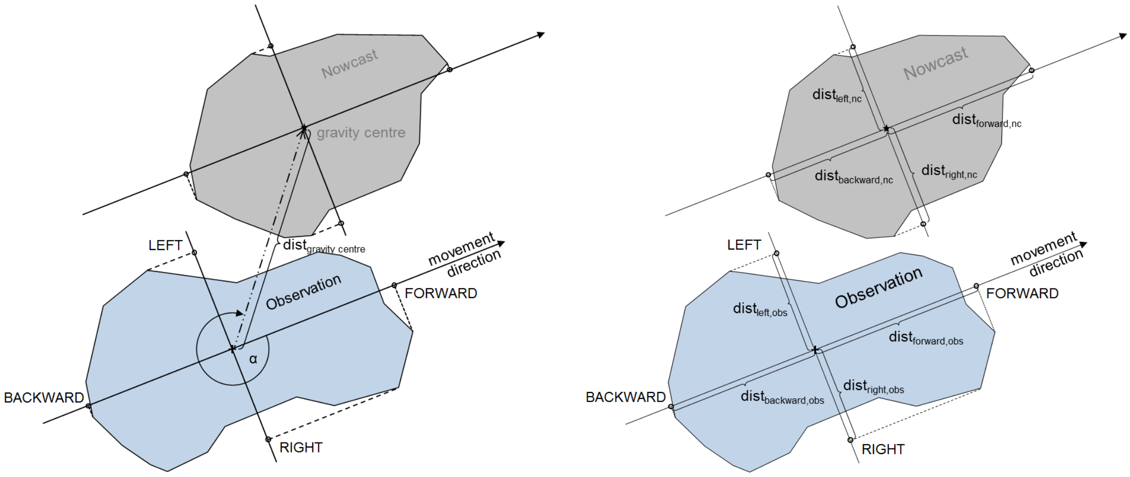

(a) Gravity centre misplacement vector. (b) Maximum extent relative to gravity centre.

Figure 3.3: Methodology of separated uncertainty analysis: (a) gravity centre misplacement indicated by an error vector directed from the gravity centre of the observed cell to that of the nowcasted cell. (b) Determination of the respective maximum extent that is compared between both cells for related directions and lead times.

The deviation of the cell sizes is determined by the direction-dependent distance difference of the maximum extent of both cells in the four directions with respect to their gravity centres as shown in Figure 3.3(b). In other words, one may overlay the nowcasted cell with the observed one so that their gravity centres are the same as visualised in Figure 3.4(a). The difference of the maximum extent on each side (e. g. $\Delta dist_{\text{left}}$) is the measure taken here for the spatial uncertainty in the cell size. Per side, the difference is defined as reality minus nowcast. The ulterior motive is to gain an information on how to modify the nowcast so that it covers the observation. So, if the observed cell has a larger extent on a side than predicted by the nowcast (here in FORWARD, LEFT and BACKWARD direction), the found distance counts positive as it would need to be added to cover the actual cell. Vice versa, a negative distance results from the comparison in direction RIGHT where the nowcasted extent exceeds the actual one.

As will be revealed later on rather no systematic errors will be found for neither the advection uncertainty nor the cell development uncertainty. Thus, an integrated absolute analysis is necessary to identify measures applicable to nowcasted cells in weather avoidance routing.

3.2.3 Absolute deviations between nowcast and observation

The absolute uncertainty of a nowcasted cell accounts for the superimposed uncertainty components related to displacement and growth. Thus, the uncertainty determination introduced in this Section is based on the absolute deviation of both cells in each direction as shown in Figure 3.4(b). As easily recognisable when comparing this absolute distance determination with that presented in Figure 3.4(a), larger deviations and, thus, increased uncertainty measures can be expected for this analysis. This is caused by the nowcast

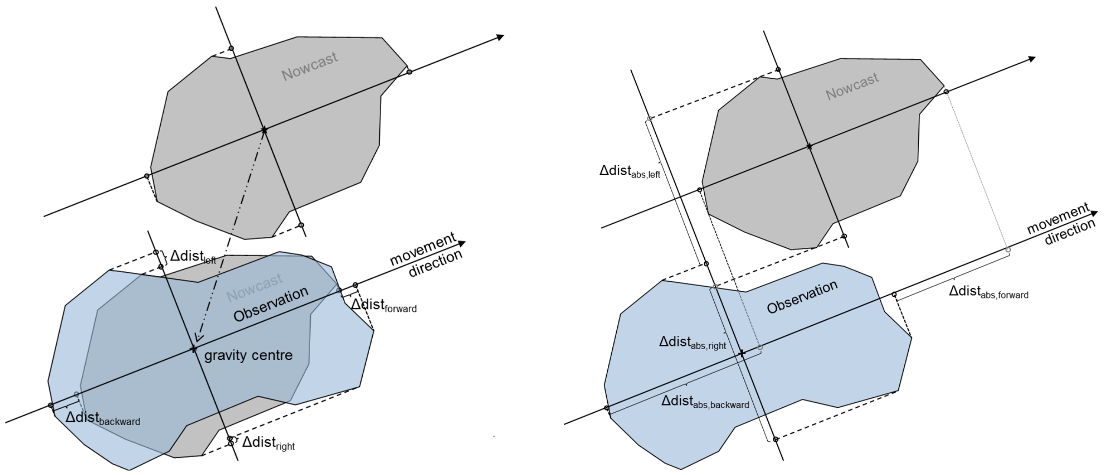

(a) Cell size error illustrated by overlaid cells. (b) Absolute deviations between both cells.

Figure 3.4: (a) Cell size error determined by maximum extent difference of overlaid cells in four directions with respect to the then equal gravity centres. (b) Absolute spatial uncertainty determination between related outer points of nowcasted and observed cells in the same directions.

misplacement which is superimposed to the error in size prediction of cells. It may add an error of up to several tens of kilometres as will be seen in the following discussion of results.

3.3 Results of the nowcast uncertainty analysis

All pairs of nowcasted cell and related observation are analysed. Spatial deviations are determined in four directions according to both methodologies which were previously discussed. For both procedures and per direction twelve distributions will emerge – one for each lead time – in which the respective deviations are merged. From these distributions further evaluations are derived.

3.3.1 Gravity centre misplacement and maximum extent analysis results

The gravity centre misplacement identified in the separated analysis of the two uncertainty introducing processes can be visualised as done in Figure 3.5(a). In the top diagram, all gravity centres (grey points) nowcasted for 5-minutes lead time are shown with respect to gravity centres of observed cells (black point) aligned in the diagrams centre (0,0). The coordinate system is rotated such that the cells movement direction leads upwards. The example from Figure 3.3(a) would give a point in the top-left quadrant, meaning that the cell or at least its gravity centre was nowcasted to far ahead and left of the later observation. The nowcasted gravity centres are rather equally distributed around the actual ones with the mean (red circle) located about 1.5 km right behind of the actual cell centre. This indicates that Rad-TRAM, averaged over all 5-minutes lead time comparisons, tends to displace cells slightly to slow whereas the mean direction matches the real cell displacement. A similar behaviour is recognisable for 30- and 60-minutes lead time distributions of nowcasted gravity centres relative to the observed one shown in the centre and bottom diagramme of Figure 3.5(a). Though, the distribution widens significantly and reaches up to distances of more than 40 km, the mean nowcasted displacement stays slightly behind (2.3 km and 2.6 km, respectively) the movement of actual cells. Therefore, a systematic displacement error of gravity centres in Rad-TRAM can not be derived from this result.

The related relative frequency distributions of maximum extent differences between nowcast and observation are exemplary given for direction RIGHT in the right panel of Figure 3.5(b). The distributions are about symmetric. According to the definition of differences, which are built by reality minus nowcast, positive distances describe situations in which the most right point of the observation is located right of that of the nowcast. Thus, one will need to add a distance to the nowcast to reach the observation. In case the nowcast reaches too far to the right, the nowcast over-predicted the situation and the distance is counted negative. Histogram classes have a width of 2 km corresponding to the spatial resolution of the Rad-TRAM output. The bars are normalised for better comparability, however, the number of counts decreases with increasing nowcast time. Having found 2294 5-minutes lead time nowcasts to compare with a later observation, there were only 1099 and 548 observations found for comparison with nowcasts for 30 and 60 minutes, respectively. This effect, visualised in Figure A.5 in the Appendix, results from the short-life character of convective cells which may have disappeared in the meantime. Additionally, the cumulative distribution of found detours is plotted in grey and the 90th percentile, indicating the value that builds the upper limit of 90 % of all samples of the distribution, is given by the black dashed line in Figure 3.5(b).

The distances found for different lead times result in a single peak distribution each of which is more or less symmetric. Especially the distribution for 5-minutes lead time nowcasts exhibits a positive excess kurtosis characterising the distribution as being leptokurtic, meaning that it has an even steeper peak than a normal Gaussian distribution. Goodness-of-fit tests like that of JARQUE and BERA (1987), however, reject the null hypothesis that the distributions match the skewness and kurtosis of a normal distribution. What is hinted here is a decrease of the kurtosis leading to a broader distribution with increasing lead time of the nowcasts. The 90th percentile, which will be of interest in the uncertainty consideration in weather avoidance routing, shifts from 1.91 km to 5.62 km and 7.55 km in top-down direction of the given distributions.

The distributions for LEFT, FORWARD and BACKWARD directions exhibit a similar symmetric shape and range (not shown). Thus, no characteristic tendency of cell misplacement or cell size prediction is identified in the Rad-TRAM data set. Therefore, a deduction of applicable uncertainty measures for the separated processes is hard and the further focus is set to the absolute uncertainty analysis.

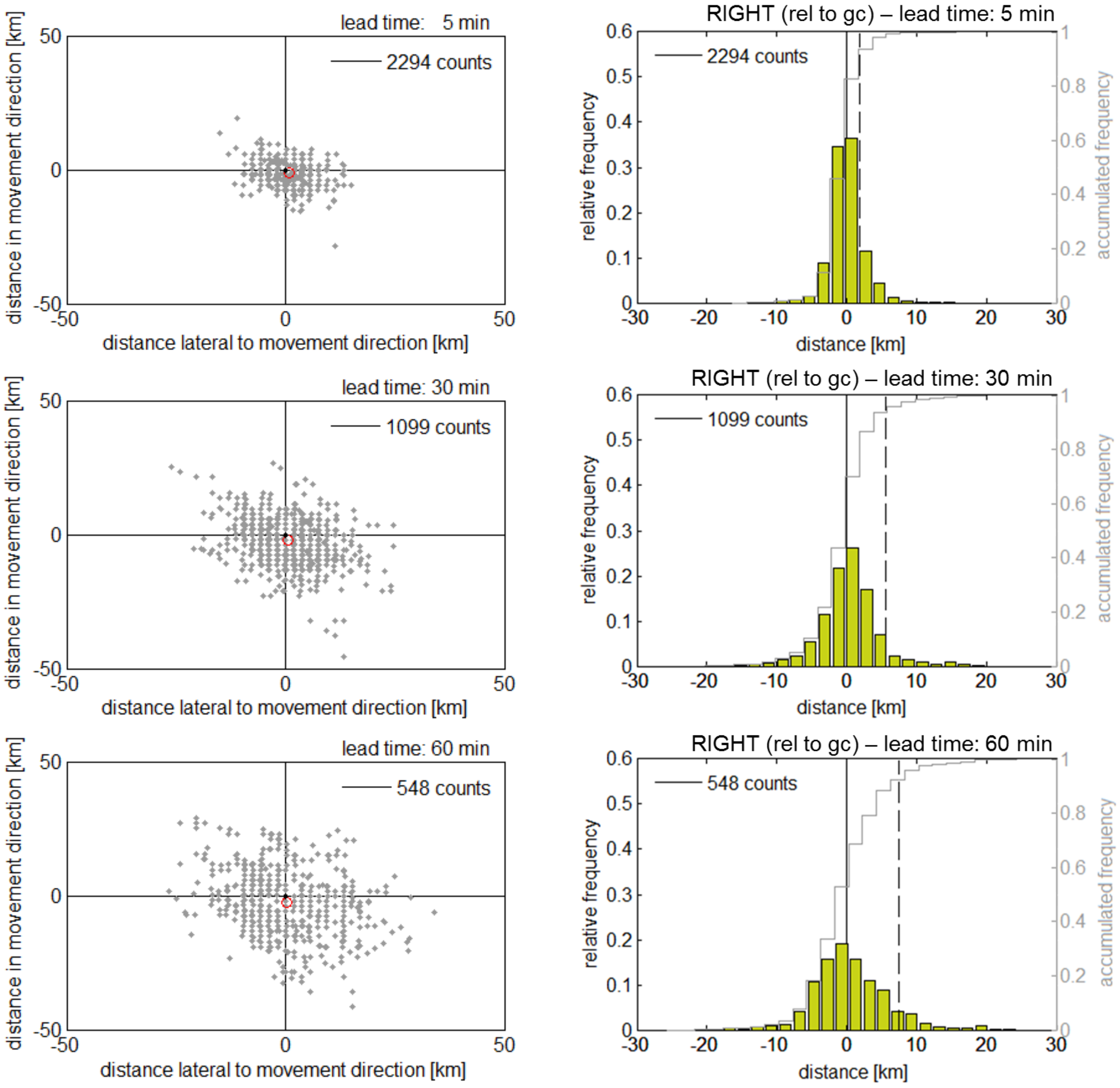

(a) Gravity centre misplacements for 5-, 30- and 60-minutes lead time.

(b) Frequency distribution of spatial deviations for 5-, 30- and 60-minutes lead time in direction RIGHT.

Figure 3.5: Nowcasted gravity centre locations (grey points) relative to the actual ones (black point) in the diagrammes centre are given in the left panel (a) for lead times of 5, 30 and 60 minutes obtained from 2294, 1099 and 548 cell comparisons. The coordinate system is oriented so that the actual cells movement is in direction of the positive ordinate. The respective mean of the distribution is indicted by the red circle. In the right panel (b) related maximum extent differences of the overlaid nowcasted and actual cells for direction RIGHT are shown. The cumulated distribution is given by the grey line, the 90th percentile by the black dashed line.

3.3.2 Results of the absolute uncertainty analysis

Frequency distributions found in the analysis of absolute deviations between nowcast and observation for lead times of 5, 30 and 60 minutes and directions LEFT and RIGHT are given in Figure 3.6. The left panel (a) shows the results for direction LEFT in blue bars. Whereas the distribution for 5 minutes looks pretty much like that of the analysis of maximum extent comparison discussed before (single peak, symmetric), the distribution flattens and broadens much stronger in the absolute analysis shown here. The single peak character dissipates with increasing lead time and is disappeared in the distribution for lead times of 60 minutes. Neither this nor all following distributions match a Gaussian distribution as proofed by goodness-of-fit tests. The 90$^{\text{th}}$ percentile shifts from 1.98 km to 11.14 km and further to 17.14 km for the given lead times.

In contrast to the spatial absolute deviation distributions for direction LEFT, those for RIGHT exhibit a different shape (see right panel (b) of Fig. 3.6). A symmetry is not shown. Instead, there are only few negative counts. This implies that in almost all cases of 15 July 2012 the most right point of the observed cell was further right than nowcasted. As discussed in Section 2.3.2, observations report on a common development of new cells at the leading right edge of existing cells in the northern hemisphere. A new cell merging the older one leads to a seemingly displacement of the cell to the right of the winds (BROWNING 1986). It might be that this effect of new cell formation and the resulting deflection to the right are not fully covered by Rad-TRAM as it only accounts for already existing cells. This could be a reason for the characteristic results in direction RIGHT in some synoptic weather situations. On other thunderstorm days, which were sampled, this feature of the nowcast was not observed. However, a systematic analysis has not yet been performed and is beyond the scope of this work.

The 90$^{\text{th}}$ percentile level is about 2 km larger than for direction LEFT and shifts from 3.79 km to 11.68 km and further to 18.24 km for the given lead times.

Box-and-whisker plots summarising the main characteristics of the found frequency distributions for all four directions and their development with lead time are given in Figure A.6. As recognisable there, distributions for FORWARD and BACKWARD direction feature about the same symmetric characteristics like such found for deviations LEFT of the movement direction.

Uncertainty development

The development of the nowcast uncertainty, which was already indicated by the 90$^{\text{th}}$ percentiles of the distributions that shift to larger values with increasing lead time, is recognisable when plotting the latter measure above the lead time as done in Figure 3.7.

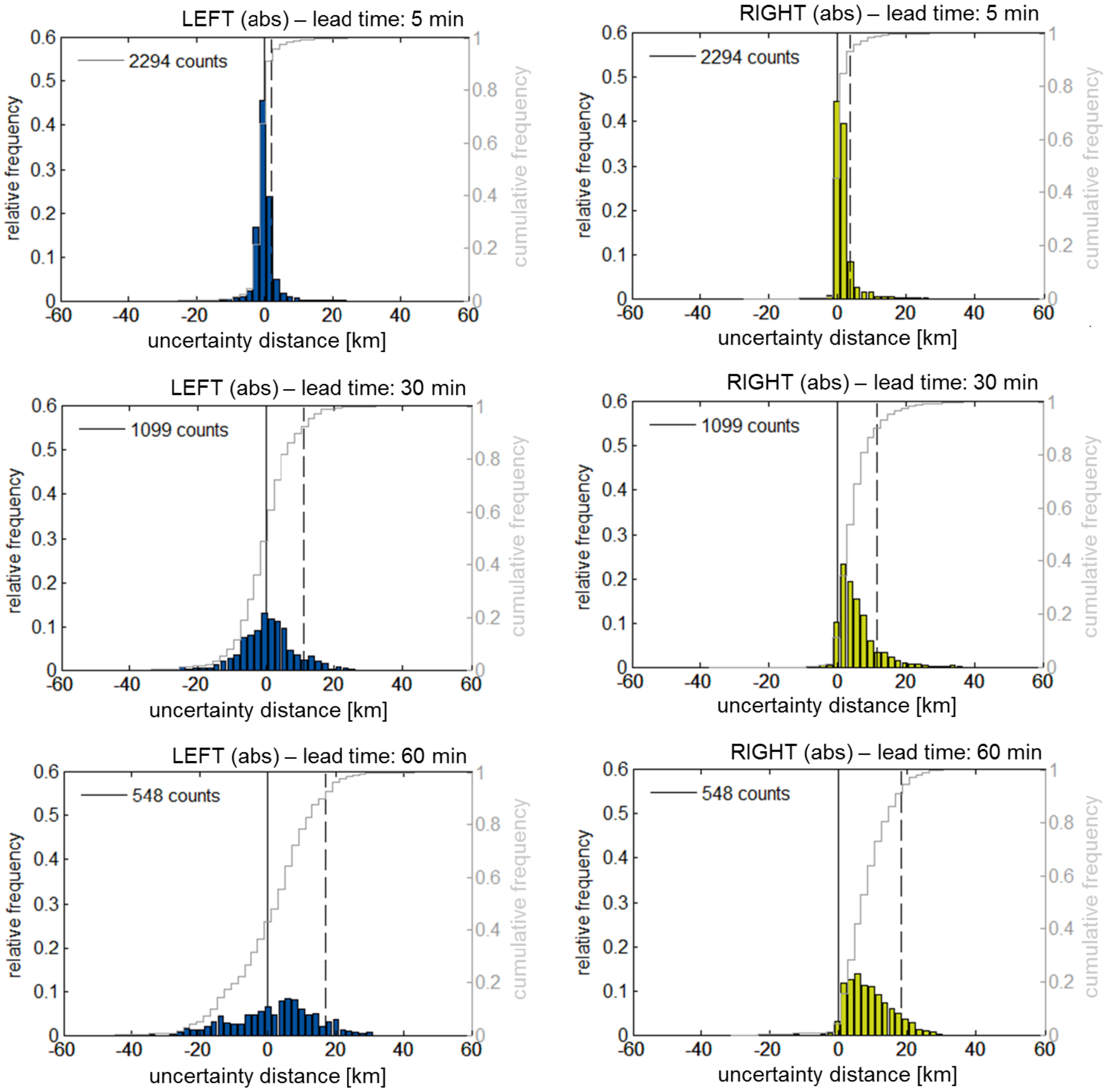

(a) Left side deviations for 5-, 30- and 60-minutes lead time.

(b) Right side deviations for 5-, 30- and 60-minutes lead time.

Figure 3.6: Frequency distributions of absolute spatial deviations in direction (a) LEFT and (b) RIGHT for lead times of 5, 30 and 60 minutes. The accumulated distribution (grey line, right ordinate) helps to identify the 90^{th} percentile (dashed line) that shifts to larger values of the widening distributions with increasing lead time.

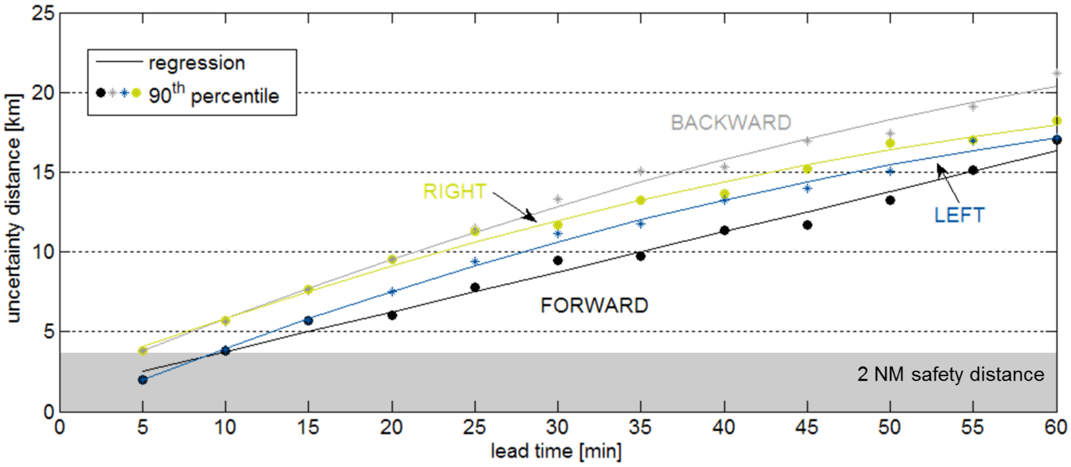

Figure 3.7: 90th percentiles of all four directions (circles for direction FORWARD and RIGHT, stars for LEFT and BACKWARD) as a function of lead time. Polynomial regressions are shown in lines. Their respective regression coefficients are given in the text. The grey bar indicates a 2 NM distance for comparative reasons as it will become relevant in the study presented in Chapters 5 and 6.

For 5-minutes lead time nowcasts the 90th percentiles, arising from the previously discussed frequency distributions, are equal to 1.97 km for FORWARD (black circles) and LEFT (blue stars), and 3.78 km for BACKWARD (grey stars) and RIGHT (green circles) direction. With increasing lead time the uncertainty defining measure rises for all directions. However, the rate at which the uncertainty increases varies. While the uncertainty is maximum for the backward direction at all times, it is smallest throughout all lead times. It reaches up to 17.01 km for 60-minutes lead time nowcasts for which the uncertainty in the remaining directions is spread up to 21.17 km.

Thus, uncertainty is direction- and lead time-dependent. Information on the time-dependent (t in minutes) development rate of the direction-related uncertainty u in kilometres is obtained by polynomial regression in a least squares sense resulting in the following polynomials:

$$\begin{aligned}
u_{90,\mathrm{LEFT}}(t) &= -0.0023 \cdot t^2 + 0.4275 \cdot t - 0.0921 \\
u_{90,\mathrm{RIGHT}}(t) &= -0.0023 \cdot t^2 + 0.3908 \cdot t + 2.1487 \\
u_{90,\mathrm{FORWARD}}(t) &= 0.0001 \cdot t^2 + 0.2450 \cdot t + 1.3111 \\
u_{90,\mathrm{BACKWARD}}(t) &= -0.0020 \cdot t^2 + 0.4336 \cdot t + 1.6721
\end{aligned}$$

The developments of further measures like mean, median and the 10th percentile, that all help to describe a frequency distribution, are shown in Figure A.6 in the Appendix.

Variation of nowcasted cell contours

The variation of nowcasted cell contours in all directions for a certain lead time are visualised as follows in Figure 3.8. In there, the 80 %-range defined by 10th (outer line) and 90th (inner line) percentiles of the found frequency distributions of the nowcast error are indicated by grey bars forming a frame behind the artificial actual cell contour given in bold black. Its edge length is set to 100 km in order to also visualise the negative deviations in a clear way. Any nowcasted contour in the grey area within the red box would represent an underestimation of the related observation in the nowcast. The inner white box gives a cell to which the previously found direction-dependent 90th percentile values have to be added to match the actual cell. In each direction still 10 % of nowcast contours will be within the white box. However, as the mean diameter of the Rad-TRAM data set cells in and lateral to the movement direction averages to 15.7 km, with occasional observations of over 40 km (maximum: 81.3 km) the nowcast might probably not be simultaneously smaller in all directions. Instead, both cells can be completely separated with a nowcasted outer most left point which is even right of the actual rightmost point. An off-centre box contour would result from such a case.

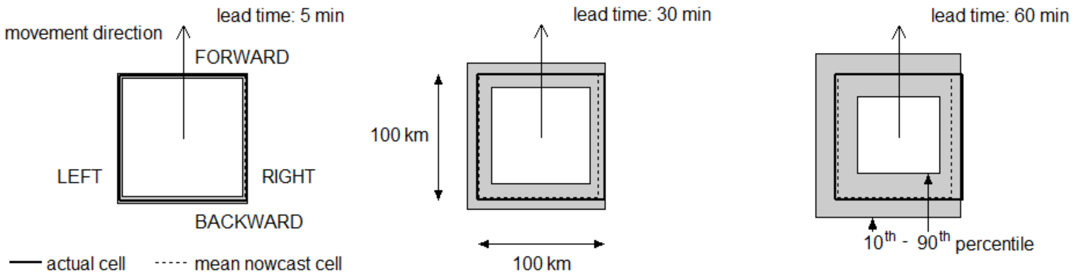

Figure 3.8: Grey bars behind the bold black box, which indicates the actual cell contour set to a fixed edge length of 100 km, show the 80 % variation range (10th - 90th percentile for outer and inner box, respectively) of nowcasted cell edges in the respective direction. The mean nowcasted contour box is given by the black dashed line. Plots are given for lead times of 5 (left), 30 (centre) and 60 (right) minutes.

Again, clearly recognisable is the increasing variation – the spread – of nowcasted contours with lead time. Not only the 90th percentile shifts to larger values (here: inner margin), but the negative values of the 10th percentile shift to smaller ones, what increases the absolute value and widens the frame additionally. The variation differs with the direction and especially the RIGHT-side characteristics identified in Figure 3.6 stick out for the 30- and 60-minutes lead time plots (centre and right) as well as all other not shown lead times where the variation is concentrated within the bold black box. The respective mean nowcast contour defined by the means of the distributions is given as a black dashed line.

Correlation analyses of deviations on opposing sides

Furthermore, a correlation analysis on the spatial deviation found for opposite sides is processed and results are provided in Figure 3.9. It enables to identify whether the deviations are positive or negative on both sides, meaning that the cell was nowcasted either too small or too large in both directions, or if one deviation is positive while the other is negative what describes a shift of the cells against each other.

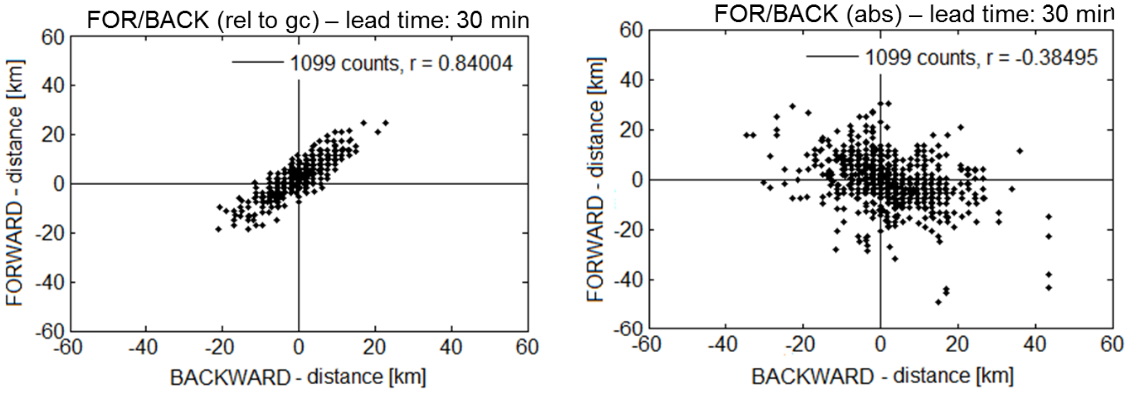

(a) Maximum extent difference analysis.

(b) Absolute deviation analysis.

Figure 3.9: Scatter plots indicating the correlation of spatial deviations between nowcasted and actual cells for opposing directions and 30-minutes lead time. Deviations of the leading edges (FORWARD direction) of the cell are given on the ordinate, such found in BACKWARD direction on the abscissa. The top-right quadrant gives such cases in which both deviations were positive describing a nowcast that was smaller than the actual cell in both directions (vice versa for bottom-left quadrant). In contrast, the bottom-right quadrant indicates a positive BACKWARD deviation (actual cell exceeds the nowcast) and a negative one in FORWARD direction, what results from a too fast cell displacement. (a) Deviations in opposing sides of the maximum extent analysis relative to the gravity centre (separated analysis) show a strong positive and linear correlation. (b) Deviations found in the absolute distance analysis show rather no correlation.

Size deviations in the separated analysis were determined by differences of maximum extents on each side of aligned nowcasted and observed objects with their gravity centres. Correlating the found differences for opposite-direction pairs results in a coefficient r ranging between 0.5 and 0.9 (see Fig. 3.9(a)). This implies that Rad-TRAM tends to equally under- or overestimate the cell size in opposite directions with respect to the cell movement. When the cell misplacement is superimposed, the former correlation disappears and rather all combinations are found (see Fig. 3.9(b)). With lead time a widening of the respective point cloud can be recognised (not shown). Equally analysed but not shown here are correlations of LEFT and RIGHT side deviations. Due to the discussed RIGHT-side characteristic, the resulting point clouds exhibit a shift to only positive distances for RIGHT while the nowcasted LEFT side extent is smaller or larger than observed. Thus, points are mainly found in two neighbouring quadrants but again without any specific correlation.

The extent of each nowcasted cell and its location relative to the related observed one is

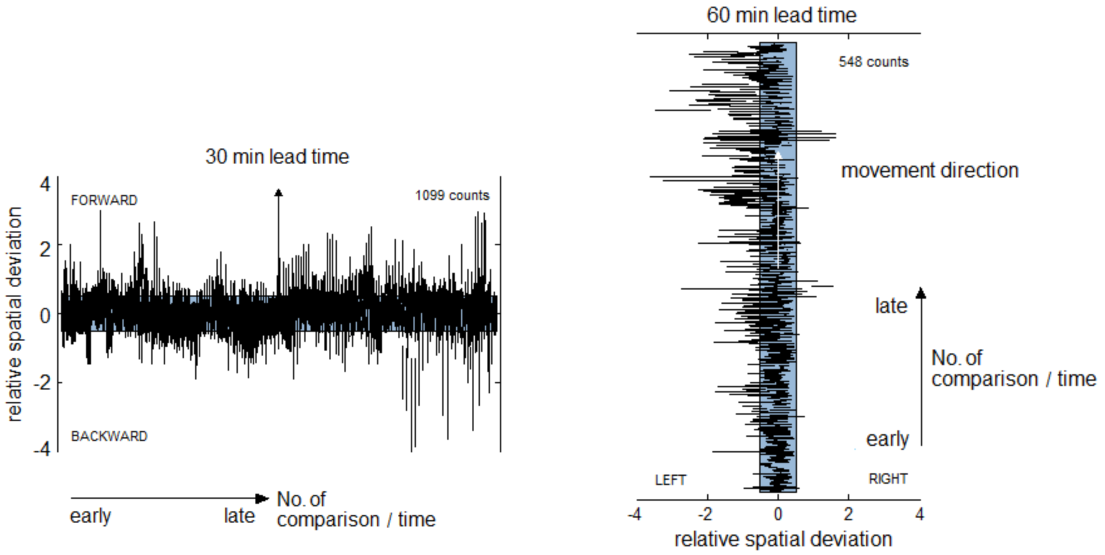

(a) Parallel to movement direction. (b) Lateral to movement direction.

Figure 3.10: Nowcasted cell extents and locations (black lines) relative to a standardised cell (height/width of blue bar = 1) (a) in and against and (b) lateral to the movement direction for lead times of 30 and 60 minutes, respectively. Lines longer than 1 represent nowcasts that were larger, than the later observation and vice versa. A black line that is totally apart the blue bar indicates completely separated cells that do not overlap.

given in Figure 3.10. In Figure 3.10(a) extent and position of 30-minutes lead time nowcasts are given parallel to the movement direction (FORWARD+BACKWARD), whereas in Figure 3.10(b) nowcasted cell extents and locations for 60-minutes lead time are given lateral to the movement direction (LEFT+RIGHT). In both Figures the actual cell is standardised to width 1 (blue box) in the respective direction. For each nowcasted cell a black line indicates its characteristics relative to the observation. As deduced from previous analyses presented in former Sections, all types of deviations (smaller, larger, shifted to either of the sides) are recognisable in Figure 3.10(a). In some cases the nowcasted cell is completely shifted against the comparative one visualised by a black line that is located on one or the other side of the blue bar. In 3.10(b) again the overestimation of the LEFT-side extent in the nowcast becomes obvious. The nowcast exceeds the blue bar only occasionally on the right side. This lateral uncertainty will have the main influence in the routing simulations presented in Chapters 5 and 6. Thus, a full panel for the lateral uncertainty including all lead times, is exemplary shown in Figure A.7 in the Appendix.

Nevertheless, the correlation analysis for absolute deviations shows no distinct results. The same holds for the gravity centre misplacement from which, as discussed first in this presentation of results, no characteristic error can be derived. Instead, the absolute spatial deviations and their respective measures, e. g. the 90th percentile, are most appropriate to be further accounted for in adverse weather avoidance modelling.

3.4 Critical comments on the uncertainty analysis

The presented uncertainty analysis poses a suggestion what methodology to apply in order to deduct appropriate measures. Though the data set was limited, it is assumed as being representative for the Rad-TRAM product and the obtained results are further applied to cells of the same set. The found uncertainty measures build a hypothesis that needs to be confirmed by a systematic analysis which should be based on a much larger data set. It might be interesting to see whether or not characteristics in the uncertainty can be found for differing synoptic situations or certain geographical regions. As an example, frontal thunderstorms might be easier to displace than individual air-mass storms as the former rather travel with the mesoscale structure of which the characteristics are more or less known and predictable.

Different synoptic and structural situations will also influence the lifetime of cells. This issue still need some investigation to identify a methodology how to account either for new emerging cells that are not nowcasted before as well as dissipating cells. For each of the latter a nowcast of up to 60 minutes was released just 5 minutes ago. Such cases, rated as false alarms in traditional scores, were left out of consideration in the performed analysis as no matching observation is available.

Having then created several pools of uncertainty measures, each relevant for one certain synoptic condition, such as frontal thunderstorms with fast motion of the front, these measures are assumed to define the uncertainty of the nowcast system for the respective situations which can be applied to future nowcasts. According to the then current synoptic situation in which thunderstorm nowcasts are released, the pool allows to pick out the appropriate related measures and apply them to the nowcasted cells as suggested in the following. Which particular measure, whether for instance the 90th or 95th percentile, is applied resides in the user.

3.5 Integration of uncertainty in weather avoidance routing

Having determined the specific uncertainty of the nowcast product it should be applied in a beneficial manner. Regarding future ATM strategies, including the principle of 4D trajectories, predictability and robust planning become more and more important. In route planning and weather avoidance route modelling, airspaces affected by hazards such as military zones in action, volcanic ash areas or adverse weather regions of icing or thunderstorm occurrence, are often treated as so called "no-go" zones. For that two- or three-dimensional polygons are considered around which a safe trajectory is calculated as will be detailed in Chapter 4. Among observational data obtained by radar and satellite from which such polygons are extracted, nowcast systems like Rad-TRAM are conceivable data sources that directly provide cell contours. Either observational or nowcasted cells can be used then. The previously identified spatial uncertainty allows for defining regions around such nowcast cells in which thunderstorms occur with certain probability. Based on a deterministic nowcast the product-specific spatial uncertainty enables to

derive probabilistic statements that facilitate decision making.
In contrast to ensemble prediction, where the given probability refers to the occurrence of the meteorological phenomenon, here it is rather a methodology common in tropical cyclone forecasting. Instead of a precise location and size, a widening cone, covering the forecast for several days, is issued and states the possible centre track of the storm while incorporating the uncertainty. The latter is obtained by the 67th percentile of spatial track errors identified in the past five years (THE COMET PROGRAM 2015). The characterised cone does not show the size of the storm but the possible path of its centre. The resulting area in the application presented here, rather indicates an area anywhere in which the actual thunderstorm cell will be located with the respective certainty. To create this area the nowcasted cell contour is enlarged by the direction- and lead time-dependent uncertainty measure. Accounting for an avoidance of this uncertainty area still reveal a risk of e. g. 10 % to encounter the actual cell anywhere apart.

The methodology applied to form the so called uncertainty margin around nowcast cells is visualised in Figure 3.11 and consists of the following three steps:

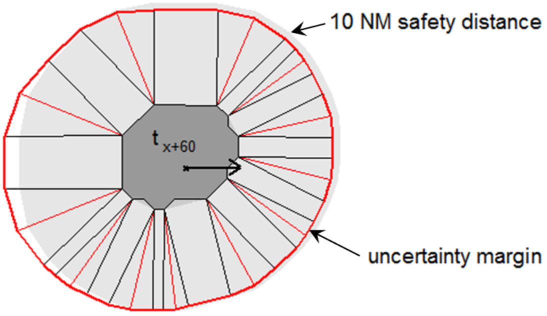

Figure 3.11: 90th percentile uncertainty margin (bold red contour) creation for a 60-minutes lead time nowcast cell (dark grey shaded polygon). Normals (black lines) to each edge of the related convex polygon are constructed at each respective node. The node itself is displaced along the angle bisector (red thin lines). The distance to which the nodes of the uncertainty polygon are set on these found lines is defined by each lines orientation with respect to the cell movement direction as well as to the respective uncertainty measure for that direction which might be linearly interpolated. For comparative reasons a constant 10 NM safety margin around the cell is indicated in light grey.

1. The deterministic (nowcast) cell (dark grey shaded polygon) is convexly wrapped (medium grey patches filling the concave polygon sections).

2. Each edge of the convex polygon is outwardly parallel displaced by a direction- and lead time-dependent distance. When aiming to form a polygon in which the later thunderstorm is located with 90 % certainty, the 90th percentile value for each direction and the respective lead time (see Fig. 3.7) is accounted for. The normal (black lines) on each of the polygons edges, its angle relative to the movement vector, defines the distance by which the convex edge of the cell is displaced. Distances

for angles between the four main directions are linear interpolated. A new point in the respective distance is created on each normal.

3. The convex vertex of each polygon is displaced by the respective distance along the angle bisector (red thin lines). The resulting uncertainty polygon (bold red contour) consists of a sequence of new points, three per each of the nowcast vertices.

Due to the direction-dependent distances the resulting uncertainty polygon might again feature concave sections which should be eliminated before integration in routing tools like DIVMET, which will be detailed in Chapter 4. For comparative reasons a constant safety margin of 10 NM which represents avoidance distance for thunderstorms recommended in international regulations (see e. g. NATS 2010) is indicated in light grey and is in about the same magnitude.

The uncertainty increases with lead time. Thus, depending on the lead time the uncertainty margins significantly enlarge the polygon area that should be avoided. Some lead time samples (grey shaded polygons) of a nowcast set together with the observation (blue shaded polygon) on which the nowcast is based are given in Figure 3.12. While there is no significant growth of the nowcasted cell (between 69 km^2 and 87 km^2), the respective 90th percentile uncertainty polygons do increase considerably with lead time which rises to the right. The cells are separately presented, their actual gravity centre location is indicated by the lines below that lead to the coordinate system on the left.

The enlargement of the accounted area is given by the ratio of uncertainty polygon area to that of the nowcasted cell. The nowcast area is enlarged by one and a half times for 5-minutes lead time. In contrast to that the resulting uncertainty polygon for 60-minutes lead time has more than twentyfold the nowcasted cell area. Each related observation of the respective cell is given by a bold black contour which lags behind the eastward moving cell (indicated by the arrow) at lead times larger than 30 minutes. However, except of the 10-minutes lead time situation, where another cell probably merged into the considered one, all observed cells are fully located within the uncertainty polygon. They would have been safely avoided when having planned routes based on these objects.

The ranges of obtained cell area enlargement due to the creation of uncertainty polygons around all nowcasted cells are shown in box-and-whisker plots provided in Figure A.8 in the Appendix. The interquartile range, meaning the 50 % of data between 25th and 75th percentile, of this area ratio is narrow at around a doubling of the polygon size for 5-minutes lead time and spreads out afterwards. For 60-minutes nowcasts the box reaches up to a 20-fold enlargement. The upper whisker (91th percentile) almost reach a ratio of 25.

In multistorm environments such an enlargement of each cell may lead to large structures that merge and, thus, prevent any get through but force re-routings. The early consideration of possibly dissipating hazardous areas may cause inefficient and unnecessary detours. Thus, strategic planning of such manoeuvres, which are made worse due to uncertainty, are probably not the common strategy for short-living phenomena like

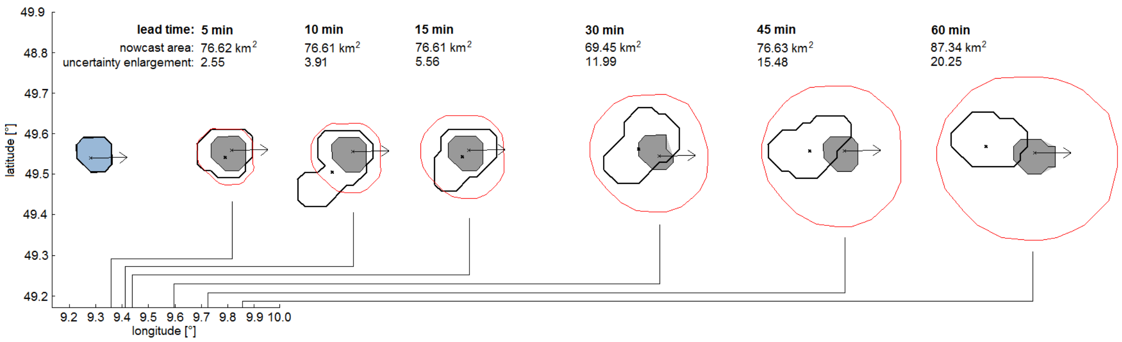

Figure 3.12: 90th percentile uncertainty margins (red) around 5, 10, 15, 30, 45 and 60 minutes lead time nowcasts (grey shaded polygons) released at 7:55 UTC. The nowcasts are based on the second observation of the cell (blue shaded polygon). The longitudinal location of their gravity centre is indicated by the bottom lines leading to the coordinate system on the left. Related later observed cells are given by bold black contours. The nowcasted area in km^2 as well as the ratio of uncertainty polygon and nowcasted area are given for each presented lead time.

thunderstorms. The initiation of any deviation may rather be shifted to the tactical level in order to adapt the actual or more certain situation and adjust the route later on. Studies on the trade-off between robust route planning and efficient routing will be detailed in Chapter 5. Before that, an introduction into weather avoidance routing and the applied model DIVMET is given in the following Chapter.

4 The adverse weather diversion model DIVMET

In 2009 HAUF and SAKIEW started developing the adverse weather diversion model DIVMET, which stands for *divert meteorology*, at the Leibniz Universität Hannover. DIVMET is a fast time simulation model that generates a safe and short deviation route for single aircraft laterally around each conflicting thunderstorm cell and through a dynamic multi-storm environment (HAUF *et al.* 2013).

It is one among a number of weather avoidance models currently under development that enable path-finding in adverse weather situations. These models support decision making by involved parties in aviation and, thus, reduce workload in adverse weather situations (MCNALLY *et al.* 2012). The pioneer of avoidance models is probably the Dynamic Weather Routes (DWR) ground-based trajectory automation system developed at NASA Ames Research Center. The system is operational in use for testing purposes at American Airlines for two years now and aims to optimise weather avoidance routes of active flights which were defined prior to departure (MCNALLY *et al.* 2015). Actual and nowcasted thunderstorm information is used in form of contours extracted from NEXRAD radar devices and processed by the Corridor Integrated Weather System (CWIS) convective weather forecast model (KLINGLE-WILSON and EVANS 2005). These contours are then processed in the Convective Weather Avoidance Model (CWAM) that generates so called Weather Avoidance Fields (WAF) giving avoidance polygons around convective cells that are circumnavigated by pilots with certain probability. These probabilities were previously obtained by statistical analyses of the avoidance behaviour of pilots in convective situations (MATTHEWS and DELAURA 2010). DWR takes these WAFS and integrates them in the air traffic simulation Center/TRACON Automation System (CTAS). Operated by airline dispatchers, CTAS finds optimised conflict-free, laterally displaced routes that get along with two auxiliary named waypoints maximum while considering weather up to two hours ahead, traffic conflicts and FAA routing restrictions. Airspace congestion downstream the conflict can be analysed with the Future ATM Concepts Evaluation Tool (FACET, BILIMORIA *et al.* 2001, SRIDHAR *et al.* 2005) and the finally agreed auxiliary waypoints are communicated to the pilot who further coordinates the manoeuvre with the responsible ATCO. The approach applied in DWR to find a safe route emerges from geometrical considerations and determination of tangents from certain points on the planned trajectory to the avoidance polygon. Tangents intersections nearby named waypoint identify those to use (MCNALLY *et al.* 2012).

Other weather avoidance models are still far from this sophistication. The applied approaches vary a lot depending on the individual model objective. Motivated by a natural solution for the path-planning problem, the Light Propagation Algorithm (LPA), developed by Dougui *et al.* (2011) is based on wavefront propagation through a medium with a varying index of refraction. The latter also allows for introducing speed constraints and minimum distances to hazardous areas. Following Fermat's Principle (Feynman *et al.* 2013), the simulated path of light transition represents a time-optimised trajectory. Another approach to find the shortest path is provided by Dijkstra's algorithm that calculates all possible connections between two points in a discretised space, a grid, and searches for the shortest path (Rippel *et al.* 2005). Among the named procedures further solutions for the typical path-finding problem are applied in the broad field of robotics. An overview of which is for instance given in (Correll 2014).

In contrast to these specific avoidance algorithms, advanced air traffic simulation models such as AirTOp account for detailed flight performances and airspace regulations. If at all, they only allow for circumnavigation of large structures introduced by blocked airspace as exemplary applied by Luchkova *et al.* (2015) by means of a volcanic ash event.

Regarding DIVMET, the original purpose was to represent current re-routing behaviour of pilots in thunderstorm situations in which decision making is mostly based on the on-board radar information. The benefit resulting from increased weather information is one objective that can be investigated with DIVMET as well as it allows for consideration of different stages of weather information. Similar as in DWR, path-finding in DIVMET is based on geometrical considerations but at the time being is limited to single-hazard, namely thunderstorm avoidance.

Having started from scratch six years ago, now several thousand lines of Matlab code account for different simulation modes. Varying weather information stages can be included and a set of routing options allows for different strategies to simulate what will be of relevance in Chapter 5. The possibility to couple DIVMET to an air traffic simulation model enables to account for multi-aircraft situations while considering aircraft performances (Hauf *et al.* 2013). A detailed overview with key features of DIVMET is presented in the following.

4.1 Representation of adverse weather

Adverse weather is represented in DIVMET by two-dimensional no-go zones. These are introduced by impermeable closed polygonal paths, also referred to as weather objects – a phrase first defined in the Flysafe project where these objects were sent to and displayed in the cockpit (Mirza *et al.* 2008).

So far DIVMET is restricted to thunderstorm circumnavigation, however it is not limited to this type of adverse weather. As described in Section 2.4 thunderstorm monitoring is mainly enabled by radar and satellite observations. Thusand as applied in Rad-TRAM, these data sources allow for polygon extraction according to certain thresholds. Again radar data reflectivities equal to or exceeding 37 dBZ are considered as they are often associated with convective airspaces avoided by pilots (Forster and Tafferner 2012). Either observational or nowcasted radar data or other polygonal information, e. g. from Rad-TRAM or Cb-TRAM, can be used in DIVMET.

Polygonal paths comprising these areas of intense reflectivity are extracted and taken as input for DIVMET. However, the cell extent provided by radar data is rather valid for lower altitudes (see Section 2.4). Nevertheless, DIVMET considers each weather object to represent a vertical atmospheric column blocked by convection, reaching from surface level to high altitudes. These columns are dynamic in the simulation according to data availability which usually has update rates ranging between 5 and 15 minutes.

When considering thunderstorms, their representation by polygonal columns is appropriate as they force lateral deviation manoeuvres to be defined by the model. DIVMET is in principal applicable to other adverse weather phenomena like icing areas and volcanic ash which can be similarly considered as no-go zones. Although, compared to the column-shaped appearance of thunderstorms, these two types of adverse weather occur in distinct layers. Instead of horizontal deviations, vertical manoeuvres, namely flight level changes, are likely to be the more efficient solution which is not yet implemented in DIVMET.

The principles of path finding based on lateral deviation manoeuvres in DIVMET are detailed in the following Section.

4.2 Path finding in DIVMET

In DIVMET, trajectory and weather data serve as input, as shown in the first steps of the flow chart presented in Figure 4.1. All weather representing polygons are read in. According to time and the respective aircraft position the latest weather information is picked from the data pool. Depending on the applied weather information stage, the so called field of view (details follow in Section 4.3.1), either the overall situation or limited parts of it are assumed to be known resulting in a (reduced) set of cells further referred to as weather objects. For further consideration in the model the pure weather objects are convexly wrapped before being enlarged by certain avoidance distances recommended by international regulations. These larger convex polygons define potential risk areas which are then checked for conflicts with the planned trajectory. Conflicting risk areas are marked. These, together with the remaining risk areas and certain points (current position *A* and a target point *B* on the planned trajectory), are then passed to the MET2ROUTE algorithm (grey structure in Figure 4.1) which accounts for a static deviation route calculation.

In MET2ROUTE a complete deviation route based on geometrical considerations of the static set of conflicting risk areas is generated geographically based on the reference ellipsoid of World Geodetic System 1984 (WGS84, Maularie (2000)). The first decision to be made is whether to initiate the diversion to the left or right of a cell. Similar to decision making by pilots, the spatial extent of all conflicting risk areas left and right of the route

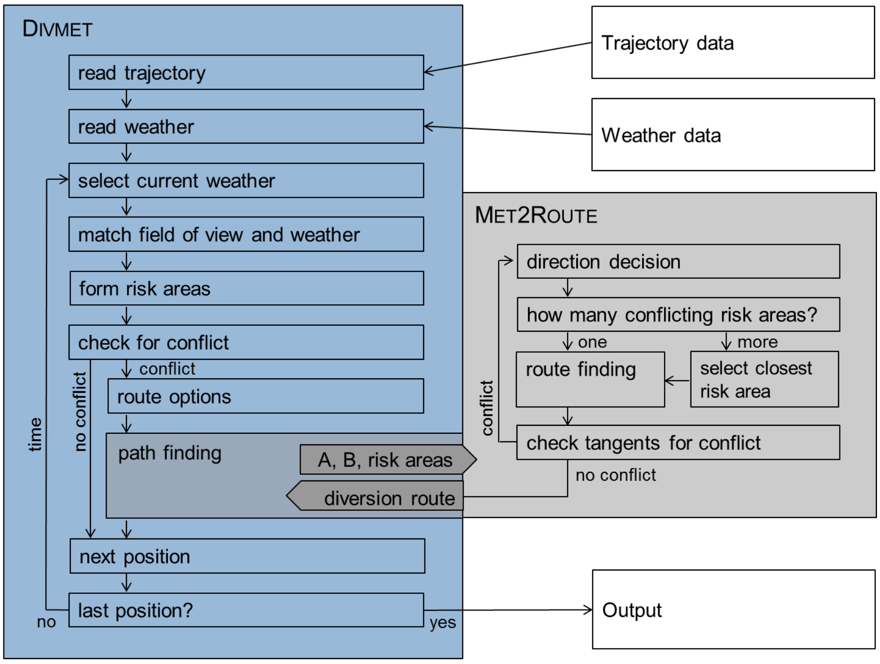

Figure 4.1: Flow chart with separated structures for the simulation model DIVMET (blue), the static path-finding algorithm MET2ROUTE (grey) with exchange parameters and external in- and output data (white).

is the decisive factor. If the extent to the left is larger, as shown in Figure 4.2(a), the first deviation manoeuvre will be initiated to the right as it is assumed that the smaller extent is likely to result in shorter deviation routes however this is not necessarily the case.

The path-finding is then successively processed object-based for single risk areas along the route. In case of several conflicting risk areas the second step is to identify the closest one (*RA1*) to the current position A of the aircraft. In the situation given in Figure 4.2(b) only one risk area is in conflict with the planned trajectory. Tangents T_1 and T_2 from A and B to the formerly defined side of the risk area and tangent points EP and XP on the latter, respectively, are determined. These tangents may solve all conflicts but may also cause new ones. Thus, a procedure is run through to check both tangent sections $\overline{A\,EP}$ and $\overline{XP\,B}$ for conflicts with any of the risk areas whether formerly conflicting or not and eventually solve them. If there is no conflict, the deviation route is pooled by three parts: Tangent T_1 section $\overline{A\,EP}$, the convex polygonal segment from EP to XP of the risk area and section $\overline{XP\,B}$ on tangent T_2. Otherwise, if there is a conflict on one tangent section, the newly conflicting risk areas are marked. When assuming to have identified a conflict on T_1 as shown on the right in Figure 4.2(b), again the closest new risk area RA_2 is found and the direction decision is repeated, now based on the spatial extents of this single risk area left and right of the tangent section $\overline{A\,EP}$. Point A remains for further calculation but B is temporary shifted to risk area RA_1. While accounting for the new direction decision for RA_2, two tangents are determined from there to point A as well as to risk area RA_1 which temporary serves as target B' however without any distinct point. Two new tangents are found which together with the polygon section of RA_2 replace T_1. Now the procedure

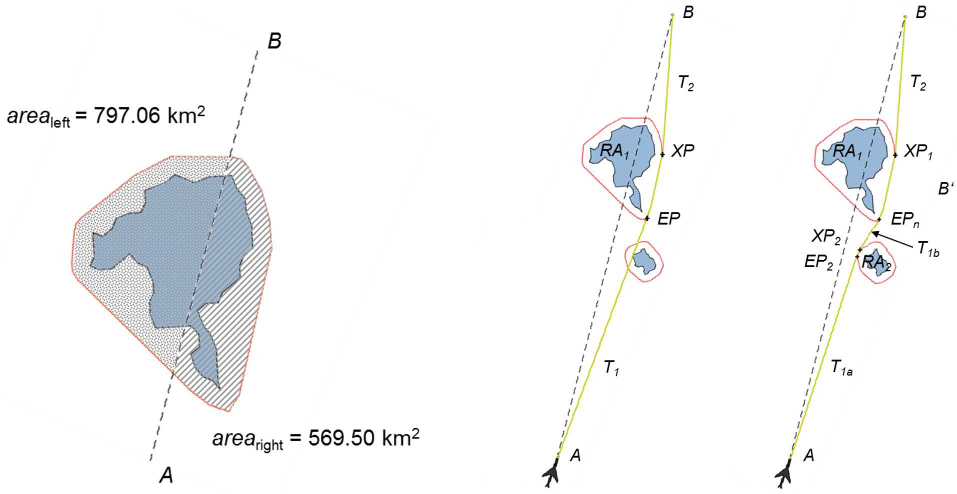

(a) Deviation direction decision making.

(b) Deviation route determination.

Figure 4.2: (a) Deviation direction decision making based upon risk area (red contour) extension left (dotted) and right (hatched) of the route (dashed black line). This decision strategy will lead to a right-wise circumnavigation. (b) Deviation route determination in two steps: The avoidance route around the conflicting risk area RA_1 is built from tangent $\overline{A\,EP}$, polygon section from tangent sampling point EP, referred to as entry point, and exit point XP and tangent $\overline{XP\,B}$. The tangents are checked for new conflicts which is the case on T_1. In a second step a deviation route from A to B', which is shifted to risk area RA_1, is calculated. The final route is then pooled from T_{1a}, polygon section $EP_2 - XP_2$, tangent T_{1b}, polygon section $EP_n - XP_1$ and tangent T_2.

is repeated until all conflicts are solved by the substitution of the tangent by at least one new set of two tangent sections pooled with a risk area segment. Finally, the deviation route between the original points A and B consists of alternating tangent sections and risk area segments. Due to the successive generation of route segments and the repeated decision making regarding the deviation direction, the found route is not necessarily the shortest possible – it rather represents a solution a pilot would likely have chosen in the same situation.

The just determined deviation route is valid for the static set of weather objects and risk areas but with flight time the atmospheric situation will develop, cells will move, emerge and disappear and new conflicts may arise. Thus, the deviation route is passed back to DIVMET where the flight movement is simulated while accounting for basic kinematics with constant flight velocity.

New weather information might become available because of an update of newly observed cells or due to a limited view which moves with the aircraft and thus continuously discloses new parts of the weather situation at every time step of aircraft movement which is typically set to 3 seconds. Thus, DIVMET checks the latest route for conflicts whenever new information is available and, where required, calls MET2ROUTE until the final destination is approached.

4.3 Features

In order to allow for different scenarios and due to demands recognised while developing DIVMET, some features were implemented that in their combination form unique characteristics of the tool.

4.3.1 Field of view

The degree of knowledge about the adverse weather given by a data set is essentially represented by the applied field of view in DIVMET, exemplary shown in Figure 4.3. When simulating the actual deviation behaviour of pilots, decision making in the model is based on a limited field of view that in shape of a circular segment represents the on-board radar field. According to what has been described in Section 2.4.1, the radar field size in the model is defined by the two variable parameters, range and opening angle, which typically are around 100 NM and between 80° and 120°, respectively. The range of 100 NM allows for monitoring the situation along the planned path up to almost 45 minutes ahead when assuming a constant en-route flight velocity of $900\,\mathrm{km\,h^{-1}}$.

The information gained by an on-board radar in flight gives an impression on the always current situation on adjacent flight levels ahead of the aircraft. In contrast to that, in DIVMET weather data of all modes is extracted from ground-based radar observations which are typically updated every 5 to 15 minutes. Weather extraction in the limited field of view mode can be imagined as being based on a circular segment overlaid to the radar image and defining the reduced set of weather information by the overlapping area. Conflict detection and resolution in this mode, thus, is limited to the previously reduced set of weather information, namely those weather objects or parts of them within the imaginary on-board radar field of view. Only these cells will be passed to and considered by MET2ROUTE which calculates a deviation route. Thus, the deviation initiation is rather close to the conflicting risk areas. Adverse weather further ahead will successively be recognised when flying along the route which has to be re-planned over and over again as shown in Figure 4.3(a).

The full knowledge of the weather situation is the opposing mode given in Figure 4.3(b). All cells along the route and apart from it are recognised instantly and accounted for in MET2ROUTE's re-routing process. More efficient routes are thought to be found in this mode compared to limited view. The benefit of future procedures that may account for increased hazard awareness in the cockpit are able to be evaluated with these two modes. Expensive data communication links may allow for uplinks of simplified ground- or satellite-based observations. The advantage is to get the overall impression of the weather situation what enables instant planning of the deviation route to the destination. Route updates only become necessary with weather updates. Together with the weather data the calculated deviation route may be uplinked and displayed in the cockpit to suggest an efficient solution to the pilot who decides whether or not to take it.

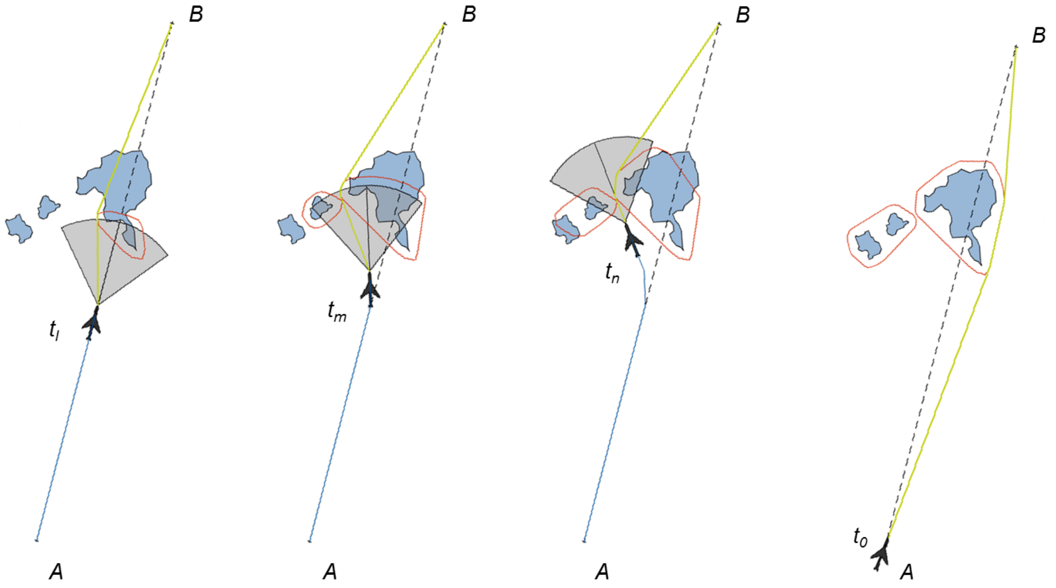

(a) Limited view. (b) Full view.

Figure 4.3: Weather avoidance routing under consideration of different information horizons. (a) Subsequent route (green) adaptation necessity when having limited weather information, for instance given by the on-board radar represented by grey circular sectors. (b) Instant avoidance route finding with spatially unlimited weather information, e. g. obtained by data uplinks.

4.3.2 Safety distance

Depending on the kind of adverse weather pilots need to take different safety measures. Weather objects representing the hazardous regions in DIVMET may be penetrable for certain certificated aircraft but more often and especially in case of thunderstorms need to be avoided while accounting for an additional safety distance (HAUF *et al.* 2013). Regulations by NATS (2010) recommend to avoid intense convective cells by 10 NM at flight levels below 20,000 ft; above this level 20 NM shall be maintained. According to FAA (1983) severe thunderstorms (return signals of 40 - 50 dBZ = heavy, > 50 dBZ = extreme according to ATC Weather Radar Echo Terms and Conditions) should generally be avoided by at least 20 NM. The gap between neighbouring cells is allowed to pass if these are separated by at least 40 NM. Areas with thunderstorm coverage of 60 % should entirely be circumnavigated. However, individual pilot behaviour strongly differs from these official recommendations. DELAURA and EVANS (2006) studied the thunderstorm circumnavigation within an US airspace corridor and found a distribution of held distances rather than a step function. Following their results, human factors such as the personality of the pilot and his proximity to the home base or the aircraft load, whether passengers or freight, control decision making by the pilot.

In in-house studies with DIVMET actual arrival routes in the terminal manoeuvring area (TMA) of Hong Kong International Airport were analysed. Weather objects representing regions with reflectivities exceeding 36.5 dBZ were mostly avoided by about 2 NM distance (Sauer *et al.* 2015b).

In DIVMET, a fixed safety distance is considered which however can be varied from simulation to simulation. Identified weather objects (parts of cells within the field of view) are enlarged by the safety distance. First, a convex hull is formed around each of these weather objects. Second, the convex hull is enlarged equivalently to the uncertainty margin presented in Section 3.5 but with a constant safety distance. This way the so called convex safety margin is formed around each weather objetc what results in new objects (red polygons in Figure 4.4(a)) referred to as risk areas along which the deviation route is calculated (Hauf *et al.* 2013).

Due to the enlargement of each weather object merging processes may emerge in multi-cell environments. These occur whenever two or more risk areas do overlap and, thus, close gaps to fly through. Therefore, the larger the safety distance the more likely is the creation of blocking structures (see Figures 4.4(a) - (c)). Especially in squall line situations enlarging weather objects may result in long detours as no come through is available because of overlapping risk areas.

For computing a deviation route around the merged structure a new convex polygon is formed that envelopes all overlapping risk areas (Hauf *et al.* 2013). Depending on their geometric configuration the new convex hull may also cover large concave areas that rather do not pose a risk to aviation. Routing solutions to destinations within such a concave area require a special treatment by subtracting the respective section from the convex polygon shown in Figure 4.4(d). For details please refer to Hupe (2015).

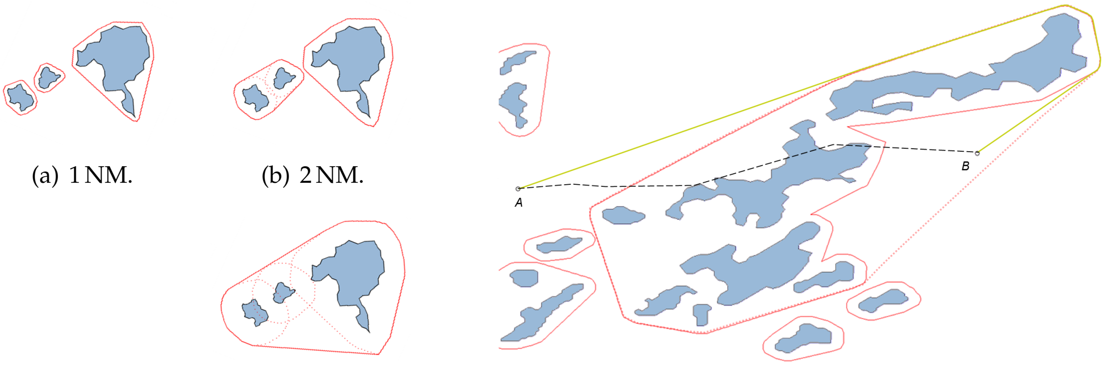

(a) 1 NM.

(b) 2 NM.

(c) 5 NM.

(d) Special treatment of concave sections to allow for routing to an airport within the respective section.

Figure 4.4: (a) - (c) Weather objects (blue) enlarged by individual safety distances form different risk areas (red dotted contours). The larger the safety distance the more individual risk areas do overlap and are convexly shaped in (b) and (c). They may cover large harmless areas which require special treatment to enable routing to the destination located within the convex polygon but outside any individual risk area (d, based on Hupe 2015).

4.3.3 Moving weather

Convective cells are not static but do move and evolve with time. Advection with the mean wind of the steering level at 500 hPa ($\sim$ 5 - 6 km) is superimposed by the life cycle of a cell including its development with growth followed by a shrinkage until the cell dissipates.

The dynamics of cells ahead of the aircraft are continuously observable by the pilot, either by eye or via their displayed radar response. The weather representation in DIVMET is dynamic but discretised to the update rate of radar data. Between two updates and for calculation in MET2ROUTE the weather situation is considered as being static (HAUF *et al.* 2013). Due to the relation of velocities of the involved systems this simplification is acceptable. As stated above, aircraft en-route fly at speeds of about $900\,\mathrm{km\,h^{-1}}$ ($=250\,\mathrm{m\,s^{-1}}$). Thus, within two data updates with rates of 5 or 15 minutes aircraft cover a distance of 75 km or 225 km while convective cells travel with mean wind of about $15\,\mathrm{m\,s^{-1}}$ which results in a displacement of 4.5 km or 13.5 km, respectively.

Compared to reality where the pilot is continuously able to monitor the cells development and likely adjusts the flight route, the simulation may fail in this continuous conflict-free adaptation. Due to the timely discretisation of weather information cell encounters may occur in the simulation when a cell, regardless of whether new or developed, is located above the current aircraft position. The latter may be either within the weather object or just in the safety margin around it. In the latter case re-routing considers the shortest way out of the risk area while changing the flight direction as little as possible and further account for avoiding this risk area. If the aircraft is within the weather object, the heading remains and the flight continues through the cell as this is recommended practice after thunderstorm encounters (see e. g. in NATS (2010)).

4.3.4 Route options

Diversion route calculation in DIVMET is executed between two points A and B as soon as a weather conflict on the planned trajectory occurs. This trajectory may consist of only two or a whole set of waypoints that define a straight or arbitrary cornered route, respectively. In the latter case different options arise which points A and B on the route to choose. In HAUF *et al.* (2013) four options had been envisaged which were implemented since then as shortly detailed in HUPE *et al.* (2014):

Free Flight disregards all waypoints of the planned trajectory and just bases the re-routing on current position A and destination point B. This option allows for the most efficient routing though the deviation route might not be similar to the declared one.

Rejoin Route is an option that accounts for returning and continuing with the planned trajectory after having avoided the weather conflict on a diversion which has been instantly initiated after conflict detection. Deviation routes are subsequently calculated to waypoints behind the weather conflict, each serving as a potential rejoin route point B', referred to as return capture fixes by (MCNALLY *et al.* 2012). Starting with the closest waypoint to the conflict the first one is searched at which the required heading change is equal or less 30° when rejoining the planned route.

Leave Later accounts for the planned routing as long as possible and chooses A', the so called leave route waypoint, which is referred to as the manoeuvre starting point by (McNally *et al.* 2015), the way that it is the latest to initiate the deviation around the conflicting risk areas while satisfying the 30 degree heading change criterion. Point B remains at the destination point of the planned trajectory. Thus, once the former route is left at A' its further path is disregarded and B is directly headed for on a safe weather conflict-free deviation route. This option implies a kind of wait and see mode as the deviation is not directly initiated but the flight is continued on the planned route for the time being. Weather updates may lead to conflict dissipation what then might allow for continuing on the declared route without any deviation.

Smallest Deviation combines the *Leave Later* and *Rejoin Route* options and thus, accounts for the longest possible alignment with the planned trajectory. Only route segments with weather conflicts are substituted by a calculated diversion route. The resulting route may be less efficient but complies the most with the declared route.

The calculated deviation route from each of the route options is then linked with route section flyable on the planned route (current position A – A′ – diversion – B′ – destination B) to build the complete conflict-free route. These resulting routes for all four route options are visualised in Figure 4.5.

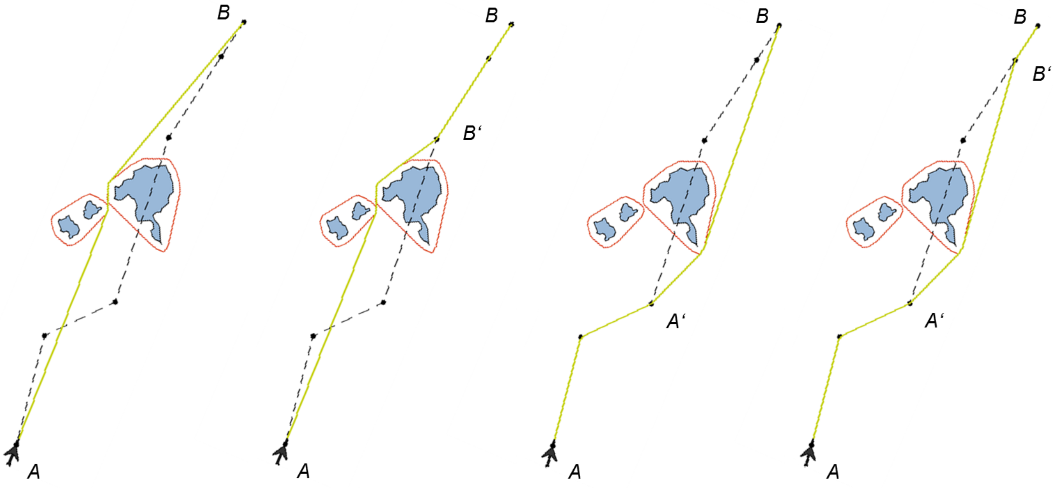

(a) Free Flight. (b) Rejoin Route. (c) Leave Later. (d) Smallest Deviation.

Figure 4.5: Route options in DIVMET.

The introduced heading change criterion of 30° was suggested by Austro Control, the Austrian ANSP, and originates from passenger comfort that should not be negatively affected (Hupe *et al.* 2014). In DIVMET, however, this value is adaptable. An invention of new, additional points on the direct link between two subsequent declared waypoints for deviation or return with a heading change angle of exactly 30° is implemented. Though, for the Monte-Carlo simulations described and analysed in Chapter 5 an arbitrary point with certain distance to the risk area is determined and used as leave route point A' regardless of the required heading change.

4.3.5 Reactive vs. proactive routing

Navigation in DIVMET is based on the weather data set defined as being relevant in the simulated situation. When using observational information weather data is updated whenever it is available. Thus routing is reactively adapted to the dynamic weather situation (HAUF *et al.* 2013). Due to the timely discretisation of the weather information inefficient deviation manoeuvres may occur in the simulation as cells may pop up or are displaced to a position directly in front of or above the aircraft which would not happen in reality as the pilot continuously monitors the situation and intuitively thinks about the further cell development and location.

Thunderstorm nowcasts can be used equivalently to observational data for reactive routing. In fast time simulations nowcasts facilitate trajectory and arrival time predictions. To do so, the latest release of nowcast data is taken at a certain time, for instance when an aircraft enters the TMA on which it is focused in one application of DIVMET. Approaches to Hong Kong International Airport are simulated based on SWIRLS nowcast fields. The extracted nowcasted cells for different lead times (up to one hour) are subsequently treated as the valid situation at proceeding simulation time. Within a couple of seconds a trajectory of a one-hour flight is determined according to the probable weather development.

When simulating in real time, nowcast information fills the gap of missing continuous data. Apart from the observational data, nowcasts for e. g. five minutes ahead can be used simultaneously to prevent a sudden conflict because of a weather updated cell in the vicinity of the aircraft. Consideration of the future position of a cell, thus, enables a temporary proactive routing, meaning that not yet existing cell stages are accounted for in route calculation. This, however, is limited to the first lead time of image based nowcast products as all cells of each lead time set is considered and merged in DIVMET which would result in large structures when using data of several lead times.

On the contrary, as deliberated by SCHARF (2013) and presented by SAUER *et al.* (2015a), object based nowcast information, like those from Rad-TRAM or Cb-TRAM, facilitate proactive routing over longer time horizons. From a data set of several cells issued at time t_0, an individual lead time t_{0+x} nowcast for each cell is selected according to the potential time of conflict, i. e. the flight time t_x distance to the cell (see Figure 4.6). An artificial set of relevant cell stages is created which does not represent a situation observable at one certain time. It consists of cell stages said to be valid at different times along the flight. Lead time-dependent uncertainties as analysed in Chapter 3.3.2 for Rad-TRAM data can be applied then by enlarging each relevant cell by the respective margin.

Updates may be integrated by applying the same selection procedure to upcoming nowcast releases (t_5, t_{10}, ...) which are likely less uncertain and from which the maximum

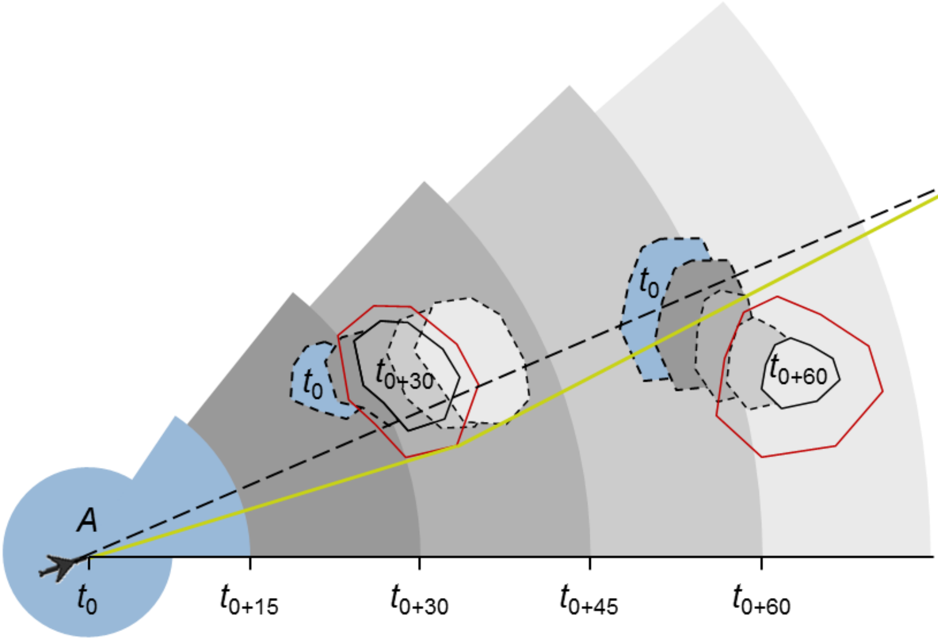

Figure 4.6: A selection algorithm determines the object-dependent relevant lead time t_x based on the radial flight time distance to each respective (nowcast) cell (dashed contour and blue [obs] / grey filling). If lead time and flight time distance correspond (here: cell and background have same colour) the cell is assumed to be relevant (solid contour). It is enlarged either by the safety distance, or, as will be detailed in Section 5.1, by the direction- and lead time-dependent uncertainty margin. An artificial field of cell stages valid at different times is created and a deviation route (green) is proactively determined (based on (SCHARF 2013).

lead time as well as the respective uncertainty margin for the flight decrease.

This proactive handling enables an early route commitment which might be of interest for the intended 4D trajectories in European airspace (SESAR JOINT UNDERTAKING 2012). If uncertainties are considered correctly, no further route adjustment might be necessary during the flight and, thus, additional workload for controllers in adverse weather situations is minimised.

4.3.6 Coupling to an air traffic simulation model

DIVMET as a stand alone model allows for provision of a deviation route for one single aircraft while accounting only for basic kinematics. As non-linear knock-on effects may result from single aircraft deviations, e. g. aircraft-aircraft conflicts or air space congestion, a system-wide view is important. This can be achieved by coupling DIVMET to an air traffic simulation model for which NAVSIM was selected (HAUF *et al.* 2013). The latter is a global 4D model developed by ROKITANSKY at University of Salzburg, Austria. NAVSIM was originally build to analyse satellite communication capacity demand for future aviation concepts (ROKITANSKY 2009). The model allows for precise simulation of several thousand aircraft simultaneously from gate to gate and according to a specific aircraft performance model called BADA (Base of Aircraft Data) which is provided and maintained by EUROCONTROL (2015) in cooperation with aircraft manufacturers and airline operators.

In the coupled mode aircraft and their respective trajectories are subsequently processed in DIVMET. A software library builds the interface and enables simple XML format messaging. Via controller-pilot data link communications (CPDLC) messaging information on flight trajectory and current position are transmitted to DIVMET (GRÄUPL *et al.* 2012). This model synchronises the trajectory with the latest available weather information and determines an individual diversion for the particular flight. The diversion route is then passed back to NAVSIM. The former trajectory is substituted by the provided deviation route on which the further flight is simulated in NAVSIM according to the specific aircraft performance data. DIVMET continues with the next flight until all flights are processed. As this procedure takes some time (several seconds per flight), NAVSIM may be stopped to avoid any delays arising in the deviation route determination because of a continued flight on the former trajectory after a weather update. The procedure is repeated whenever new weather information is available, i. e. due to a weather update and/or every moment when a limited field of view is applied. In the latter case subsequent processing of all flights is steadily repeated while continuously simulating with NAVSIM (HUPE *et al.* 2014).

Simulating DIVMET's provided deviation routes with NAVSIM allows for precise statements on flight profiles and overflight/target times. Approach route and arrival time predictions as described in Section 4.3.5 for Hong Kong International Airport become more accurate by the combination of DIVMET and NAVSIM. Coupling the two models additionally enables to analyse system effects of deviation manoeuvres. Aircraft-aircraft conflicts are one of such knock-on effects which may grow to non-linear scales. This type of conflict can be analysed but not yet resolved with NAVSIM. Equivalent to the intention of MCNALLY *et al.* (2015), the provided deviation routes can rather be seen as suggestions to pilots which shall still be controlled by ATC to assure safety.

Diversions may also cause a shift in sector load. Weather affected regions are avoided which results in congestion along the edges of the risk areas. During the deviation procedure aircraft potentially penetrate adjacent sectors and increase the load there. In a project called MET4ATM initiated by Austro Control, an analysis on this issue has been performed based on weather and trajectory data of 17 July 2010. Simulated routes in coupled mode and the resulting sector conditions were confronted with the planned and actual situation in order to evaluate the feasibility of sector load predictions (SAUER *et al.* 2013; HUPE *et al.* 2014; HAUF *et al.* 2015).

In the stand-alone mode, DIVMET is used in the upcoming study, the set-up of which is presented in the following Chapter. In the performed simulations either the free flight option or a tactic similar to the leave later procedure but without pre-defined waypoints, is applied.

5 Diversion tactics in Monte Carlo simulations with DIVMET

In aviation the responsibility to find a safe route around a thunderstorm or through a field of storms resides with the pilot. Due to his limited sight on the actual weather situation and the lack of knowledge on its further development deviation routes are often inefficient. This is mostly due to late initiation of a deviation or an unfortunate decision making. Weather avoidance models such as DIVMET facilitate early re-routing. But what would be the effect then? Is there an optimum planning or deviation initiation horizon?
In order to identify the effect of different strategies concerning efficient routing in thunderstorm situations, diversion routes calculated by DIVMET are consulted. A Monte Carlo approach is applied, which is generally useful regarding sampling, estimation and optimisation of processes (KROESE *et al.* 2014). Such methods allow for deducing the statistical sample distribution (MOONEY 1997). Each cell of the analysed Rad-TRAM data set of 15 July 2012 is treated as being a random sample representing a typical thunderstorm cell over Central Europe. The effect of a number of defined routing tactics is then sampled by running DIVMET in the respective strategy set-up subsequently with each of the data set cell.

5.1 Methodology and study set-up

The 563 identified Rad-TRAM cells (cell IDs 0-562) of 15 July 2012 and their respective nowcasts serve as the meteorological base of this study. Each individual cell cycle is treated separately. Its first identified stage, location and movement direction defines the considered planned trajectory for the respective case in a prototyping way.
Among other possible geometrical variations, the trajectory set-up is chosen so that the aircraft always follows the cell and outruns it eventually. The departure point A is located against the cell movement direction in distances corresponding to flight times t_x varied between $5, 10, ..., 60$ minutes. The time span of 60 minutes allows to apply the full nowcast horizon. With a constant flight velocity of $250\,\mathrm{m\,s^{-1}}$ the flight distance l_x to the cell gravity centre is up to 900 km long. As the main interest is in the deviation tactic in front of the conflict and the resulting detour effects, destination point B is set to a flight time distance of two hours ($l_{120} = 1800\,\mathrm{km}$) behind the cell so that it has not much influence on the detour (see Figure 5.1). However, this effect will be treated analytically in Section 5.2.1. Geographical coordinates of both points are determined by gravity centre displacement in and against the movement direction along the great circle on the WGS84 geoid. Thus, the planned flight time varies between 2 hours plus 5 minutes and 3 hours,

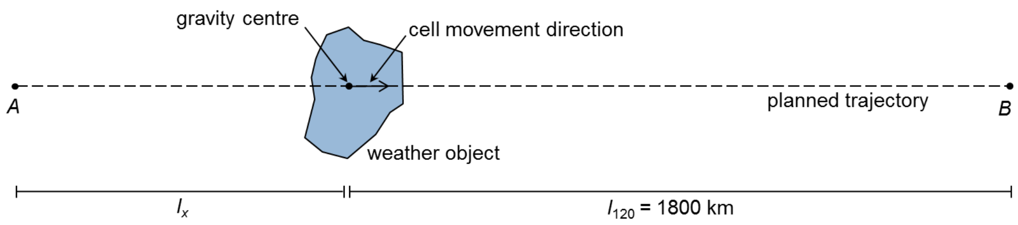

Figure 5.1: Trajectory set-up for Monte Carlo simulations. Start distance l_x varies between distances covered in flight times t_x of 5, 10,..., 60 minutes at $250\,\mathrm{m\,s^{-1}}$. l_{120} is the distance flown in 2 hours.

which is representative for medium-haul flights over Europe.

Aircraft and weather object start with the same movement direction, however, that of the latter may change during its development and the cell may move to either of the sides or even lurch about as exemplary indicated in Figure A.9 in the Appendix. It resembles a random walk – a terminology first used by PEARSON (1905) and further detailed by SPITZER (1976) – as visualised by cell gravity centre tracks in Figure A.2 in the Appendix. Thus, the deviation from the planned route is strongly dependent on the lateral extent of the weather relative to the planned or adjusted trajectory. The changing lateral extent of the cell and its misplacement in nowcasts (see Fig. 3.10(b) and panel plot in Fig. A.7 in the Appendix) is the main covered part of weather uncertainty in this study. Dissipating cells will also have a great impact as will be seen later on. Whenever new weather information is considered, the diversion route is adjusted to the new situation.

DIVMET's free flight route option is applied in the numerical simulations. So the deviation and, finally, the detour as the difference of diversion and planned route is mainly influenced by the lateral extent of the considered cell plus the applied safety distance. Due to the comparatively very small lateral extent that has to be avoided on the planned long distance, the envisaged detours will be small. An analytic consideration is performed in Section 5.2 in order to assess the ranges to expect.

In order to cover possible flight tactics, several scenarios are defined as detailed in the following. For each parameter setting (see them summarised in Tab. 5.1) of the scenarios 563 flights – one to each cell ID – are simulated. In a parameter study, the departure or conflict recognition distance l_x is additionally varied between 5, 10, ..., 60 flight minutes to the gravity centre, so that twelve simulation runs are performed per scenario configuration.

Simulation scenarios

A set of scenarios is defined to cover different weather information stages and possible tactics how to account for the available weather information. What is the effect of different weather information and its update rates? Should the pilot immediately react to the latest weather data or is it rather efficient to wait for more current data when approaching the situation? What is then the best time to initiate any deviation? These are only some questions concerning strategies applicable when being limited to observational data.

If nowcast information is available, questions need to be answered whether it is worth to trust the nowcast and deviate immediately. How reliable and precise is this data? Should the defined uncertainty be considered or does it lead to unreasonable detours? What would be the benefit of data uplinks versus the latest nowcast set retrieved before departure? In order to evaluate the former questions, three scenario blocks are defined and detailed in the following.

1) Observational data. In this scenario flights depart in flight distance l_x covered in t_x = $5, 10,..., 60$ minutes and directly recognise the first state of the convective cell which is updated every 5 minutes. The applied deviation tactic is then varied as follows:

- *Reference* scenario. The route is instantaneously adapted to the weather situation as shown in Figure 5.2(a). Due to the forced instantaneous reaction the aircraft automatically deviates from its individual planned trajectory. After each weather update the diversion route is reactively adjusted (see Figure 5.2(b)) and the direction of diversion may be switched (not shown) because of the new location of the cell relative to the direct link between current position and destination B. In cases where the lifetime of the cell is shorter than the flight time t_x to the cell, the deviation would not have been necessary. This is one among other parameters evaluated in Section 6.
- *Wait and see* scenario. The decision to deviate is delayed as can be seen in Figure 5.2(c). Even though the weather conflict is recognised, the flight is first continued on the planned trajectory until a certain flight time distance l_i to the convective cell is reached. If still necessary, a diversion route is calculated according to the then actual weather situation and the deviation is initiated. Cells that disappeared in the meantime or those which were displaced sidewards may not pose a risk anymore. In these cases no deviation is neither necessary nor initiated at any time.
  Again, after deviation initiation the route will be reactively adjusted to the upcoming cell development which is updated every 5 minutes.

2) Departure nowcast sets. They describe the latest available nowcast information released before or at departure. This scenario is equivalent to a common strategy in which the pilot gets the latest information just before departure. Due to missing data-link techniques no update is available during flight. In reality, the pilot will visually monitor the nearby situation and may take the nowcast information into account when initiating any deviation.

In the simulation the trajectory is again planned based on the first identified cell stage and its characteristics regarding gravity centre and movement direction. Depending on the applied data source, the respective cell stage – valid at or nowcasted for time t_{0+x} – is selected and the aircraft is proactively re-routed, comparable to a re-planning before sharing the RBT. No route adaptation to the actual situation is then considered. However, the weather development is monitored and cell encounters are counted when the aircraft

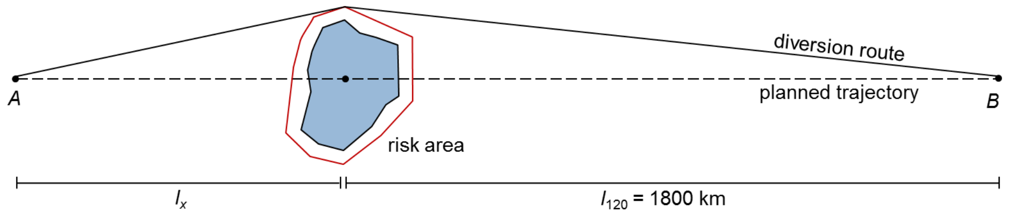

(a) Diversion route in *reference* scenario at time t_0.

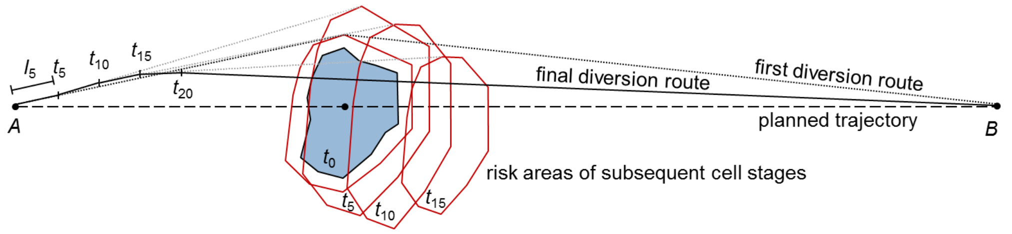

(b) Final diversion route in *reference* scenario after cell dissipation at time t_{20}.

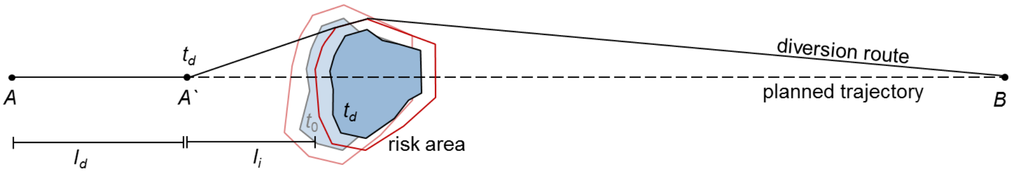

(c) Diversion route in *wait and see* scenario at time t_d.

Figure 5.2: (a) Simulation principle of *reference* scenario: an initial diversion is instantly initiated around the conflict recognised at departure time t_0. (b) At rates of 5 minutes weather updates lead to an reactive adjustment of the initial diversion route. After cell dissipation (here at time t_{20}) the route is directed towards destination point B. No further adjustment is necessary. (c) In the *wait and see* scenario the deviation initiation is postponed to time t_d when the aircraft reached a distance l_i to the then current cell. The shown first diversion valid at t_d will be reactively adjusted.

position is within a weather object.
Four scenarios are defined that differ either in the applied data or the considered avoidance distance:

- *Perfect nowcasts* can be obtained by observational data in retrospect. At departure point A the life cycle of the cell is checked if it covers or even exceeds the planned flight time t_x. If so, the respective cell stage valid at time t_{0+x} is selected and used for deviation route determination as given in Figure 5.3(a). Otherwise no diversion is initiated.

- *Rad-TRAM nowcast data* of the latest release at departure is taken to select the best guess of the cell stage that is valid at the probable time of conflict t_{0+x}. The diversion is oriented towards and around a risk area that is formed by the selected cell stage enlarged by either
  - a constant safety distance of 2 NM (see Fig. 5.3(b)),
  - the direction- and lead time-dependent 90th percentiles uncertainty margin as

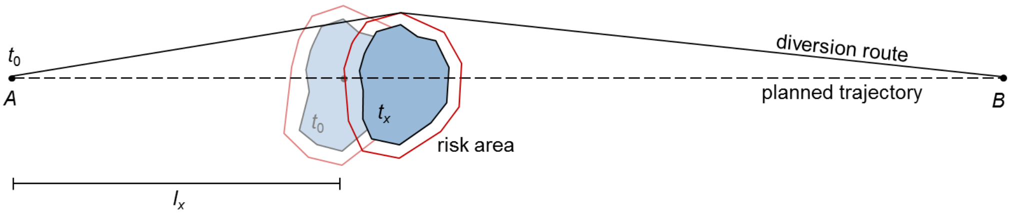

(a) The *perfect nowcast* scenario with safety distance.

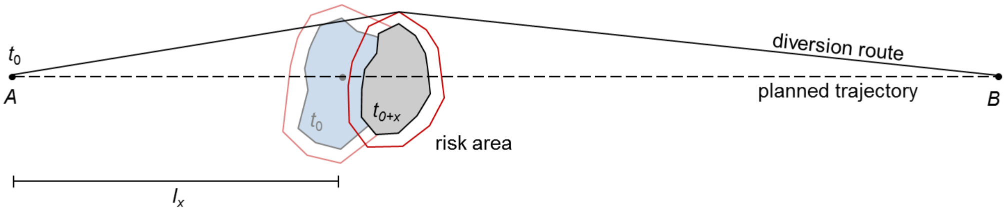

(b) The *departure nowcast data* scenario with safety distance.

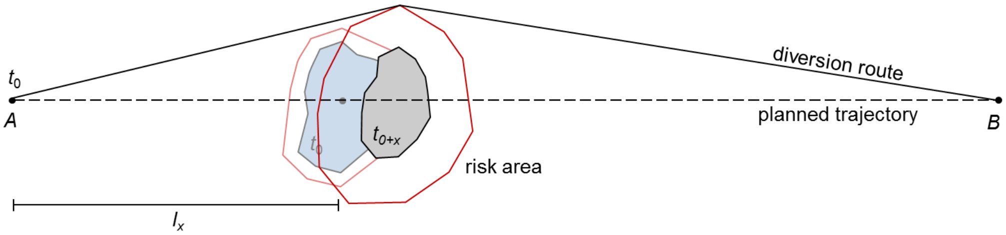

(c) The *departure nowcast data* scenario with uncertainty margin.

Figure 5.3: Simulation principle and data differences in the *departure nowcast* scenario. (a) In the *perfect nowcast* scenario the cell stage valid at time t_{0+x} is selected and the aircraft is proactively re-routed while accounting for 2 NM safety distance if the cell still exists. Instead of observational data, the Rad-TRAM nowcast issued at t_0 for lead time t_x is selected and enlarged either by (b) the safety distance or (c) the uncertainty margin.

defined in Section 3.5 (see Fig. 5.3(c)) or

- both, the variable uncertainty margin plus 2 NM safety distance.

However, any diversion might be completely needless as the actual cell disappeared or has not posed a risk to the original trajectory anymore when the aircraft approaches it. In contrast to the *perfect nowcast* scenario, nearly all flights will proactively re-route in this scenario as Rad-TRAM, in its current state, always give nowcasts up to 60-minutes lead time for each observed cell. Although, no update neither of the nowcast nor of the route is considered, cell encounters regarding the actual situation are monitored for the later evaluation.

3) Nowcast updates enable to reduce the uncertainty in the considered data and a allow for a more efficient routing. This scenario presents a combination of the former ones. Each individual trajectory is planned based on the first observed stage of a cell. Proactive deviation routes are then determined – either instantaneously or with a delay – according to the respective selected nowcast which is enlarged by either the safety distance, the uncertainty margin or the sum of both.

- *Instantaneous deviation* accounts for the first nowcast set released at departure from which the nowcast with lead time t_x equal to the planned flight time distance to the cell is selected. Thus, the initial deviation of all flights in this scenario is equal to that accounted for in Scenario 2. Here, however, the nowcast is updated at 5-minutes rates. As the situation of interest is fixed to time t_{0+x} the considered lead times decrease whereby the certainty increases. Thus, the applied uncertainty margin becomes smaller. With each nowcast update an adapted proactive deviation route is determined.
- *Delayed deviation initiation* enables then to prevent diversions at all for such flights that are related to short-living cells. Equivalent as in Scenario 1, no deviation is initiated if the cell dissipated within time t_d. Otherwise, a proactive route is determined according to the then latest nowcast release at or shortly before t_d from which the respective nowcast with lead time t_{x-d} (valid for time $t_{d+(x-d)}$) is selected. Once the deviation is initiated, the route is updated whenever a new nowcast is released as described above.

An overview on the scenario parameters is given in Table 5.1. For each of the parameter settings twelve simulation runs for all 563 individual cell cycles are performed with departure flight times t_x varied between $5, 10, ..., 60$ minutes to the cell gravity centre.

Table 5.1: Overview on parameters of the simulated scenarios.

Scenario name	Weather update rate [min]	Deviation initiation delay [min]	Safety distance [NM]
Observational data			
Reference	5	—	2
Wait and see	5	5 – 55	2
Departure nowcast sets			
Perfect nowcast	—	—	2
Nowcast	—	—	2 / um* / um + 2
Nowcast updates			
Instantaneous deviation	5	—	2 / um / um + 2
Delayed deviation initiation	5	5 – 55	2 / um / um + 2

* direction- and lead time-dependent uncertainty margin

Before discussing the simulation results some of the just detailed scenarios will be analytically assessed in order to identify relations and border cases and get an idea of the magnitude of certain set-up effects. However, the simulations account for real and dynamic data, what is only considered to some degree in the following assessment.

5.2 Analytical assessment of some selected scenarios

In order to find a general answer on the detours to anticipate from the simulations and to identify border cases, an analytical formulation is found for some of the earlier discussed scenarios. The basic deviation problem is simplified as shown in Figure 5.4 and, first, the weather situation is assumed to be static.

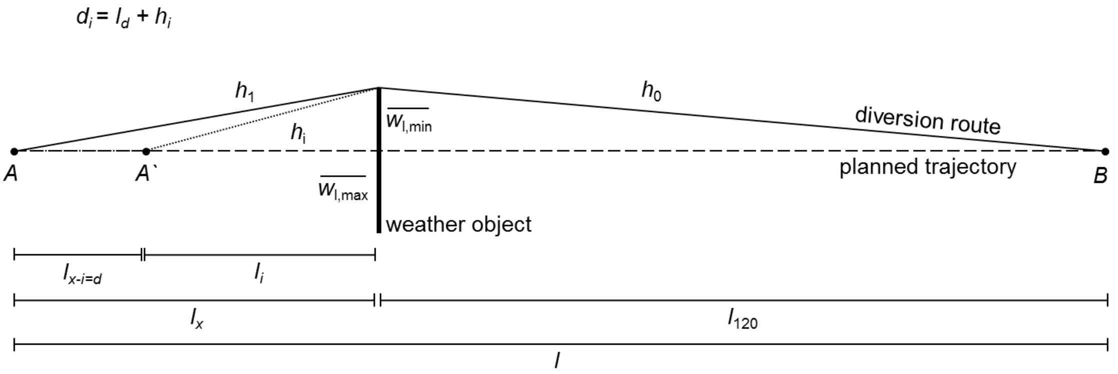

Figure 5.4: Geometrical set-up and theoretical diversion route of the *reference* and *wait and see* scenarios.

The planned trajectory of distance l_x to the cell gravity centre and the two hours flight time distance ($l_{120} = 1800\,\mathrm{km}$) behind is given as a straight dashed line. The bold vertical line represents the weather object reduced to one dimension. As the lateral extent of a cell basically determines the detour of the diversion route in this study, this simplification is an appropriate approximation. In DIVMET, the decision whether to deviate to the left or right is based upon the weather object area or risk area on each side of the route. However, for this analytical consideration it is assumed that the smaller lateral extent $w_{\mathrm{l,min}}$ is on the side of the route where the risk area is smaller, what indeed is not necessarily the case.

The identified convective cells of the Rad-TRAM data set are analysed regarding their extents in the four considered directions. The mean extents of all observed cells as well as of all first detections of a cell are summarised in Table A.1. The always smaller lateral extent $w_{\mathrm{l,min}}$ (sometimes on the left side, other times on the right side) averages to

$$\overline{w_{\mathrm{l,min}}} = \frac{1}{N} \sum_{N} min(w_{\mathrm{left}}, w_{\mathrm{right}}) = 6783.6\,\mathrm{m}. \tag{5.1}$$

First-time identified cells exhibit an average minimum extent of $\overline{w_{1,l,min}} = 4568.3\,\mathrm{m}$. The safety distance of 2 NM needs to be added to cover the mean lateral distance that is avoided in the simulations.

An estimation of detours resulting from either instantaneous re-routing or later deviation initiation around the always same weather situation was done by D. PACE GERZ (2014). From an integrated perspective, the overall flight distance, he deducted a recommendation how to react to a weather situation that is about to occur with certain probability. While PACE focussed on only two extreme cases (instantaneous re-routing and latest possible deviation directly in front of the cell) , here the effects of a postponed diversion should be evaluated analytically. Under the assumption of static weather the diversion route is straightly directed from point A to the risk area edge forming the hypotenuse h_1 of a right-angled triangle. Its length can be derived from Pythagoras' theorem

$$h_1 = \sqrt{l_x^2 + \overline{w_{\mathrm{l,min}}}^2} \tag{5.2}$$

where l_x is the negative defined, variably planned distance to the cell gravity centre in metres ($l_x = t_x \cdot 60\,\mathrm{s\,min^{-1}} \cdot v$ with departure flight time distance t_x in minutes and constant flight velocity $v = 250\,\mathrm{m\,s^{-1}}$). In case of a delayed deviation initiation at point A' the flown distance to the edge of the weather object is

$$-(l_x - l_i) + h_i = -(l_x - l_i) + \sqrt{l_i^2 + \overline{w_{\mathrm{l,min}}}^2} \tag{5.3}$$

where the negative defined distance l_i results from $l_i = t_i \cdot v$ with flight time t_i to the weather object. The second part of the diversion route is located behind the cell. The planned distance l_{120} is fixed in all scenarios by the time frame of two hours ($l_{120} = 2 \cdot 60\,\mathrm{min} \cdot 60\,\mathrm{s\,min^{-1}} \cdot v = 1800000\,\mathrm{m}$). Thus, hypotenuse h_0 is solely determined by $\overline{w_{\mathrm{l,min}}}$ via

$$h_0 = \sqrt{l_{120}^2 + \overline{w_{\mathrm{l,min}}}^2}. \tag{5.4}$$

The length h of the diversion route is the sum of the legs $l_x - l_i$, h_i and h_0:

$$h = -(l_x - l_i) + \sqrt{l_i^2 + \overline{w_{\mathrm{l,min}}}^2} + \sqrt{l_{120}^2 + \overline{w_{\mathrm{l,min}}}^2}. \tag{5.5}$$

Compared to the planned trajectory with flight distance $l = -l_x + l_{120}$ the detour D caused by the diversion h is the difference of both and a function of l_x and l_i:

$$D(l_x, l_i) = h - l = h + l_x - l_{120} \tag{5.6}$$

$$= -(l_x - l_i) + \sqrt{l_i^2 + \overline{w_{\mathrm{l,min}}}^2} + \sqrt{l_{120}^2 + \overline{w_{\mathrm{l,min}}}^2} - (-l_x + l_{120}) \quad \text{for } l_i \leq l_x \leq 0 \tag{5.7}$$

The normalised detour $D(l_x, l_i)/l$ is visualised on a logarithmic ordinate over the deviation initiation time t_i in Figure 5.5. The green solid line shows the normalised detours emerging due to different deviation initiation distances on a trajectory started in departure distance t_x of 60 minutes to the cell with minimum lateral extent $\overline{w_{\mathrm{l,min}}} = 6783.6\,\mathrm{m}$. Sampling points at 5 minute increments of t_i are given by individual markers for this and all other departure distances l_x. The solid black line marks the upper boundary of emerging normalised detours $D(l_x, l_i)/l$ for $l_x = l_i$. For this parameter combination the deviation is initiated instantly at departure position A. Compared to the small detour range resulting from differing l_x for one certain deviation initiation distance l_i (vertical

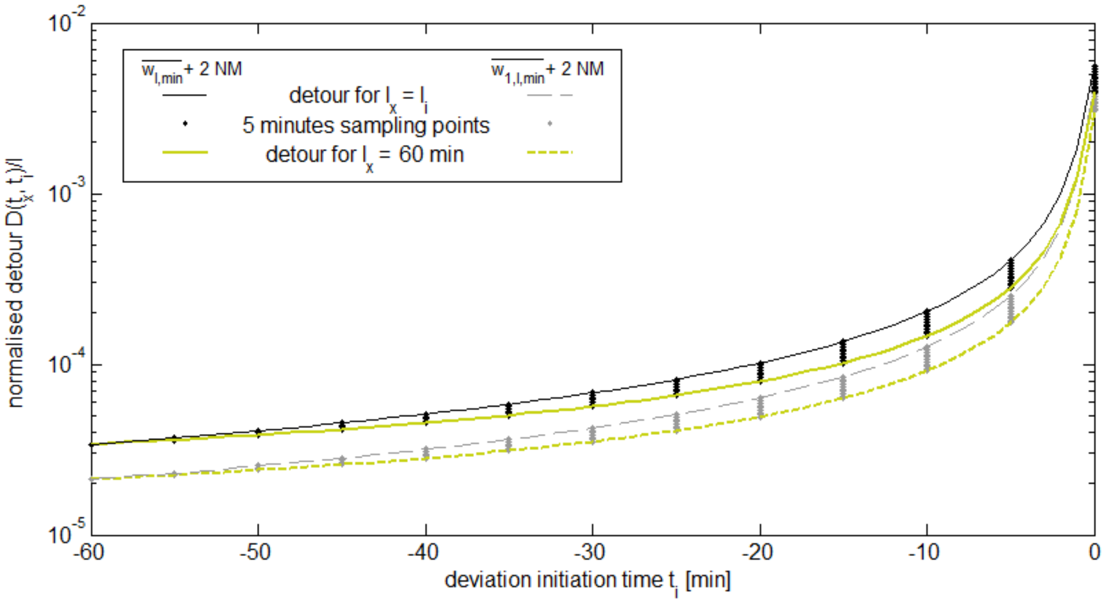

Figure 5.5: Normalised analytic detour $D(t_x, t_i)/l$ for a static object as a function of departure time distance t_x and deviation initiation distance t_i. Black colour and solid lines represent results for laterally avoided distance $\overline{w_{1,\mathrm{min}}}$ plus 2 NM safety distance, grey colour and dashed lines give results for the medial lateral extent of first time observed cells which is $\overline{w_{1,1,\mathrm{min}}} = 4568.3$ m plus 2 NM. The green line gives the respective detour for departure time distance $t_x = 60$ min. Markers indicate sampling points at 5-minute delay increments for different departure distances. The black and grey line link points at which the deviation is initiated instantly at departure ($t_i = t_x$).

range between green and black line), larger effects are introduced by the delayed initiation of a deviation (along the abscissa). The found relative detour rises from $3.4 \cdot 10^{-5}$ (≈ 90 m) for an instantaneous deviation in flight time distance $t_x = t_i = 60$ min, which represents the optimal path, by about two orders of magnitude to 0.027 % (≈ 730 m) when delaying the deviation to initiation time distance $t_i = 5$ min. When flying to the obstacle and only deviate then the relative detour is 0.39 % which is about 10.5 km. These small ratios are due to the geometric set-up with a long planned trajectory and a rather small laterally extended obstacle.

When accounting for an even smaller lateral extent of the weather object, e. g. $\overline{w_{1,1,\mathrm{min}}}$, the level of relative detours decreases as given by the dashed lines and grey sample points in Figure 5.5.

5.2.1 Detours due to delayed deviation and earlier return to route manoeuvres

The trajectory set-up applied in the presented study accounts for a very long flight distance behind the cell in order to exclude any additional detour effects caused by the destination or rejoin point. Note that the focus is set to the applied tactic in front of the weather conflict. So the question arises how the deviation initiation postponed to distance l_i affects the detour. This effect is geometrically assessed with a static weather object under consideration of parameters given in Figure 5.6(a).

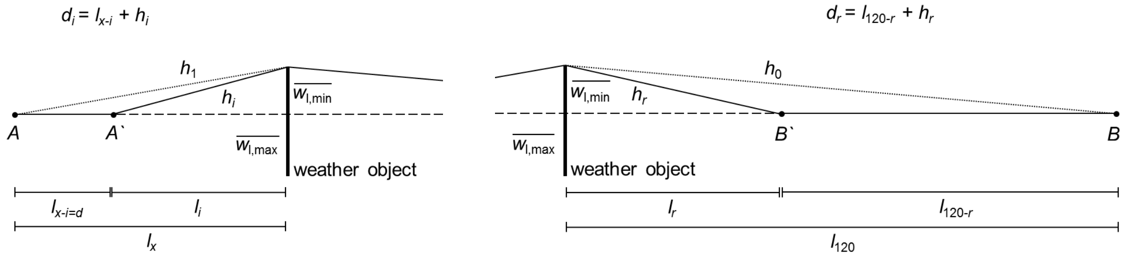

(a) Delayed deviation initiation.

(b) Rejoin route.

Figure 5.6: Geometrical set-up for the analytical assessment of the effect of (a) delayed deviation initiation and (b) earlier return to route manoeuvres on the detour.

The additional detour that is flown when postponing the deviation initiation is a factor f_1 slightly above 1 that can be derived from

$$f_1 = \frac{d_i}{h_1} = \frac{-(l_x - l_i) + \sqrt{l_i^2 + \overline{w_{1,\min}}^2}}{\sqrt{l_x^2 + \overline{w_{1,\min}}^2}}. \tag{5.8}$$

The shorter the departure time distance t_x and the smaller the deviation time distance t_i is, the larger the factor f_1 becomes what is recognisable in Figure 5.7(a). The solid line represents the maximum detour where the deviation is only initiated when the weather object is already reached ($t_i = 0\,\text{min}$). For departure time distances $t_x > 10$ minutes the maximum additional detour is less than 5 % independent of the deviation delay. Initiating the deviation after having flown 90 % of $t_x > 10$ minutes results in an additional detour of not more than 1 % (dashed-dotted line). Only when departing closer than 10 minutes flight time to the weather object an additional detour due to a delayed deviation initiation may elongate the diversion by up to 35 % compared to the respective instant reaction. The dashed line gives factor f_1 for deviations initiated after having flown on the planned trajectory for half of the departure time distance t_x given on the abscissa. The instantaneous re-routing defines the reference scenario that equals to $f_1 = 1$ (green line).

With loss of generality the destination point B is set to the by 2 hours flight time distance in direction of cell movement displaced cell gravity centre in this study. In numerical simulations with DIVMET the free flight option is chosen which prevents any earlier return to the route. What however would be the effect when rejoining the route earlier as suggested in Figure 5.6(b)? This question can be answered analogous to the delayed deviation initiation problem. Formula 5.8 is adapted as follows

$$f_0 = \frac{d_r}{h_0} = \frac{(l_{120} - l_r) + \sqrt{l_r^2 + \overline{w_{1,\min}}^2}}{\sqrt{l_{120}^2 + \overline{w_{1,\min}}^2}}. \tag{5.9}$$

The ratio f_0 of detours is plotted in Figure 5.7(b) as a function of rejoin time distance t_r

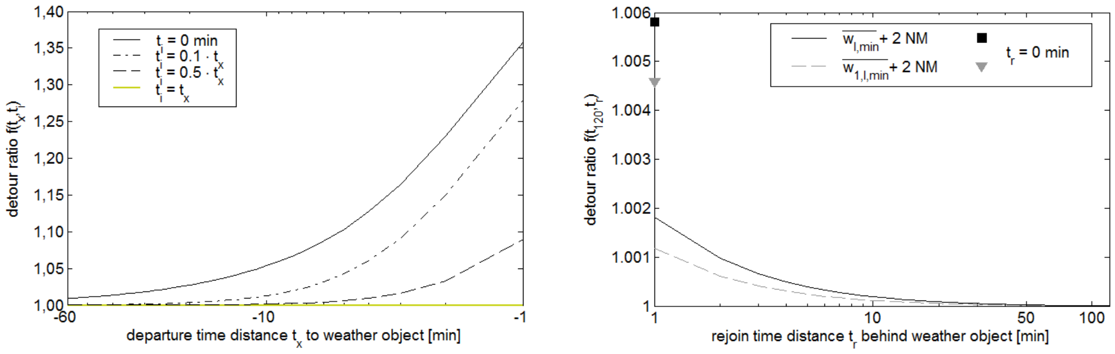

(a) Deviation delay detour effects.

(b) Return to route detour effects.

Figure 5.7: Additional relative detours due to (a) postponed deviation initiation and (b) preponed rejoin route manoeuvres. (a) Factor $f_1(t_x, t_i)$ for deviation around $\overline{w_{\mathrm{l,min}}}$ plus 2 NM safety distance as a function of start time t_x given on the logarithmic abscissa. Lines represent different deviation initiation distances $t_i = a \cdot t_x$ for $a^{-}0, 0.1, 0.5$ and 1. $a = 1$ describes the reference (green line) with instantaneous diversion. The black solid line represents the maximum deviation distance emerging from a flight to the object and along it ($a = 0$). Any possible additional detour due to a deviation delay is in the vertical range between green and black line for a certain departure flight time distance t_x. (b) Factor $f_0(t_{120}, t_r)$ representing the additional detour caused by a preponed return to the planned route relative to the direct to destination point B as a function of rejoin time distance t_r given on the logarithmic abscissa. The avoided lateral distance is $\overline{w_{\mathrm{l,min}}}$ and $\overline{w_{\mathrm{1,l,min}}}$, each plus 2 NM safety distance, given in black and grey, respectively. Markers indicate the maximum additional distance when directly returning to the route after the weather object ($r = 0$).

behind the weather object. Markers indicate the detour emerging from flying along the weather object back to the planned route. They give the maximum additional detour for avoided lateral distances $\overline{w_{\mathrm{l,min}}}$ and $\overline{w_{\mathrm{1,l,min}}}$, each plus 2 NM safety distance, given in black and grey, respectively, which equals to 0.46 % to 0.58 %. In comparison to the direct link to B an earlier rejoining of the planned route would lead to an elongation of less than 0.01 %.

With a configuration as chosen for this study, even these seemingly marginal additional detours caused by a delayed deviation or a preponed return to the route have an effect on the overall detour which has about the same magnitude. Thus, the choice made regarding the 2 hours flight time distance to destination point B was reasonable.

5.2.2 Analytic consideration with changing weather

So far, weather was considered as being static in the analytic formulation. However, in reality weather is dynamic and changes continuously. The trajectory is set up according to characteristics of the first observed stage of a cell. Still no movement of the cell is considered but its lateral extent may change. Nine conceivable options of the further cell development with respect to its lateral extent are given in Figure 5.8. The cell size may stay the same as in option 0 which was considered so far. Otherwise the left side extent, which is originally the smaller one, may change with the update at time t_{u} and either decreases (option 1) or increases (option 2) while being still smaller than the right side

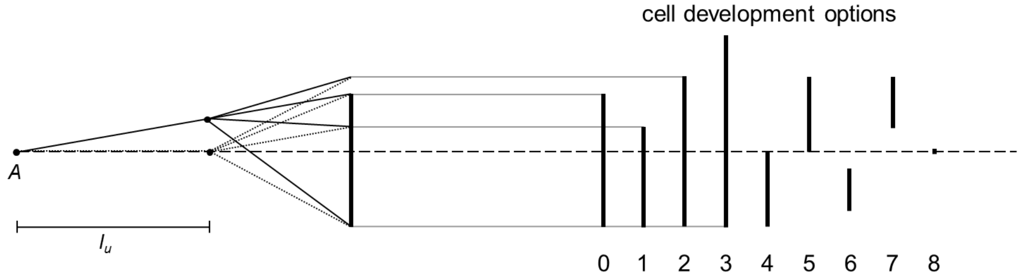

Figure 5.8: Cell development options (0-8) lateral to the movement direction to which the diversion route needs to be adapted after having flown distance l_u either on the planned or the previously determined diversion route.

extent. The route is adjusted to the new situation – starting from the current location on either the initial diversion route or the planned trajectory if the distance to initiate the deviation is reached. The left side extent may also exceed the extent right of the direct connection between current position and destination point B (option 3). In this case it might be beneficial to switch the deviation direction when having already initiated the deviation. The same holds for options 5 and 7 where the cell is only located left of the planned trajectory. If still on the latter route, either no or just small manoeuvres to the right of the flown direction are necessary. Options 4 and 6 represent a shift of the cell to the right with the same consequences as discussed before but with the opposite deviation direction. Finally, option 8 accounts for the cell dissipation. Any deviation and concomitant detours would not have been necessary.

Cell dissipation

With static weather instant deviation initiation is the most efficient strategy. Each delay in the reaction results in an additional detour as discussed in accordance with Figure 5.8. Now with dynamic weather, what if option 8 occurs and the cell disappears after a time t_u? If still on the planned trajectory, the aircraft can continue its flight without any diversion or detour. The detour caused by a premature deviation initiation followed by a cell dissipation within time t_x is further analysed according to the set-up given in Figure 5.9. At departure time t_0 a diversion route is calculated around the first observed stage of a cell. The aircraft moves with constant velocity $v = 250\,\mathrm{m\,s^{-1}}$ on this route until a

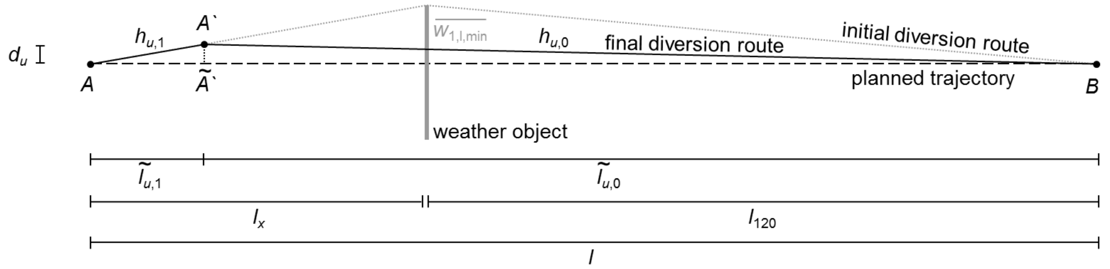

Figure 5.9: Geometrical set-up for route adaptation at position A' on the initial diversion route after cell dissipation at time t_u.

weather update at time t_u reveals dissipation of the cell. The already flown distance on the diversion route is

$$h_{u,1} = t_u \cdot 60\,\mathrm{s} \cdot 250\,\mathrm{m\,s^{-1}}. \tag{5.10}$$

In order to apply Pythagoras' theorem to calculate the length $h_{u,0}$ of the direct link between current position A' and destination point B some measures need to be determined. First, the actual lateral distance d_u to the planned trajectory ($\overline{A'\,\tilde{A}'}$) needs to be known. It can be derived from the intercept theorem which, applied to the chosen set-up, reads

$$\begin{aligned}
&\frac{d_u}{h_{u,1}} && = \frac{\overline{w_{1,\mathrm{l,min}}}}{h_1} && && \text{(5.11)}\\
\Longleftrightarrow\quad & d_u && = \frac{\overline{w_{1,\mathrm{l,min}}}}{h_1} \cdot h_{u,1} && \Big| \ \text{with} \quad h_1 = \sqrt{l_x^2 + \overline{w_{1,\mathrm{l,min}}}^2} && \text{(5.12)}\\
& && = \frac{\overline{w_{1,\mathrm{l,min}}}}{\sqrt{l_x^2 + \overline{w_{1,\mathrm{l,min}}}^2}} \cdot h_{u,1} && && \text{(5.13)}
\end{aligned}$$

Second, the remaining distance between projection point $\tilde{A}'$ and destination point B is required to be known. Thus, length $\tilde{l_u}$, which is slightly shorter than $h_{u,1}$, has to be determined. This can be achieved by applying the intercept theorem to the adjacent and opposite side of the right-angled triangle:

$$\begin{aligned}
&\frac{d_u}{\tilde{l}_{u,1}} && = \frac{\overline{w_{1,\mathrm{l,min}}}}{-l_x} && \text{(5.14)}\\
\Longleftrightarrow\quad & \tilde{l}_{u,1} && = \frac{-l_x}{\overline{w_{1,\mathrm{l,min}}}} \cdot d_u && \text{(5.15)}\\
& && = \frac{-l_x}{\overline{w_{1,\mathrm{l,min}}}} \cdot \frac{\overline{w_{1,\mathrm{l,min}}}}{\sqrt{l_x^2 + \overline{w_{1,\mathrm{l,min}}}^2}} \cdot h_{u,1} && \text{(5.16)}\\
& && = \frac{-l_x \cdot h_{u,1}}{\sqrt{l_x^2 + \overline{w_{1,\mathrm{l,min}}}^2}} && \text{(5.17)}
\end{aligned}$$

Hypotenuse $h_{u,0}$ is then determinable by

$$\begin{aligned}
h_{u,0} &= \sqrt{(-l_x - \tilde{l}_{u,1} + l_{120})^2 + d_u^2} && \text{(5.18)}\\
&= \sqrt{\left(-l_x - \frac{-l_x \cdot h_{u,1}}{\sqrt{l_x^2 + \overline{w_{1,\mathrm{l,min}}}^2}} + l_{120}\right)^2 + \left(\frac{\overline{w_{1,\mathrm{l,min}}} \cdot h_{u,1}}{\sqrt{l_x^2 + w_{1,\mathrm{l,min}}^2}}\right)^2} && \text{(5.19)}\\
&= \sqrt{\left(-l_x - \frac{-l_x \cdot h_{u,1}}{\sqrt{l_x^2 + \overline{w_{1,\mathrm{l,min}}}^2}} + l_{120}\right)^2 + \frac{(\overline{w_{1,\mathrm{l,min}}} \cdot h_{u,1})^2}{l_x^2 + \overline{w_{1,\mathrm{l,min}}}^2}} && \text{(5.20)}
\end{aligned}$$

The flown distance amounts to the sum of $h_{u,1}$ and $h_{u,0}$. The detour D_{dis} for routing with cell dissipation at time t_u follows from the flown minus the planned distance:

$$D_{\text{dis}}(t_u) = h_{u,1} + h_{u,0} - l \tag{5.21}$$

$$= h_{u,1} + \sqrt{\left(-l_x - \frac{-l_x \cdot h_{u,1}}{\sqrt{l_x^2 + \overline{w_{1,l,\min}}^2}} + l_{120}\right)^2 + \frac{(\overline{w_{1,l,\min}} \cdot h_{u,1})^2}{l_x^2 + \overline{w_{1,l,\min}}^2}} - (-l_x + l_{120}) \tag{5.22}$$

which is valid for $t_u \leq t_x$, or more precisely for $l_u \leq h_1$. The detour D_{dis} as a function of t_u and t_x normalised with the planned distance $l = -l_x + l_{120}$ is visualised above the dissipation time t_u added to the departure flight time distance t_x in Figure 5.10.

For some departure time distances t_x a coloured curve represents detours that are due to an increasing update time t_u. If the latter is zero (left end of the line), no deviation is initiated at all. The range up to $t_u = t_x$ (right ends of the lines) is presented there. Detours grow with the update time as the diversion is taken for a longer time and the lateral deviation from the planned trajectory increases for each respective curve. The maximum is reached shortly before the edge of the cell is approached ($t_u = t_x$). For each departure time distance t_x (now consider values on abscissa as t_x) the maximum normalised detour is given by the grey dashed line. It further rises up to 10^{-3} for one minute departure time distance (not shown). As in former diagrammes the normalised detour increases the shorter the planned route is, which is proportional to t_x.

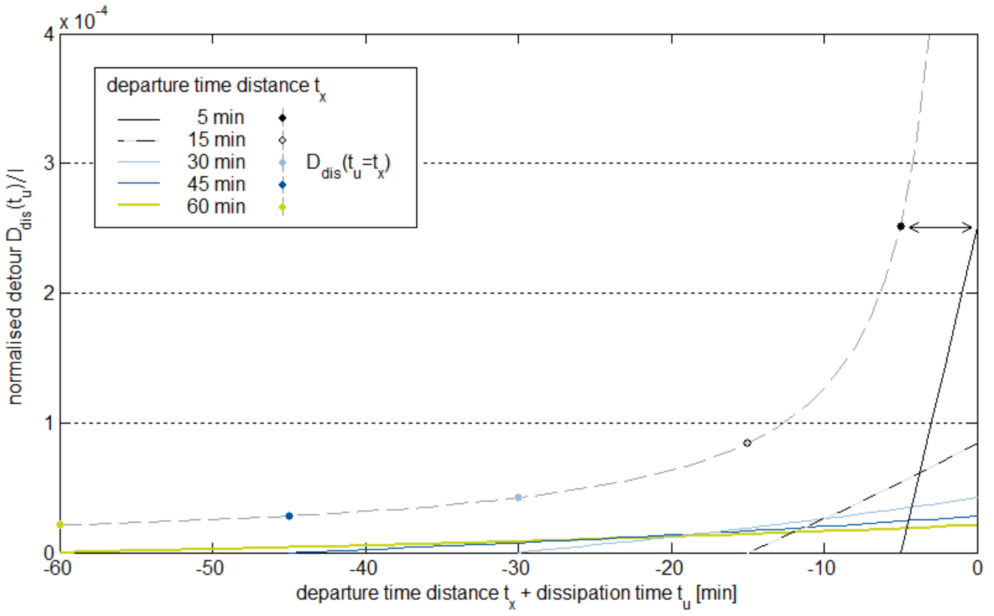

Figure 5.10: Normalised detours emerging due to cell dissipation and route optimisation at time t_u after departure in distances of 5, 15, 30, 45 and 60 flight minutes (colour-coded). The abscissa shows the negative departure time distance t_x minus update time t_u. The original diversion was instantly initiated at departure in flight time distance t_x to the weather object with lateral extent $w_{1,l,\min}$. The dashed grey line indicates the maximum normalised detour (on the very right) recognised for the respective t_x (indicated by the arrow for $t_x = 5$ minutes, consider values on abscissa now as t_x).

Cell shrinkage

Instead of complete dissipation as discussed before, the cell may just change its size. How would it need to change, that the *wait and see* strategy is beneficial? To what amount of the original size does it need to shrink on the deviation side for respective deviation initiation times t_i? Here it is assumed that the instant diversion route is not updated but remains the same even if the convective cell development would allow for an optimisation of the route.

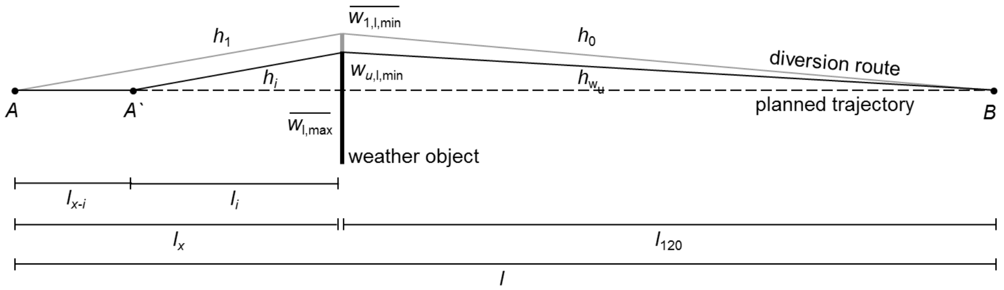

Figure 5.11: Geometrical set-up of the analysis of beneficial cell development at time $t_u = t_{x-i} = t_d$ in the *wait and see* scenario. An adaptation of the compared diversion route (grey line) instantly initiated at departure time t_0 is not considered.

The instant diversion route, given in grey in Figure 5.11 represents the reference for this case. Its length $h = h_1 + h_0$ can be determined according to Equation 5.5 with $t_i = 60$ and $\overline{w_{1,\text{min}}} = \overline{w_{1,1,\text{min}}}$.

Lengths h_i of routes with delayed diversion initiation are calculated with the same formula, but differing extents $w_{l,min}$ of the convective cell as well as varying deviation distances l_i.

As now the cell size is to determine at which the *wait and see* tactic becomes beneficial, both lengths need to be equated as follows

$$h = h_i \tag{5.23}$$

$$\sqrt{l_x^2 + \overline{w_{1,1,\text{min}}}^2} + \sqrt{l_{120}^2 + \overline{w_{1,1,\text{min}}}^2} = -(l_x - l_i) + \sqrt{l_i^2 + w_{u,1,\text{min}}^2} + \sqrt{l_i^2 + w_{u,1,\text{min}}^2} \tag{5.24}$$

In order to identify $w_{1,\text{min}}$, Equation 5.24 needs to be converted to this variable, which is analytically difficult. Instead, a graphical solution as shown in Figures 5.12 (a) and (b) is found numerically. There, coloured lines give the route length h_i as a function of $w_{l,min}$ which is iteratively decreased by factor s relative to the initial extent $\overline{w_{1,l,min}}$:

$$h_i(l_x, l_i, s) = -(l_x - l_i) + \sqrt{l_i^2 + s \cdot \overline{w_{1,1,\text{min}}}^2} + \sqrt{l_i^2 + s \cdot \overline{w_{1,1,\text{min}}}^2} \tag{5.25}$$

This relation – the absolute detour dependent on the cell shrinkage – is visualised in Figure 5.12(a). Differently coloured lines indicate absolute detours emerging from variable deviation initiation times t_i. For different departure time distances t_x the curves for the

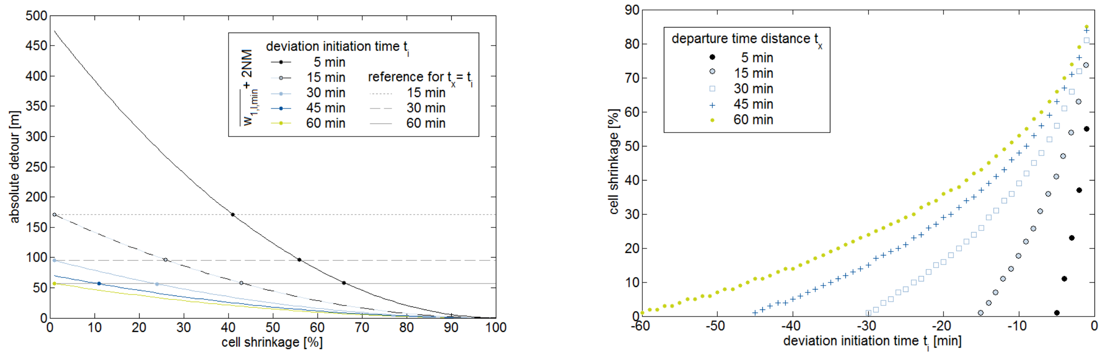

(a) Detours emerging from different cell sizes.

(b) Required cell shrinkages for a beneficial *wait and see* application.

Figure 5.12: (a) Absolute detours emerging in the *wait and see* scenario for different cell shrinkage strengths relative to the initial cell extent $\overline{w_{1,l,min}}$ given by solid curved lines that represent different deviation initiation times t_i. The reference detour for an instant deviation in departure distances of 15, 30 and 60 minutes is given by the horizontal grey lines. A beneficial cell size is reached when the coloured curve intersects the respective grey line and proceeds below the latter. (b) Required minimum cell shrinkages, independent of the original cell size, to obtain equal or less detour in the wait and see scenario with deviation initiation times t_i given on the abscissa. Different departure time distances are given in distinct colours and marker types.

same t_i are the same. What is different, is the reference detour due to instantaneous deviation at departure that is determined by t_x and given by grey horizontally lines for 15, 30 and 60 minutes in top-down order. Starting at the original cell extent on the very left of the diagramme (e. g. black line for $t_i = 5$ min) and increasing the cell shrinkage which decreases the cell size, let the detour for the respective deviation initiation scenario decrease as well. Once this line intersects a horizontal one (e. g. top, dotted line for $t_x = 15$ min), the cell shrinkage (41 %) can be read that would be minimally necessary in order not to be inefficient by postponing the deviation in the respective combination ($t_x = 15$ min, $t_i = 5$ min). Any stronger shrinkage of the cells would result in a benefit when applying this deviation initiation delay to the same departure distance. For larger departure distances, e. g. 30 and 60 minutes, the respective intersection needs to be considered and required shrinkages are read as 56 % and 66 %, respectively. Different cell extents lead to differing detours but from geometrical considerations the required cell shrinkage for the respective deviation initiation delay stays the same.

Finally, the numerical solution for factor s – the cell extent at which the *wait and see* scenario with the respective decision horizons becomes beneficial – is presented in Figure 5.12(b). The minimum cell shrinkage (1-s)·100 required to obtain a benefit (intersection points from Figure 5.12(a)) is given for any combination of t_x and t_i. The required shrinkage rises the later the deviation is initiated (to the right). As discussed before, it also increases with the departure distance.

Nevertheless, be aware, that this scenario is kind of simplified as the reference route is not adjusted to the new situation but stays as initially determined to avoid the original cell extent. In reality, the previous deviation route might be optimised equivalently to what was discussed in conjunction with dissipating cells and Figure 5.9, when a shrinkage of the conflicting cell is observed. Thus, the required decrease in cell size might even need to be stronger to obtain a benefit when applying the *wait and see* scenario.

The analytical assessment revealed that the detours to expect are small compared to the planned trajectory, which has a length of up to 2700 km. This is due to the relatively small lateral extent of the considered cell (6.8 km is the average extent of the smaller side of all cells, see Tab. A.1) that forces the deviation. Nevertheless, detour elongating effects due to a delay in the deviation initiation increases by about two magnitudes from an instantaneous deviation to a maximum delay and ranges around 1 % of the planned flight trajectory for parameters ($t_x = 60$ minutes and $t_i = 5$ minutes) relevant in the upcoming simulations. The effect of an earlier return to route was calculated to be even one order smaller. Reflections of possible cell developments showed that an early cell dissipation has only minor influence as the route can be adapted before a large detour is flown. Regarding shrinking cells that do not dissipate, the required shrinkage to obtain a beneficial routing while applying the *wait and see* tactic increases significantly up to 65 % ($t_x = 60$ minutes and $t_i = 5$ minutes) the longer the deviation is delayed.

After this analytical assessment on effects of some simple routing set-ups, the results obtained by Monte Carlo simulations will be presented. Compared to the just presented analysis with simplified weather characteristics, cell stages are dynamic. Not only that the extent of each cell changes, its location lateral to and in flight direction varies. Depending on the scenario, once a deviation route is in operation it adapts to the situation whenever new weather information is available and considered as such as will be detailed in the following Chapter.

6 Evaluation of simulation results

Monte Carlo simulations were run in order to evaluate the effect of different routing tactics clustered in three scenario blocks which were defined in Section 5.1. Based on the first observed stage of each cell and according to its movement direction a trajectory is defined on which the aircraft first follows and eventually outruns the weather object. Cell movement and, thus, flight direction are mainly eastward as can be seen in two exemplary simulation sets presented in Figure A.11 in the Appendix. All 563 cells and related flight trajectories of the *reference* and the *perfect nowcast* scenario are shown for a departure time distance t_x of 60 minutes.

The further discussion of results will focus on the three scenario blocks. First, the effect of a tactical delay in decision making when being limited to observational data is investigated. Simulation results obtained in the *wait and see* scenario are compared against such of an instant deviation – the *reference* scenario. Second, the effect of early re-routing based on the latest nowcast set issued before departure is evaluated with and without uncertainty consideration and in comparison with the *perfect nowcast* provided by observational data in retrospect. Third, detours are analysed emerging from trajectory adjustment to nowcast information that is steadily adapted to and updated with the observational product every 5 minutes. Again, simulations with and without consideration of the previously defined uncertainty measures are compared.

Objectives of stakeholders in aviation may differ significantly. While pilots aim to optimise their flight by flying efficiently, meaning to take the shortest possible route, the airline perspective might target to decrease the overall delay of all (airborne) flights. In a system-wide view and regarding the 4D trajectory concept, predictability, early re-routing and the maintenance of a stable and robust flow might be of high interest. This issue will be touched in the discussion provided in Section 6.2.

6.1 Effects of a delayed deviation decision – the *wait and see* scenario

Geometrical effects of a delayed deviation initiation around static weather were already assessed analytically in Section 5.2.1. Simulations show resulting detours (simulated minus planned trajectory length) caused by individual cell behaviour cycles to which the route is instantaneously adapted. Detours emerging in the *reference* scenario, in which the deviation is instantly initiated and further adapted according to the always current observation, are displayed in pareto-like descending order in Figure 6.1(a).

Due to the scenarios set-up with instantaneous deviation initiation at departure point A,

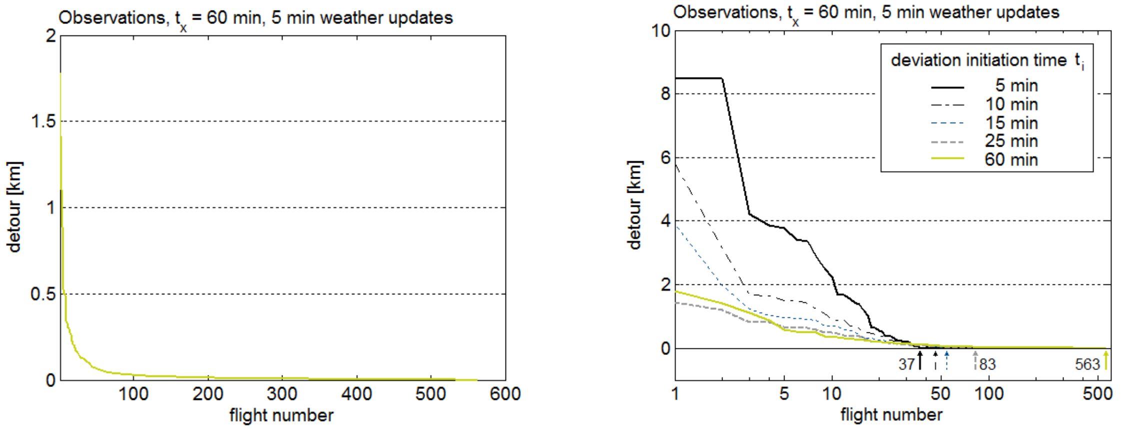

(a) Detours of *reference* scenario.

(b) Detours of *reference* and four sets of the *wait and see* scenario.

Figure 6.1: (a) Pareto-like visualisation of individual detours of all 563 simulated and deviated flights in the *reference* scenario with 60-minutes departure time distance t_x in descending order on linear axes. (b) Detours of four *wait and see* scenario simulations sets with deviation initiation distances of 5, 10, 15 and 25 flight minutes to the cell in comparison to the reference from (a) but now shown on a logarithmic abscissa. The later the deviation is initiation the less aircraft deviate and, thus, gather any detour which is indicated by arrows and numbers that give the first flight with no detour.

all 563 aircraft deviate from their individual planned trajectory. Only about 30 flights in the simulation gather relatively long detours of up to 1.8 km, whereas all other aircraft only flew marginal additional metres. This is caused by the limited lifetime of thunderstorm cells. After deviation initiation, the route is adapted to new weather information whenever this is available. If then the cell is not detected as a hazard by Rad-TRAM any more, no further consideration of the cell is necessary and the route is directed to destination point B along the great circle. As discussed in accordance with Figure 3.1 about half of all cells are detected by Rad-TRAM only three times (lifetime of 15 minutes). Thus, the majority of deviation routes can be directed towards their destination already after having flown on deviation routes for only 5, 10 or 15 minutes whereby they not yet gathered much detour in the chosen configuration. Finally, only 59 cells are still existing when the area of the potential conflict was reached. The number of cells that actually pose a risk at that time decreases to 32.

When delaying the deviation decision to a certain distance t_i to the cell, cells with lifetimes shorter than $t_x - t_i$ are already disappeared and no deviation is initiated. Thus, the overall number of deviations decreases as indicated in Figure 6.1(b). The green line in there is the same as in Figure 6.1(a) but on a logarithmic abscissa. The solid black line represents emerging detours in the other extreme, when delaying the deviation to a distance of 5 flight minutes to the thunderstorm cell. It features maximum detours of more than 8 km. Three other lines indicate resulting detours for intermediate delay times of 10, 15 and 25 minutes. Arrows in the lower part of the diagramme mark the first flight that does not show a detour – all former flights deviated. It becomes clear that, however, the number of deviations decreases, the flown detour gets larger the further the deviation is delayed.

The effects related to differently delayed deviation decisions are given in Figure 6.2. In there, characteristic values for each simulation set (563 trajectories) per deviation initiation time t_i are summarised. The amount of deviating aircraft, which was already given in Figure 6.1(b), is given by the black line which is related to the left ordinate. Starting at 100 % for instantaneous deviation initiation at departure ($t_i = t_x = 60\,\text{min}$) the curve is falling to a level of 6.4 % ($t_i = 5\,\text{min}$) which is equal to 36 flights. The green line (right ordinate) indicates the detour sum of all deviated flights in the respective simulation set. This curve is opposed to the former one. All 563 detours of the *reference* scenario are added up to 19.46 km (0.035 km per deviated flight, green filled circle). This is a far smaller sum than that accumulated by the 36 flights that only deviated in a flight time distance $t_i = 5$ minutes to the cell. These detours result in a sum of 58.78 km. Per deviated flight an average detour of 1.63 km was gathered. Compared to the analytical solution given in Figure 5.5, small discrepancies are recognisable which are due to the dynamic weather in the simulations. The mean detour of flights deviated in 60 minutes flight time distance is in the same order (decametres) but half as long as determined analytically. This is probably caused by the fact that a large number of aircraft do not need to complete the circumnavigation process as the weather disappeared in the meantime. In contrast to that, deviations initiated close to the cell result in detours that are twice as large ($\approx$ 1.5 km) as obtained in the analytical assessment. The geometrical detour-elongating effect of a delayed deviation is probably reinforced by the tendency of increased cell sizes, the maximum of which was found to be positively correlated with the cell lifetime (see Fig. A.4(b)).

The maximum individual detour per simulation set for t_i, given by a triangle, is also largest with 8.5 km for deviation initiation time t_i of 5 minutes. Box-and-whisker plots summarising the characteristics of the detours flown by deviated flights are given in Figure A.12 in the Appendix.

In order to evaluate the best time to decide whether and how to deviate and to initiate the diversion route, minima in the previously discussed measures in Figure 6.2 are determined and marked by red circles. From an airline perspective the overall detour of the fleet – the detour sum – should be minimised while occasional longer detours for individual aircraft are acceptable. In contrast to that, a pilot would try to avoid any detour and if inevitable like to keep it as short as possible. Thus, for pilot decisions the deviation initiation time t_i that features the minima in the mean and single maximum detour are those to orientate the flight tactic to. In the analysed data set only small negative signals can be identified at $t_i = 25\,\text{min}$ in an otherwise more or less homogeneous level of found detour sums and detour maxima for deviation initiation times larger than 20 minutes. The mean detour per flight is smallest for the earliest possible re-routing. However, a large number of deviations and associated detours were needless as the cell dissipated while being approached. Thus, many routes were optimised by direct headings towards

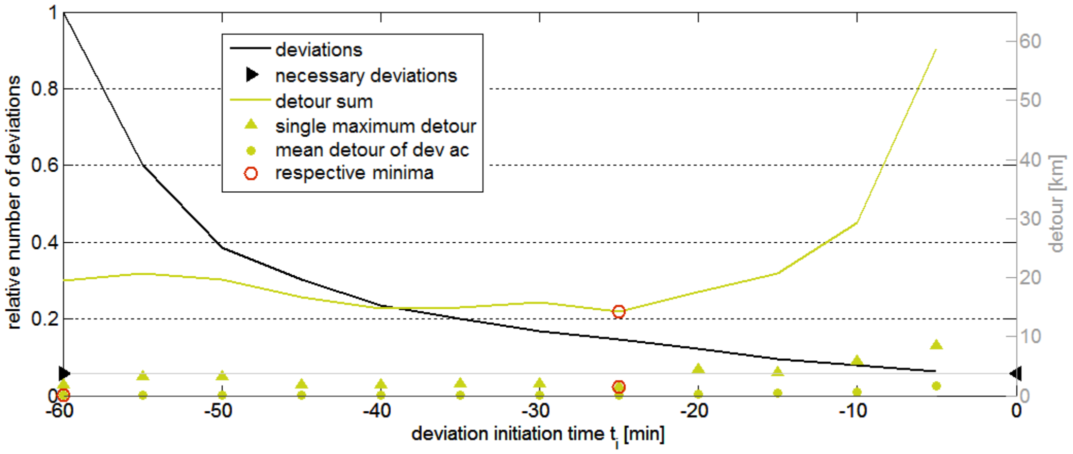

Figure 6.2: Deviation effects of the *reference* scenario (instantaneous deviation initiation at $t_i = t_x = 60$ minutes) and due to a delayed deviation decision in the *wait and see* scenario. The amount of deviating flights is given by the black line related to the left ordinate. Detour sum (green line), mean (circles) and individual maximum (triangles) are related to the right ordinate.

destination point B after the conflict resolved itself naturally. In a third perspective, given by ATC, communication should be kept to a minimum in order not to increase controller workload. However, an early deviation initiation would do so unnecessarily.

When delaying the deviation to 25 minutes flight time distance, the number of deviating aircraft can be dropped from 100 % (563 flights) to 14.5 % while keeping about the same level in the maximum individual detour as well as in the detour sum. The mean detour increases from 0.035 km to 0.15 km. Further delaying the deviation would not bring much benefit in the prevention of any deviation – the amount of deviating flights decreases to 6.4 % – but will lead to significantly longer detours for individual flights (up to 8.5 km compared to 1.5 km for $t_i = 25$ min) that sum up to much longer overall detours (58.8 km to 14.2 km, respectively).

It remains to be emphasised that, in case of short-living phenomena like thunderstorms, the decision what to do can be postponed to approach horizons in the order of the lifetime of the phenomenon. 25 minutes are recognised as the most efficient deviation initiation flight time distance. The same value was identified earlier as the average lifetime of cells but it is not as directly related as one might think spontaneously. In the discussed context of the scenario it rather means that cells which still force a deviation at 25 minutes flight time distance to the cell after being departed in 60 flight minutes distance, already exceeded their mean lifetime by 10 minutes; they already exist for 35 minutes. Nevertheless at this distance horizon individual detours as well as the integrated measure reveals an optimum. The majority of cells disappeared already and the remaining cells may tend to persist.

Interestingly, this seemingly beneficial decision horizon corresponds to the currently applied procedure. Weather avoidance is mostly based on the on-board radar information with, depending on its individual configuration chosen by the pilot, a maximum range of 200 NM (370 km) which covers a flight time distance of almost 25 minutes at a speed of 250 m s^{-1}. Simulations performed in a *limited view* scenario supplement the just discussed results of the *wait and see* scenario but are not explicitly discussed here. They slightly differ due to the fact that the initial deviation direction decision is based on partial knowledge about the conflicting cell.

6.1.1 Parameter study on the influence of departure time distance t_x

A parameter study is performed in order to evaluate whether the optimum decision horizon is dependent on the departure time distance t_x. For that, simulations were run for all combinations of t_i and t_x while accounting for $t_i \leq t_x$. The changing departure time distance t_x can be seen as a zero shift as indicated in Figure 6.3. Independent of the departure distance t_x one flight is set up to each of the 563 cells (most right point) that are at least observed once. Forcing a delayed deviation at flight time distance t_i to a cell is only possible by cells that survive the waiting time $t_x - t_i$. Thus, they need to have a lifetime of at least $t_x - t_i + 5$ minutes when assuming each observation being equivalent to 5 minutes cell lifetime. Points in Figure 6.3 give the number of cells that still exist after the least required lifetime $t_x + 5$ minutes which is given on the upper abscissa. The number of cells that actually pose a risk to the aircraft as they still overlap with the route and, thus, need to be avoided is given by triangles. When postponing the deviation initiation to 10 minutes ahead of the conflict after being departed in 30 or 60 minutes flight time distance to the cell, only cells with lifetimes of 25 and 55 minutes will still force a deviation, respectively. Searching for the related point to these lifetimes on the upper abscissa in Figure 6.3 enables to read the number of possibly initiated deviations which is equal to 179 and 74 for the respective departure distances. Thus, in correspondence with the lifetime of thunderstorm cells, especially the number of initiated deviations as well as that of necessary deviations will increase when focussing on one deviation initiation time t_i

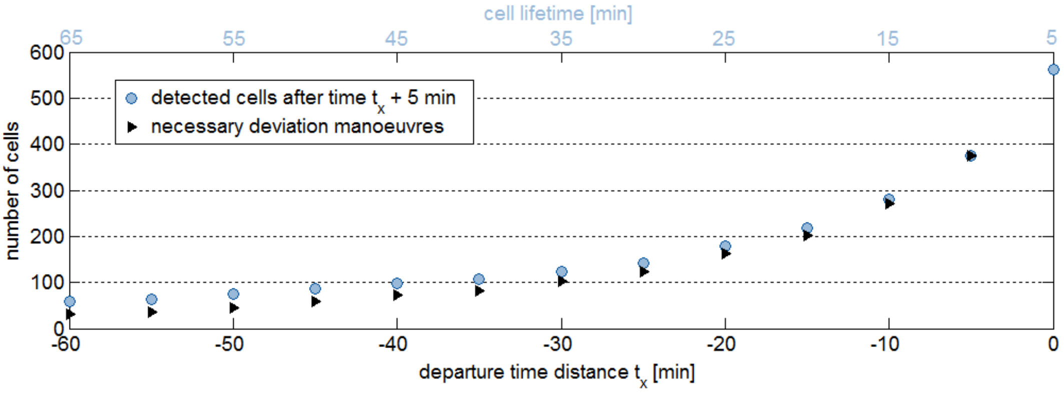

Figure 6.3: Number of actually relevant observed cells (points) for departures in flight time distance t_x given on the bottom abscissa. The required least lifetime of these cells is given on the upper abscissa. The number of respective necessary deviation manoeuvres is given by triangles.

while decreasing the departure time distance t_x. However, these numbers stay about the same but shift between the combinations of t_x and t_i.

These facts are visualised in the top panel of Figure 6.4. The black upper boundary of the green area gives the relative number of initiated deviations. It is equal to that presented in Figure 6.2. The coloured area indicates the amount of unnecessary deviations that are initiated for a certain t_i. The lower boundary marks the amount of required deviations for the respective departure time distance t_x. Further curves show the same measures for departure distances of 5, 15, 30 and 45 minutes. As the deviation initiation distance is maximally equal to the departure distance curves start at the respective position $t_i = t_x$ where all flights deviate instantly. Due to the lifetime characteristics of thunderstorm cells, the level of necessary deviation manoeuvres increases the closer the aircraft departs (see right side). Thus, less deviations are unnecessary as recognisable by the vertical spread between upper and lower area boundaries.

Of interest are then the resulting detours. The centre plot of Figure 6.4 presents detour sums while mean detours of deviated flights are given in the bottom panel. All results agree on the geometrically assessed increased elongation of detours the later the diversion is initiated. Apart from geometrical effects of postponed deviation initiation, here it is the number of deviated flights that increases the level of detour sums. The mean detour of deviated flights is about the same in all curves and only differs for deviation initiation times closer or equal to 15 minutes and eventually increases significantly for closer distances. The arrangement of curves is inverted before the latest possible deviation initiation so that the mean detour is larger the closer the aircraft departed (exceeding 2.5 km). However, the black point giving the mean detour for just departed flights shows the smallest value here and, thus, indicates that this might be due to the individual area life cycle of cells. Such a distribution of mean diameters together with the number of deviated flights results in a strong divergence of the detour sums (centre panel).

While the minimum mean detour of all t_x is found at $t_i = t_x$ (not shown), the respective minimum detour sum of each departure distance ($t_x = 5, 10, ..., 60$ min) is given by a red circle in the centre panel. By their arrangement they propose a *wait and see* tactic for departure or recognition distances longer that those covered in 30 minutes. Thus, this analysis confirms the previously identified decision horizon of about 25 flight minutes to optimise the system performance.

6.1.2 Transferability to new emerging cells

These results are, for instance, relevant regarding detours caused by new emerging cells. In the presented study only single cells were considered and the trajectory was set up according to the first detected stage of each cell. Neither multicell environments nor the emergence of new cells were investigated. In the latter case, the actual recognition distance to the new cell can be seen as the departure distance t_x. As follows from the just discussed Figure 6.4 the mean detour to expect is shortest when deviating instantaneously. However, postponing the decision to a flight time distance of 15 to 30 minutes

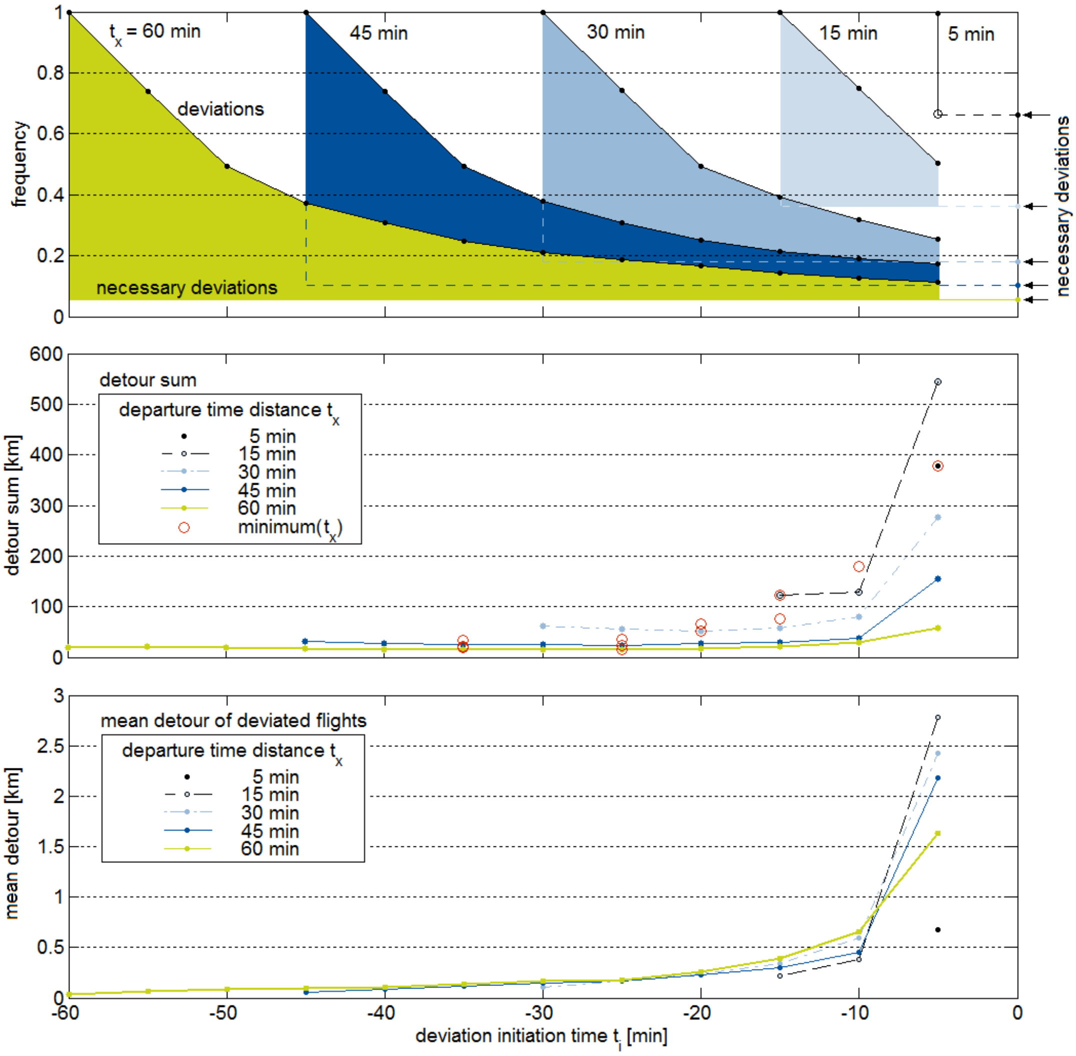

Figure 6.4: The effect of varied departure time distances t_x (= 5, 15, 30, 45 and 60 min) in the *wait and see* scenario. The top panel shows the relative numbers of initiated deviations (black curves), necessary deviations (coloured lines on the right) and resulting unnecessary deviations (coloured areas, vertical separation of upper and lower bound). Detour sums (lines) are given in the centre plot. Minima found for each departure time distances t_x are indicated by red circles. The mean detour of deviated fights is presented in the bottom panel.

might avoid unnecessary manoeuvres while not elongating the detour significantly. Only further delaying would do so.

What at all is the probability of encountering a new cell? A rough estimate can be made as follows. The analysis of Rad-TRAM data showed that on 15 July 2012 up to nine new cells (see Fig. A.3(a)) with the respective hazardous reflectivity of 37 dBZ were detected per radar scan. In their initial stage cell areas of the data set averaged to 100.4 km^2. About 20 other cells, each of which has a mean area of 192.3 km^2, already exist at that time and block some airspace where no new cells can emerge. Thus, available space for new cells in the Rad-TRAM domain, which mainly covers Germany with an area of 357340 km^2 (STATISTISCHE ÄMTER DES BUNDES UND DER LÄNDER 2015) minus the already blocked area of 20 cells which sums up to 3846 km is equal to about 353494 km^2. In there, up to 3520 idealised new cells could emerge separated from each other. When assuming cell generation as being randomly distributed and without any clustering effects, the probability to exactly meet one out of nine new cells is 9 to 3511. Now, that the question was with which probability a new cell poses a risk on the simulated route, the relevant area is much smaller. It can be assumed as the so called swath of the aircraft (e. g. 900 km flight distance for 60 minutes departure time distance) with width of the new cells mean diameter which is 10.7 km (see Tab. A.1). 95 new cells would fit into the swath which has an area of 9640 km^2. The probability that a new emerging cell is located in there is 2.7 %, that of at least one out of nine new cells per radar update rises to 21.85 %. It, however, is an idealised rough estimate.

A conflict caused by a new cell might require only small corrections of the route as that cell could be laterally displaced to the current trajectory, which might already be a diversion. Thus, the effects of closer recognition and decision horizons, as presented in Figure 6.4, only give an indication and are superimposed to the initial avoidance problem. In reality and depending on the on-board radar set-up, pilots may already monitor weaker, developing cells and create their own tactic for "what if" scenarios like the further strengthening of the cell.

6.2 Effects of re-routing according to departure nowcast sets

Trajectory planning is done days to hours before departure. As discussed in Chapter 2.5, the accuracy of thunderstorm forecasts is still only limited on such time horizons. Thus, an update of the route before departure is reasonable, especially in the future concept of 4D trajectories which is based on a committed reference business trajectory shared with all stakeholders before departure of a flight. Nowcast data such as from Rad-TRAM provide information on the cell development within a time horizon of one hour. According to the latest nowcast released before departure the planned trajectory of each aircraft can be instantaneously and proactively adapted to the expected situation which will probably be valid at time of approach. It is now assumed that no further update of the nowcast is provided to the pilot. Thus, no adaptation of the route is made, neither to new nowcast data nor to observational information. Instead, the initially determined diversion route is executed in the simulation (comparable to a blind flying) and the actual cell data is used to monitor potential conflicts and cell encounters. One of the latter is detected as such if the aircraft position is located within the weather object.

The number of flights that encountered an observed weather object in the simulations is given by bars related to the right ordinate in Figure 6.5. Lines, related to the scale on the left ordinate, give the detour sum of all 563 flights simulated for each departure time distance t_x and four modes. As the flight is re-routed at departure, no delay needs to be considered, so $t_i = t_x$. Green colour indicates the *perfect nowcast* scenario in which the later observed cell serves as the optimum guess of the cell development with the respective lead time. Cells with lifetimes shorter than $t_x + 5$ minutes are assumed to not pose a risk to the route and, thus, do not force any re-routing. As the frequency of cell lifetimes drops rapidly in the time frame of one hour, the number of re-routings, especially for large distances is limited. As a result, the overall detour added up over all flights is close to zero for 60 minutes departure time distances and increases slowly when departing closer to the cell. Only flights with departure time distances of 25 minutes or less accumulate detours of about 20 km and end up at 180 km for the closest departure in a distance of 5 flight minutes. For close departure distances the number of cell encounters in this *perfect nowcast* scenario attracts attention. In contrast to ones impression that a perfect nowcast would prevent any cell encounter, the chosen selection procedure does not fulfil the user needs with satisfaction. Whether a diversion is initiated or not is solely determined based on the fact if the considered cell still exists after time t_x and if this cell poses any risk to the planned trajectory. In case of no conflict with that specific cell, no diversion is calculated and the flight continues on the planned route even if earlier, not considered cell stages pose a risk that is not detected. Cell encounters may occur in cases where the cell dissipates at time t_x. Causing a conflict is then possible by the last observed cell stage and only if the related cell reaches above the gravity centre which was initially used for trajectory planning. Consequently, for a departure distance of 5 minutes all 175 cases in which the cell is only observed once automatically result in a cell encounter. Five additional encounters are detected on diversion routes. The selection procedure proposed in Section 4.3.5 would be better suited as it would account for the flight time distance to conflicting cells and, thus, would also consider earlier cell stages that are nearby and pose a risk. Diversions would have occurred more often and detours would sum up to larger values. However, due to its high computational effort, this procedure was not applied.

In reality a perfect nowcast is not available for trajectory planning. Instead nowcast data as such provided by Rad-TRAM can be consulted. Compared to the perfect nowcast data set where cells dissipated in the meantime, cell stages are always nowcasted for up to 60 minutes by Rad-TRAM. Thus, the distinct selection of the respective lead time, which is automatically set to t_x, forces a diversion in most cases. Only a lateral cell displacement off the route might prevent any deviation initiation. Simulations were run with nowcast

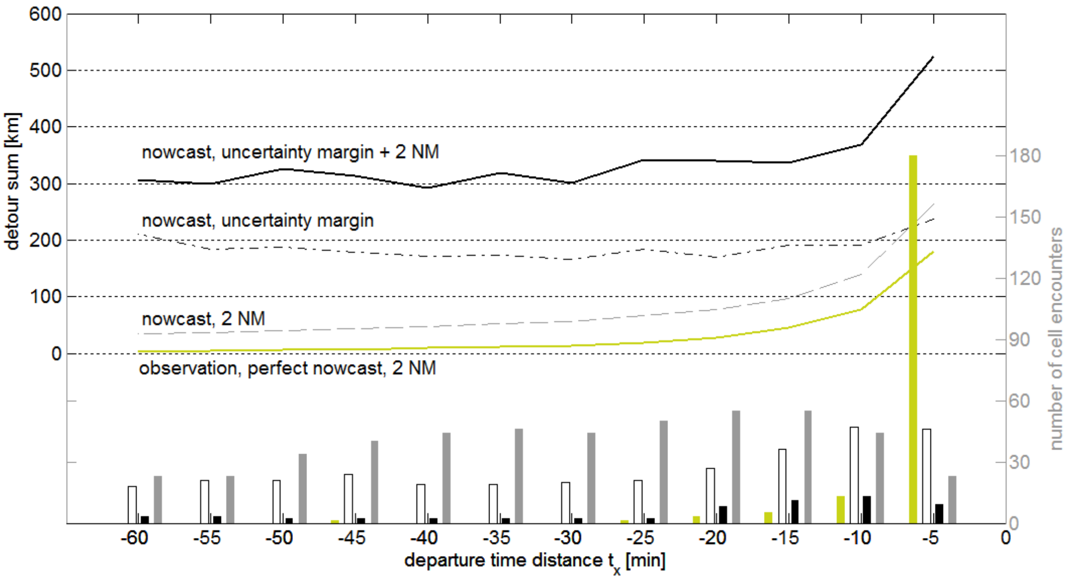

Figure 6.5: Detours (lines, left ordinate) and cell encounters (bars, right ordinate) obtained by 563 simulations per departure distance t_x between 5 and 60 minutes flight time. Instantaneous proactive re-routing is based on risk areas defined by the latest weather information released at departure time t_0 and valid at time t_x, either as *perfect nowcast* provided by observational data in retrospect or given by the nowcast, both with 2 NM safety distance in green and grey dashed, respectively. Additionally, when applying nowcast data the previously defined uncertainty can be considered, either purely (black solid line/bar) or with the safety distance on top (black, dashed-dotted line and white bar).

data enlarged by either the pure safety distance of 2 NM, the uncertainty margin defined in Section 3.5 or both, uncertainty margin plus safety distance. The related results are given in grey, solid black and dashed-dotted black/white lines and bars, respectively, in Figure 6.5. The added margin influences the deviation significantly. On the one hand the margin defines the lateral extent of the cell that should be avoided and, thus, the detour which will increase as has been seen in the analytical assessment and Figure 5.5 where the considered lateral extent differed by 2 km. On the other hand, the margin, especially if it is variable such as when accounting for uncertainty, might affect the deviation direction decision, as the ratio of areas left and right of the planned route might be shifted. As a result the diversion could lead along the opposite side and may significantly differ in length. A sample of four resulting routes to one cell cycle is shown in Figure A.10 in the Appendix.

The simulation results confirm these expectations. The detour is longer, the larger the margin is. According to Figure 3.7, the uncertainty margin is larger than 2 NM for all lead times except of the closest one for 5 minutes. This is why the dashed grey and the dashed-dotted black line intersect on the right side of the diagramme where the detour sum of the 2 NM case eventually exceeds that of the case with pure uncertainty consideration.

At the same time the number of cell encounters decreases (compare grey, white and black bars per departure time distance t_x) with an increasing margin. In the most cautious scenario, when accounting for uncertainty plus safety distance a maximum of 13 cell encounters is counted at $t_x = 60$ minutes. When avoiding airspaces defined by nowcast objects wrapped in the uncertainty margin, up to 47 cell encounters (8.3 % of 563 flights) are detected which is still in the remaining 10 % uncertainty range not covered in the applied uncertainty measure given by the 90^{th} percentiles of the distributions.

In comparison to the previously discussed scenario that accounts for a steady route adjustment to the actual situation, the resulting detour sums when applying nowcast seem not to bring any benefit. But this impression is misleading as almost all flights deviate in this *departure nowcast* scenario. Individual detours provided in box-and-whisker plots in Figure A.13 in the Appendix are better suited for comparison.

Colour-coded as in Figure 6.5, black box plots represent the most cautious scenario which indicates longest individual detours arranged around 500 to 700 m with maxima, first, increasing slightly between 1.1 to 1.3 km when departing in descending distances up to 15 minutes and, then, rising up to above 2.8 km for closer distances. Detours emerging from scenarios where either the uncertainty or the safety margin is applied level around 0.3 and 0.1 km per flight, respectively. All these detours are at least half as small as those obtained with a steady adjustment to actual data which are presented directly above in Figure A.13.

It should be kept in mind that individual detours increase with the cell extent which was manipulated in this study by adding different distances to nowcasted cell contours. A consideration of the nowcast uncertainty in addition to the safety distance results in detours that are four times as large as those emerging when cells are avoided while only accounting for 2 NM safety distance. This factor strongly depends on cells sizes. In this study, cells were rather small and the uncertainty distance added to cells with large lead times is in the same order as the cells extent itself. Thus, the cell size is significantly manipulated which has an effect on detours as just described. Imagine however, enlarging larger structures will not have such a strong influence, at least as long as no clustering effects occur that block gaps to fly through and force even larger detours. Due to the chosen set-up, such effects are not considered here.

Rather it should by considered that nowcasts used in the *departure nowcast* scenarios are all based on the initial stage of the respective cell according to which the trajectory is planned. However, in reality, the same procedure might of course be applied to cells and structures that are already further developed. Related nowcast cells might probably be a bit larger compared to those from the first nowcast set which is typically a bit subdued.

In an operational application of nowcast data only provided once at departure, the consideration of uncertainty need to be weighed. It might facilitate predictability regarding safe trajectories which would be necessary in the concept of 4D trajectories. However, when being limited to the Rad-TRAM product, this scenario only enables to account for cells that exist already at departure time. Applying an uncertainty margin decreases the risk of cell encounters but at the penalty of inefficiency caused by large detours and related costs for fuel and delay recovery when generally using the same tactic for the whole fleet. A large number of diversions would be completely unnecessary as nowcasted cells disappear while being approached. Thus, the uncertainty introduced by the lifetime of cells might even be more relevant than initially expected. Nowcasts provided by Rad-TRAM in its current state, however, do not give an information on this issue.

The creation of blocking structures in multistorm environments, which result from enlarged individual cells that overlap, force large diversions and, thus, even increase the penalty. In contrast to that, new emerging cells are not at all covered in the re-routing and may still force a tactical adjustment of the route. Thus, prioritisation of the parameter to optimise resides with decision makers: if predictability is prioritised, an application of uncertainty measures could be beneficial, in terms of system efficiency a proactive consideration on smaller time horizons or a steady adaptation to updated information is rather target-aimed.

6.3 Effects of a steady route adjustment to nowcast updates

If now data-link techniques are available to steadily provide nowcast updates to the cockpit, a continuous adjustment of the route can be done. While approaching the scene the lead time to account for decreases from update to update and, thus, the nowcast becomes more certain. Again, different avoidance distances can be applied. The resulting effects on the overall detour are given by lines in the lower part of Figure 6.6. The green line is the reference here. It represents detour sums emerging from a steady route adjustment at 5-minutes update rates of observational data enlarged by the safety distance of 2 NM, as discussed in Section 6.1, while initiating the deviation in flight time distance t_i given on the abscissa. The bold solid black line indicates detours from the most cautious scenario in which uncertainty plus safety distance is accounted for. The dashed dotted black line, as well as the grey dashed one represent detours from nowcast cell circumnavigation while considering either the pure uncertainty margin or the safety distance, respectively. Due to its positive correlation with the lead time, the uncertainty margin significantly increases the overall detour when initiating the deviation early and accounting for large lead times (both black curves on left side of diagramme). When only applying the safety distance to nowcast cells about the same detours emerge that are found for observational data. The number of deviated flights (top section) is more or less the same in all four cases as either the cell and associated nowcasts still exist when having reached the initiation distance t_i or they already dissipated what prevent unnecessary deviations. Slight differences may be caused by a lateral shift in the nowcast which, even if it is enlarged, might not pose a risk to the trajectory. However, the resulting mean detours (sum divided by deviated flights, not shown) are highest for the largest avoidance distance. Maximum single detours, given by triangles in the bottom section of the figure, show a trend to longer individual detours when delaying the decision. A sequencing in the arrangement of scenarios, however, is not obvious. The detour minima of all four simulation sets are not explicitly marked but arise for deviations initiated 25 or 30 flight minutes ahead of

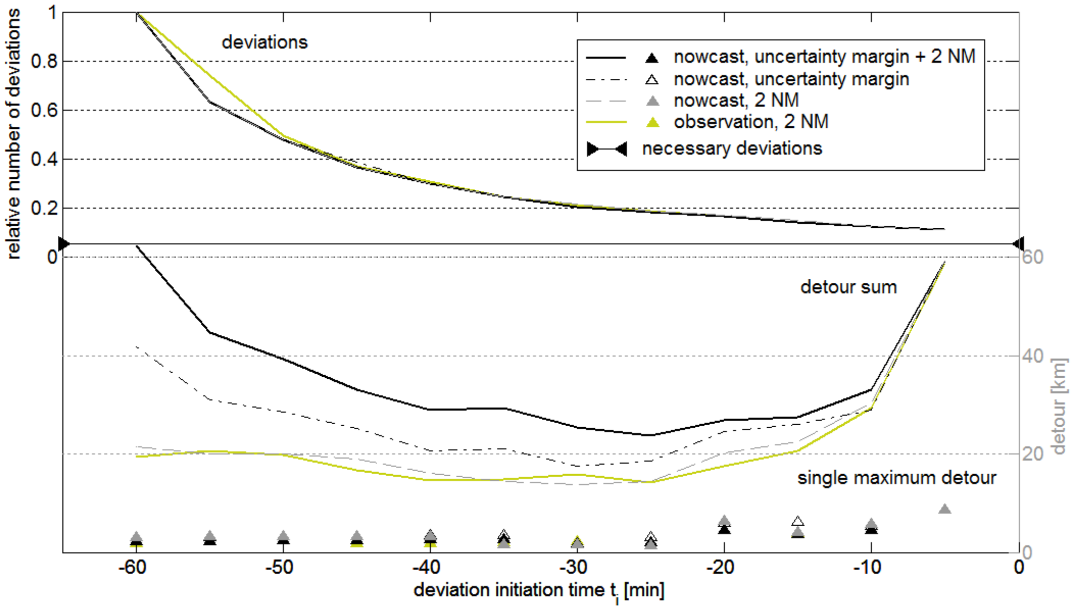

Figure 6.6: Elongation of the accumulated detour (lines in lower section) emerging from uncertainty consideration in the *nowcast update* scenario for departure time distance $t_x = 60$ minutes and differently delayed deviation initiations. Solid black and dashed-dotted black lines represent the uncertainty consideration with and without the safety distance of 2 NM, respectively. Detour sums given by the grey dashed line are caused by nowcast cell avoidance while only accounting for the safety distance. Colour-coded as such lines, triangles indicate the maximum individually flown detour. The relative number of deviating flights is given by lines in the upper section of the diagramme.

the cell. Still at that time and even clearer for larger deviation initiation distances is the detour-elongating effect of the uncertainty margin. Thus, when allowing for route adjustments anyhow, it is more efficient not to include the nowcast uncertainty. Steady updates reduce that uncertainty and enable to finally avoid a nowcasted cell for a lead time of 5 minutes of which the applied 90th percentile uncertainty measure is already smaller than the safety distance.

7 Summary and conclusion

Thunderstorms incorporate several meteorological phenomena that pose risks to aviation. Thus, international regulations strongly recommend to avoid such convective cells and even to hold a safety distance to certain reflectivity thresholds. Due to a lack of appropriate data provision in the cockpit, thunderstorm avoidance is still based on the on-board radar display that informs about the actual distribution of precipitation droplets in the atmosphere ahead of the aircraft. The scanned range of maximally 200 NM covers a flight time of about 25 minutes which at the same time represents the possible decision horizon available between first detection at the far end of the display and its approach. While being approached the cell develops, it may shrink or grow and could be displaced. Data-link techniques are in principle available to uplink comprehensive data such as radar or satellite products. These could elongate the decision horizon and increase the situational awareness of pilots by presenting the meteorological situation all around the aircraft and ahead of the on-board radar.

In the same manner nowcast data can be provided in order to supplement the general current situational information by such of the probable future state and the development of individual cells that need to be accounted for. However, due to the chaotic behaviour of thunderstorm cells, especially in the initial phase but also in their internal development, still nowcasts feature some uncertainty. A methodology is proposed how to quantify the remaining uncertainty which is defined, in this thesis, as any spatial difference between the best guess provided by the nowcast and the actual later observed cell. Deviations of the maximum extent in four directions relative to the observed cell movement are determined following the motivational question how to modify the nowcasted cell that it covers the later observation. Direction- and lead time-dependent uncertainty measures, such as the 90th percentile of distributions of the found deviations, can be derived. Analysing thunderstorm nowcast data of a whole year or an even longer period should enable to identify characteristic uncertainty measures for differing synoptic situations. The respective set of measures is thought to be universally valid for the synoptic situation and can be applied to future nowcast releases. Nowcasted cell contours for a certain lead time are enlarged by the related 90th percentiles to define an uncertainty polygon which, when being avoided, reduces the risk of cell encounters to e. g. 10 %.

A one-day Rad-TRAM data set was exemplary analysed. The direction- and lead time-dependent uncertainty measures were quantified. Deviations right of and against the movement directions exceed those in the remaining directions by up to about 2 km for all lead times. The BACKWARD 90th percentiles start at 3.78 km for 5-minutes and reaches up to 21.17 km for 60-minutes nowcast horizons. The application of these measures to nowcasted cells enlarges the latter by a factor of about 16 on average. Information on the emergence of new cells as well as cell dissipation, both meant as the exceedance or shortrun of certain reflectivity thresholds (e. g. 37 dBZ), is not provided in the Rad-TRAM nowcast. Thus, the uncertainty introduced this way is not included in the analysis.

The automatic consideration of Rad-TRAM data and their respective uncertainty was implemented in the adverse weather diversion model DIVMET. It enables to perform Monte Carlo simulations in order to evaluate different routing tactics when having differing weather information on hand. A couple of scenarios are defined that differ in the decision making and deviation initiation distance to the cell and either use observational or nowcast data, the latter with or without uncertainty consideration. From geometrical considerations of a static situation an instantaneous re-routing results in the shortest diversion. In a dynamic field of thunderstorm cells with individual life cycles the optimum tactic might be different. Thus, 563 simulations, one for each cell cycle of the analysed day, were run per scenario and each parameter combination of departure and deviation initiation distance to the initial cell, both varied in 5-minutes increments between 5- and 60-minutes flight time.

When being limited to observational data updated every 5 minutes, a *wait and see* tactic turned out to be most efficient when recognising the potential conflict in a flight time distance of more than 15 minutes. A postponed deviation enables to reduce the number of manoeuvres significantly as many thunderstorm cells dissipate. Optimum deviation initiation distances obtained from detour sums are shown in Figure 7.1 and range between 20 and 35 minutes flight time. For closer cell recognition an instantaneous deviation is advisable.

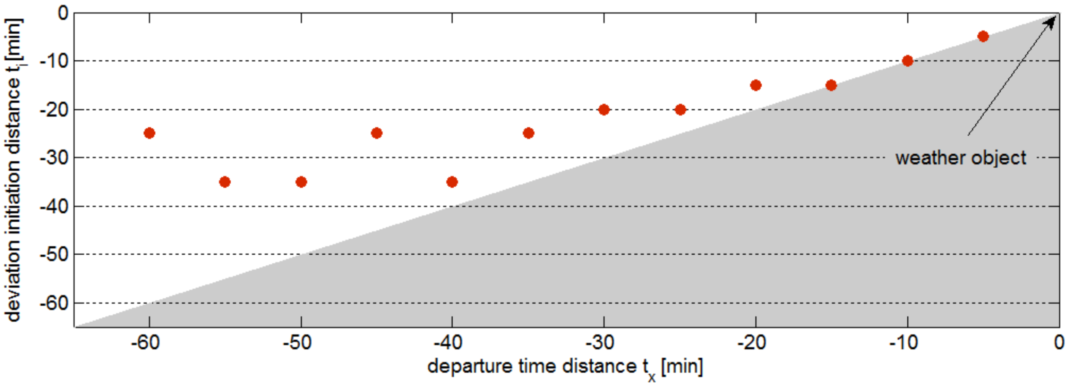

Figure 7.1: Optimum deviation initiation time distance t_i per departure time distance t_x. The grey section marks impossible solutions. An instantaneous deviation initiation would be located along the diagonal boundary.

If nowcast data is available at departure, a proactive re-routing can be applied, which would be a conceivable scenario in the context of 4D trajectories. Simulations are run in kind of blind flying on the proactively determined diversion route without any adaptation to the actual situation. However, cell encounters are monitored for evaluation purposes. Consideration of the found uncertainty measures is worth in order to predict safe routes and ensure cell encounters to occur in less than 10 %. This, however, has its price – the additional extent of the cell elongates the detour significantly. However, compared to the adaptation to observational data, even the longest identified detours in the proactive routing are still half as small. The nowcast uncertainty introduced by errors in cell size and location can be mitigated by the proposed methodology. However, the uncertainty of cell lifetime turned out to be even more relevant. Rad-TRAM in its current state does not nowcast cell dissipation but provides a prediction for the whole 60-minutes time horizon for all cells – including those (about 50 %) which disappear after less than 15 minutes. When applying this data in avoidance routing all cells are considered as being still existent when they would be approached and, thus, all aircraft are re-routed what results in a long overall detour in the system and should be avoided from an airline perspective. Furthermore, as new cell emergence is not yet nowcasted, additional short-term deviations might become necessary. Thus, whether or not it is worth to accept the cost of increased predictability by accounting for nowcast uncertainty while still taking the risk of short-term re-planning either due to conflicts in the remaining 10 % uncertainty range or because of new emerging cells resides with decision makers.

If data-link techniques allow for nowcast data updates in the cockpit to which the route can be adapted continuously, uncertainty does not need to be considered as it just leads to unnecessary detours.

The performed simulations were subject to certain restrictions. Further studies should investigate other geometrical combinations than the chosen one where aircraft and cell move in the same direction. Furthermore, the limitation to one single cell per simulation should be removed. This set-up was simple but sufficient to show the effect of different tactics, however, deviations around or through a field of several cells might be superimposed and clustering effects, especially when accounting for the uncertainty margin, may significantly elongate detours. In the special case of a squall line efficiency is the minor target, pilots rather aiming to find a gap to fly through anyway. Situations like these can be investigated with DIVMET but were out of the scope of this thesis.

Nowcasts provided by the current state of Rad-TRAM account for individual cell behaviour and extrapolate the trend within one nowcast set (12 lead times) but do not include a typical cell life cycle or even predict cell dissipation. These features, as well as an advanced warning of cells that are close to and probably exceed the applied threshold would bring valuable advantages for proactive aircraft routing. Marking related cells of a merging or splitting process would additionally enable to appropriately account for these processes in the uncertainty determination.

A comprehensive uncertainty analysis should then include thunderstorm nowcast data of at least one year – a sufficiently large data set – in order to identify the product-specific dependencies on the synoptic situation and to derive a set of general measures which can be applied to a newly released nowcast. A suitable methodology to determine the uncertainty introduced by new emerging and dissipating cells remains to be developed.

A coupling with advanced models, such as Cb-LIKE, that enable seemless prediction by linked nowcast technologies and NWP or even EPS may help in this issue.

The presented study focussed on adverse weather for which thunderstorms were selected as being representative. The proposed methodologies, however, are not limited to this meteorological phenomenon. Turbulence, icing as well as volcanic ash are other conditions that typically occur in continuous areas that are hazardous at least for certain uncertified aircraft and, thus, are often avoided by those. Although, the scales in time and space of these phenomena differ strongly from such of thunderstorms, the respective forecast uncertainty can be determined equivalently in the horizontal dimension. In contrast to thunderstorms, however, the vertical extent of volcanic ash clouds or icing areas is much smaller, as they are mostly structured in layers. Thus, an avoidance can also be achieved by flight level changes. If, however, the hazard should be avoided laterally, the strong relation to the lifetime of the phenomenon as identified for thunderstorms should be of minor relevance as these phenomena last longer. As a result, routing is thought to be most efficient the earlier the deviation is initiated in such meteorological situations.

To conclude, the proposed new methodologies of spatial uncertainty determination feature a wide-range utility – not only to thunderstorm nowcasts but in general for forecasts of areally occurring phenomena. The suggested application of found measures to the nowcast data itself allows for a precise consideration of product-specific features in weather avoidance routing. It enables to mitigate risks introduced by nowcast uncertainty and, thus, facilitates predictability. The uncertainty analysis performed with a sample data set provided by Rad-TRAM gives a first estimation of the magnitude of nowcast errors which still need to be confirmed in a comprehensive analysis. Results obtained by Monte Carlo simulations reveal the detour effect of various routing tactics and may function as a point of reference for decision makers.

A Appendix

A.1 Nowcast data set description – complementary material

Synoptic situation of 15 July 2012

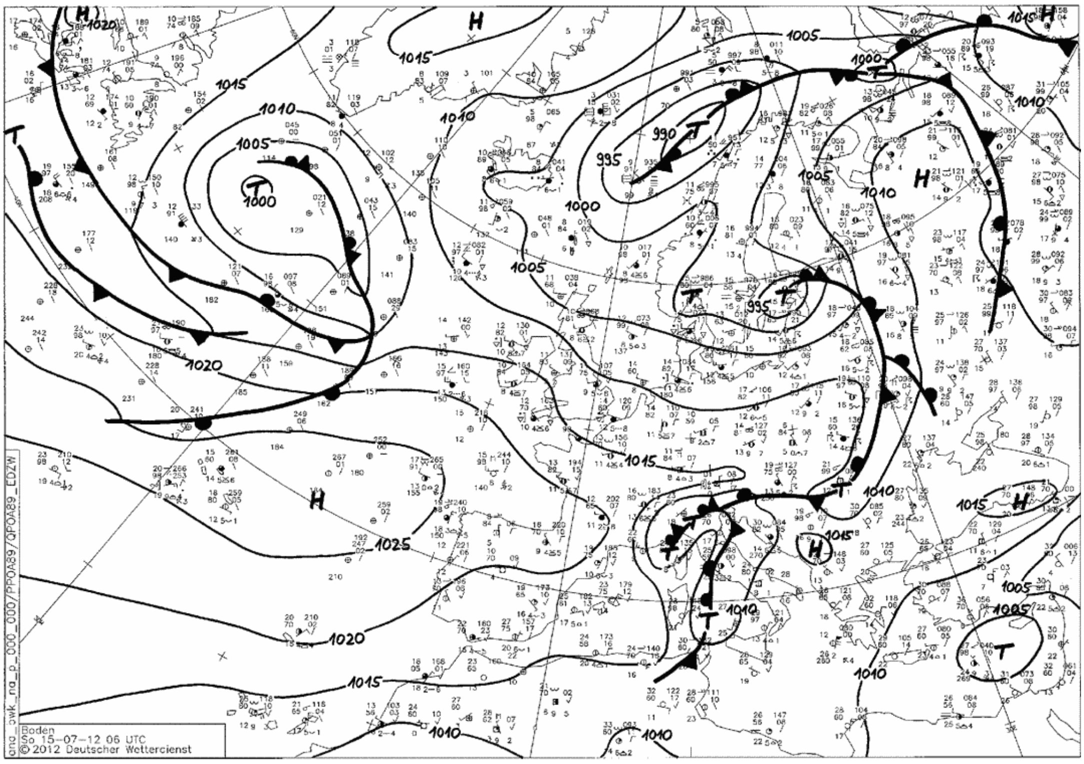

Figure A.1: Weather map showing surface pressure and fronts at 06:00 UTC on 15 July 2012.

Cell characteristics on 15 July 2012

Cell movement

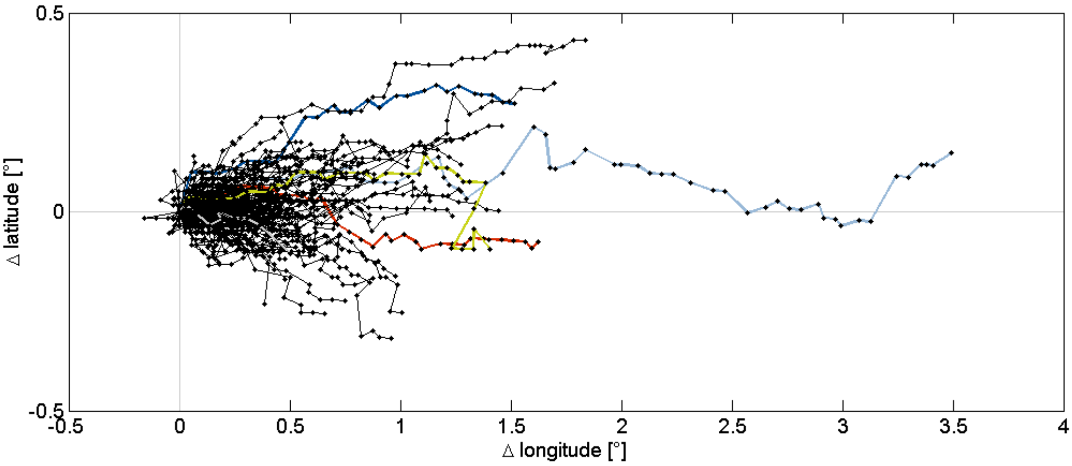

Figure A.2: Gravity centre tracks of each of the 563 cell cycles with the respective start point set to [0,0]. The time step is 5 minutes. Cell movement is mainly oriented eastward. The cell with the longest lifetime travelled about 3.5° in this direction. The observed lateral movement is limited to less than 0.5°. Five tracks are exemplary highlighted.

Cell detection and lifetimes in the course of the day

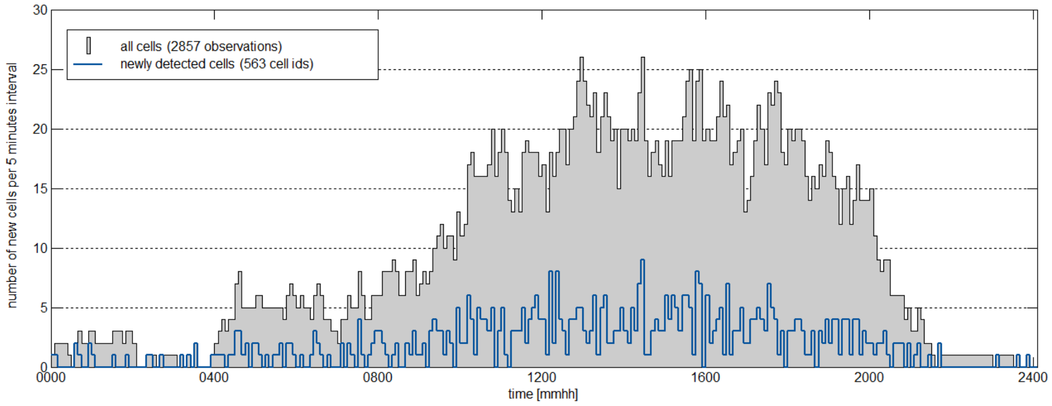

(a) Number of (newly) detected cells per radar scan.

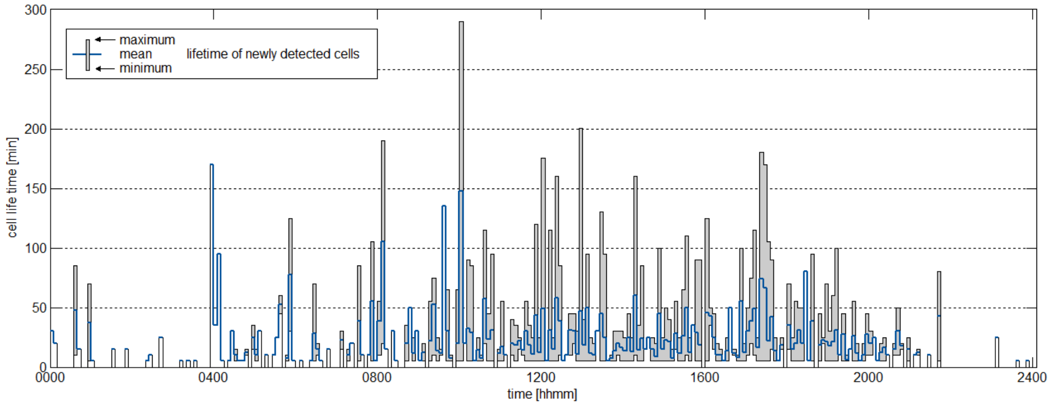

(b) Minimum, mean and maximum lifetime of newly detected cells.

Figure A.3: Rad-TRAM cell characteristics of 15 July 2012: (a) Total number of all (black line/grey area) and newly (blue line) detected cells per nowcast run which is performed every 5 minutes. (b) Range of lifetimes (grey) and mean lifetime (blue) of newly detected cells per run.

Cell size analysis

Cell area

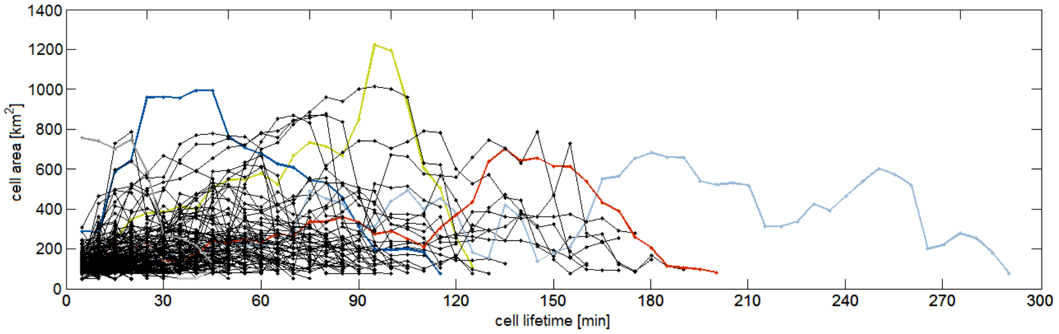

(a) Cell area cycles.

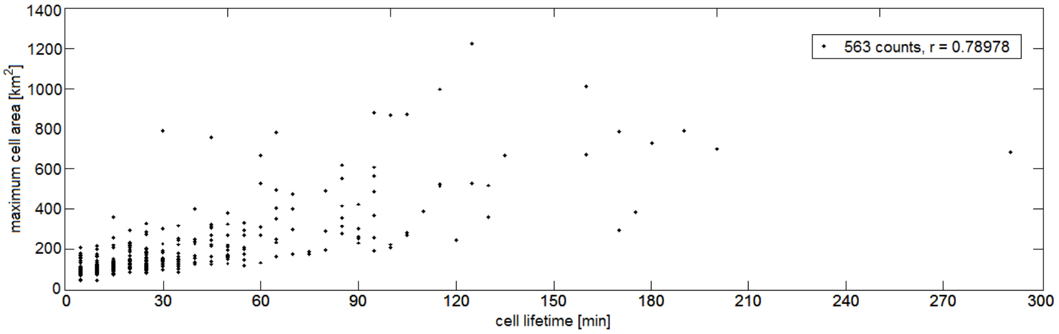

(b) Scatter plot of maximum cell area against cell lifetime.

Figure A.4: (a) Area size cycles of all cells of 15 July 2012 given as a function of the lifetime. Some random cycles are highlighted (not necessarily the same as in Fig. A.2). (b) Scatter plot of maximum cell area against cell lifetime indicating a positive correlation of both.

Cell extent per direction

Table A.1: Mean extent in metres of all and only first observation stages of convective cells provided by Rad-TRAM on 15 July 2012. For minimum and maximum extents always the smaller or larger, respectively, extent of two opposing sides is considered.

	extent [m]			
	FORWARD	BACKWARD	LEFT	RIGHT
all cells	8736.9	6957.1	8454.4	6818.0
minimum	6926.4		6783.6	
maximum	8767.6		8488.8	
first obs of each cell	6271.6	4734.2	6128.9	4582.5
minimum	4722.5		4568.3	
maximum	6283.4		6143.1	

A.2 Nowcast uncertainty analysis – complementary material

Number of comparisons

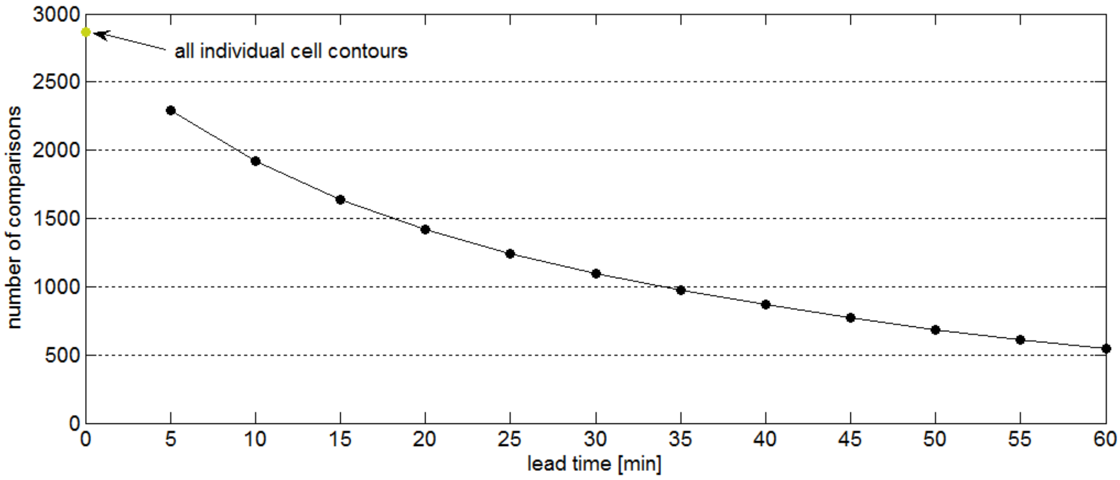

Figure A.5: Number of detected cells (green) and such of comparable objects per lead time (black points). The latter numbers are strongly related to the lifetime of thunderstorm cells. While there are many cells with short lifetimes that can be related to former nowcasts with small lead times, the number of cells exceeding a lifetime of 60 minutes (at least 65 minutes are required to match a 60 minutes nowcast) is small. Thus, the number of found matchable pairs of nowcast and observation decreases from 2294 for 5-minutes lead time to 548 for the maximum lead time of 60 minutes. The difference between 0 and 5 minutes lead time is equal to the number of identified cell cycles and is due to their first time detection for which no previously issued and related nowcast is available.

Development of distribution characteristics with lead time

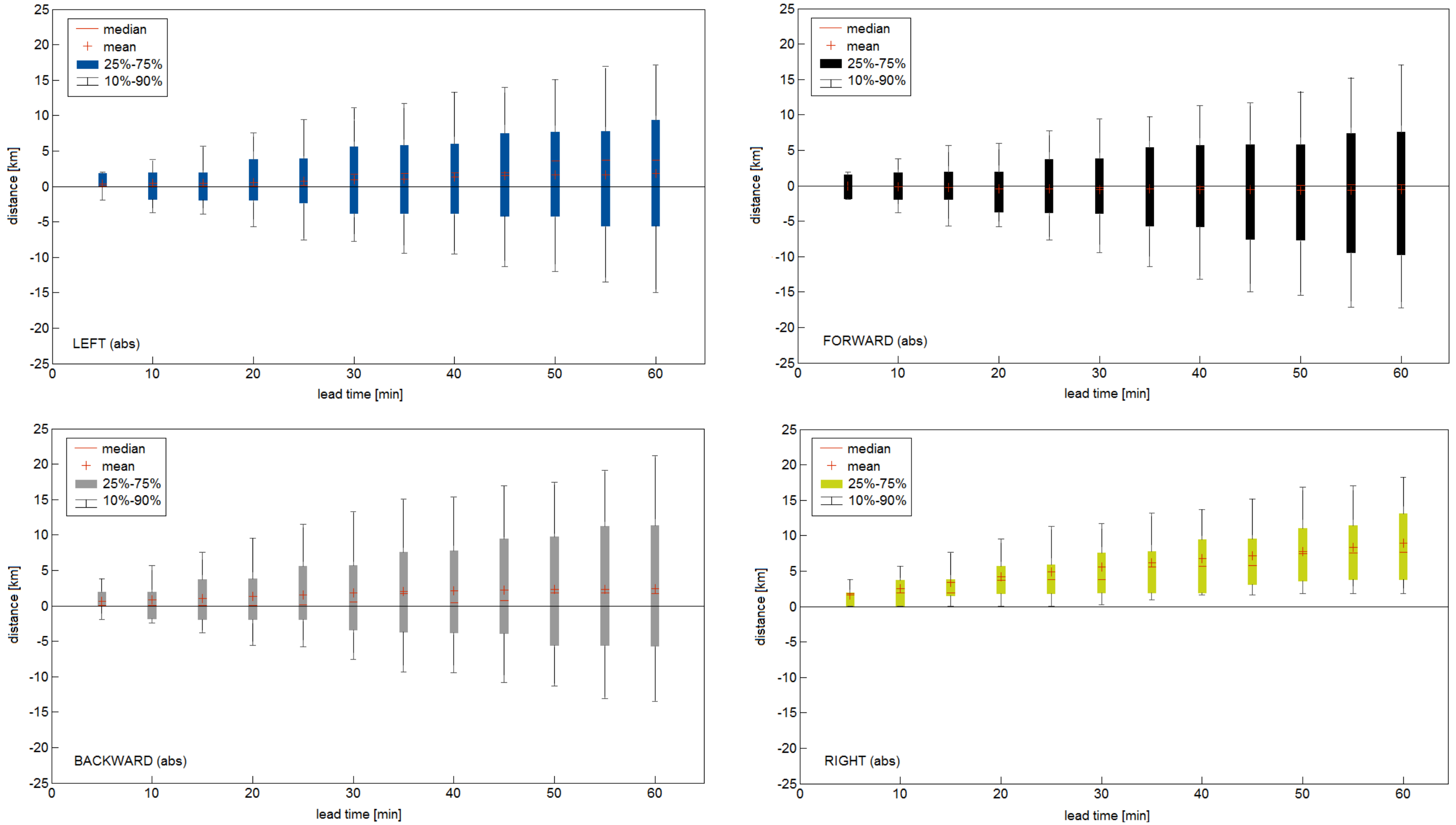

Figure A.6: Box-and-whisker plots summarising the development of mean (red cross) and median (red line), the interquartile range (coloured box) as well as the 10th and 90th (whiskers) percentiles of distributions found for absolute deviations in direction LEFT (top left), FORWARD (top right), BACKWARD (bottom left) and RIGHT (bottom right).

Absolute lateral uncertainty

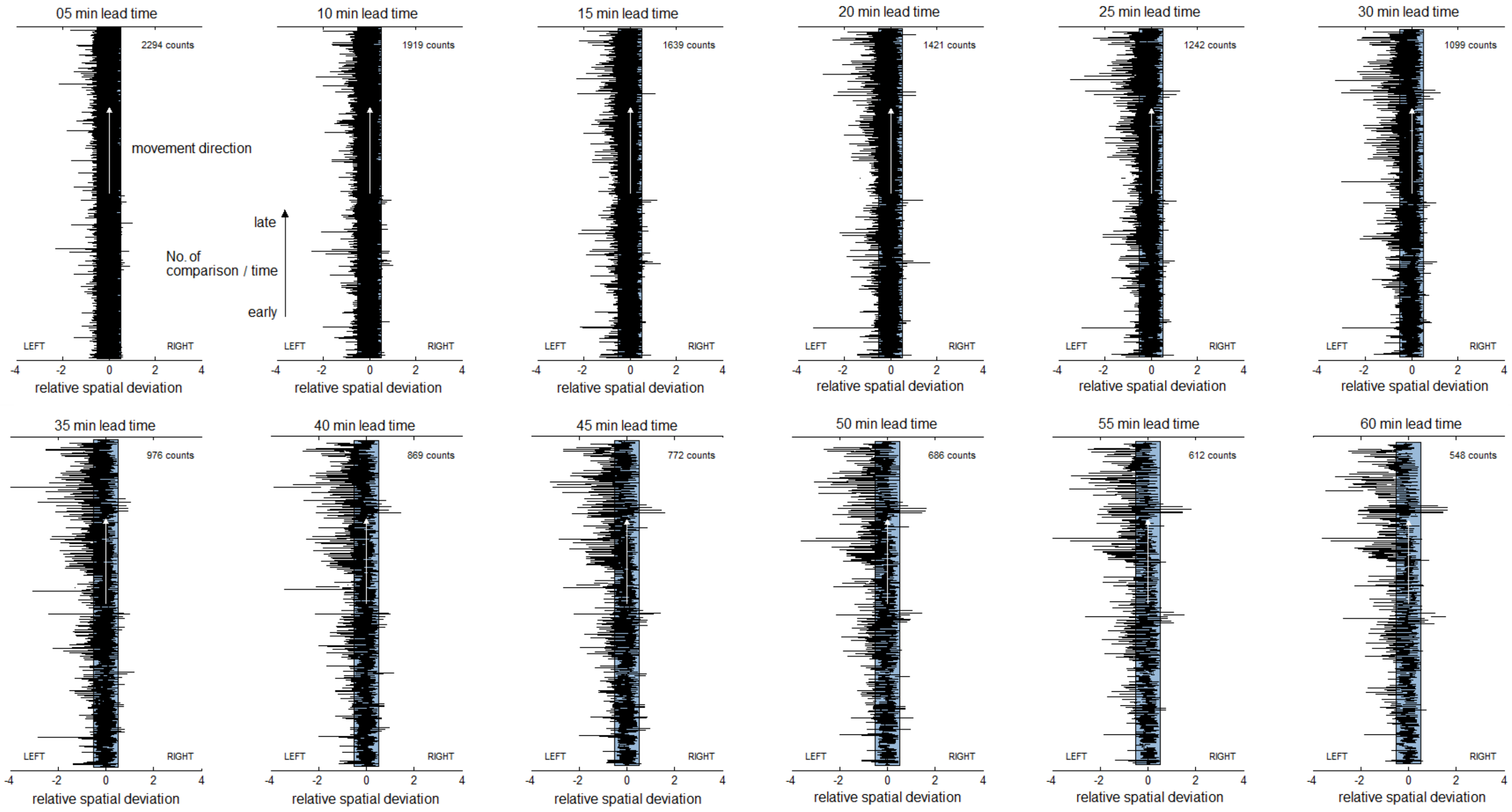

Figure A.7: Uncertainty lateral to movement direction given by extent and location of nowcasted cells (black lines) left and right relative to a standardised cell (blue bar) with width 1. A black line exceeding the blue bar indicates a nowcast that was larger than the actual cell in the respective direction and vice versa. A line that is totally apart the blue bar indicates completely separated cells that do not overlap.

Uncertainty measure application to nowcasted cells

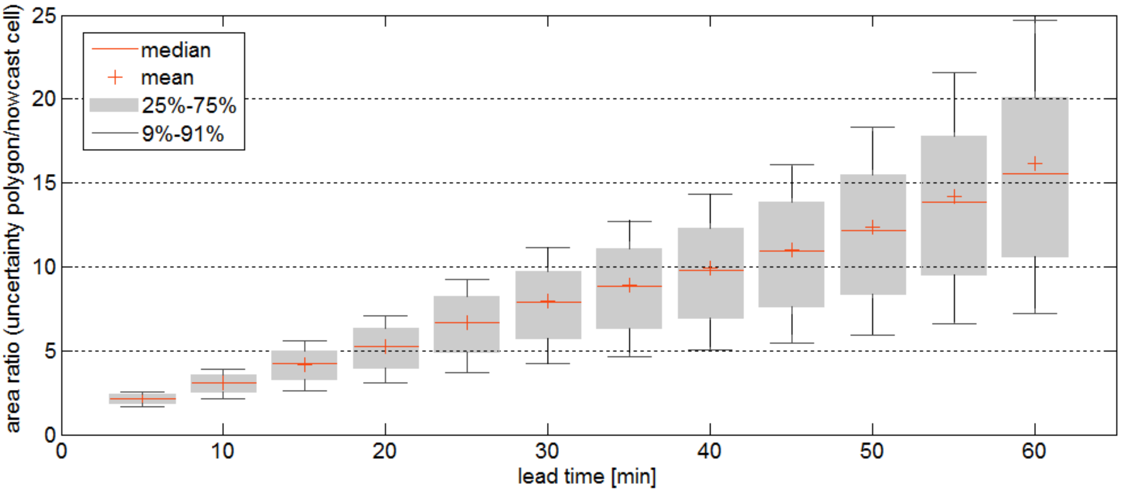

Figure A.8: Box-and-whisker plots of the area enlargement resulting from the application of the 90th percentiles to nowcast cells. The distributions characteristics of all found area ratios of the formed uncertainty polygon and the related cell of the Rad-TRAM nowcast data set of 15 July 2012 are shown for each lead time.

A.3 Simulation evaluation – complementary material

Simulation visualisation

Individual cases

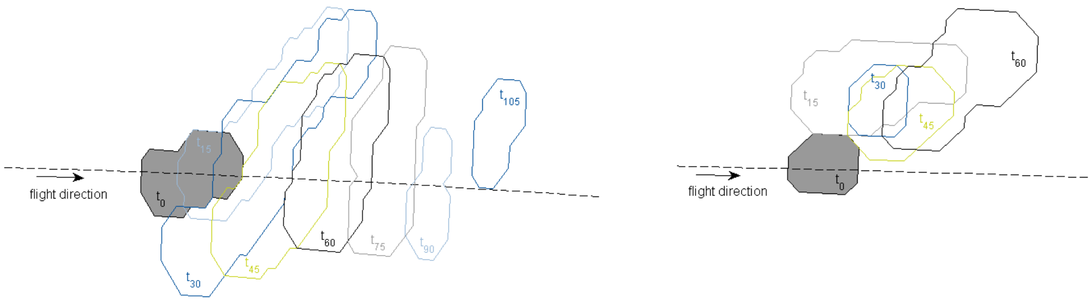

(a) Constant direction movement of cells. (b) Varying direction movement.

Figure A.9: Cell movement direction relative to the planned trajectory which (a) remains about constant during cell development or (b) changes with time.

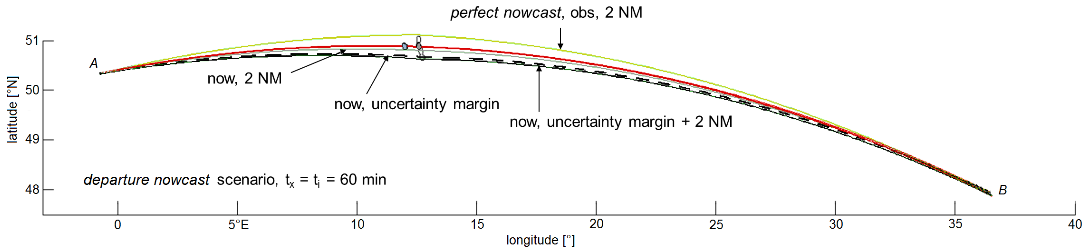

Figure A.10: Sample of the four resulting routes to a weather situation in the *departure nowcast* scenario. The red line represents the planned trajectory which is based on the left weather object (blue). When applying the perfect nowcast (long white object) the diversion leads to the north (green line). The nowcast gives the grey object which is circumnavigated in the south. Three routes emerge due to the application of three different avoidance distances: 2 NM (grey), uncertainty margin (black dashed) and both (black).

All simulated flights

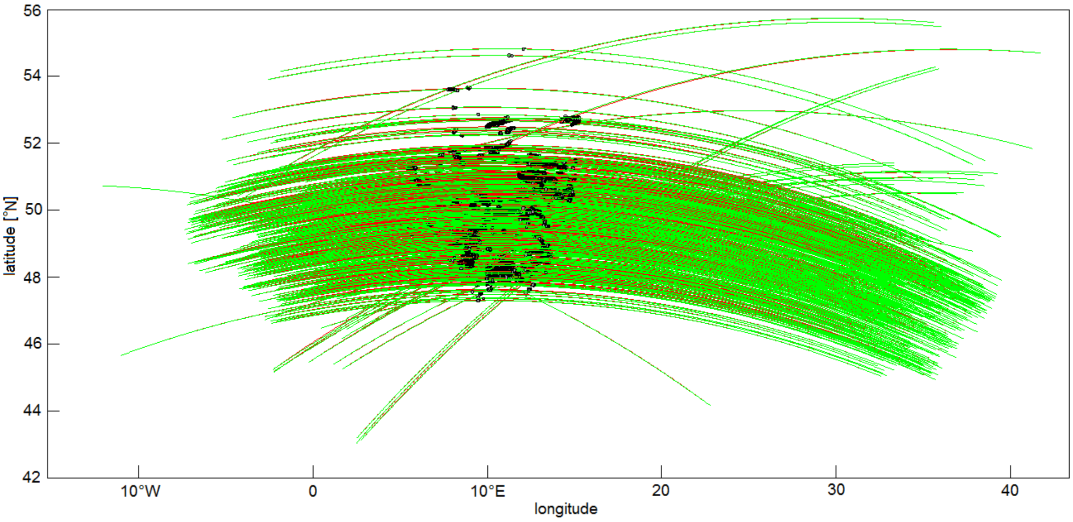

(a) Reference scenario.

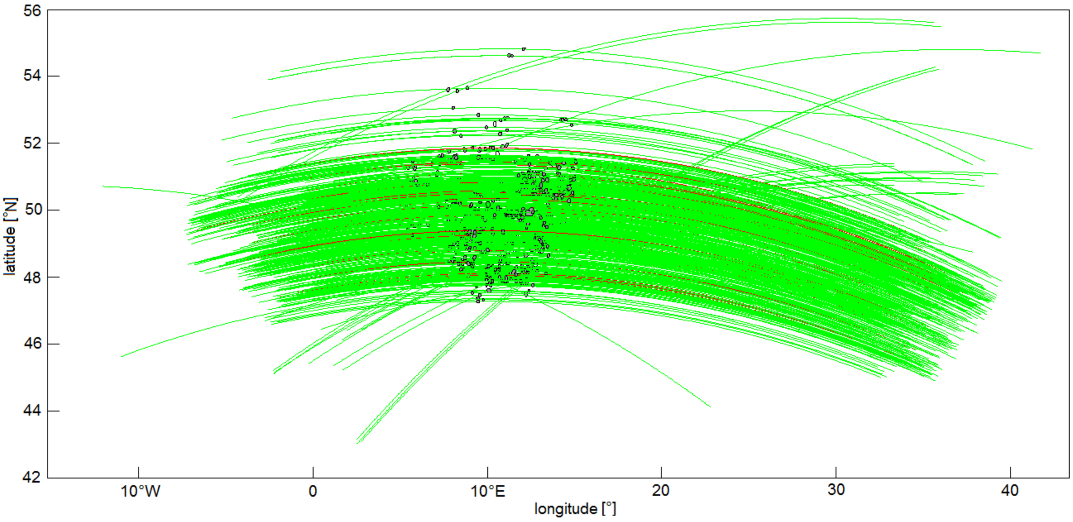

(b) *Perfect nowcast* scenario.

Figure A.11: Exemplary simulation visualisation for *reference* and *perfect nowcast* scenario with observational data. Flown routes are given in green. When these deviate from the planned trajectory, the latter is recognisable in red. The observed cell based on which the planned trajectory is generated is filled (mostly the left one). The main flow is directed from west to east, recognisable by the trajectory lengths in front of (900 km = 60 minutes flight time distance) and behind (2 hours = 1800 km) the initial cell. In (a) all flights deviate instantaneously, adapt their route to the always updated weather situation and eventually optimise their route after cell dissipation. (b) presents the *perfect nowcast* scenario in which the observed cell stage at time t_x is picked from the data set and the final deviation route is determined at departure and executed as such without any updates.

Detours in the *wait and see* scenario

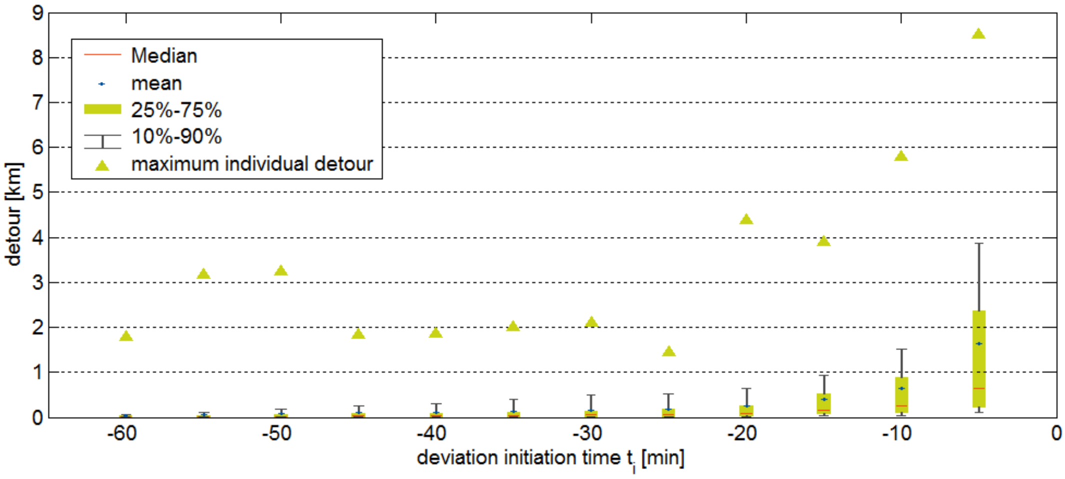

Figure A.12: Box-and-whisker plots summarising the characteristics of the distributions of individual detours obtained by simulations of the *wait and see* scenario.

Detours in the *departure nowcast set* scenario

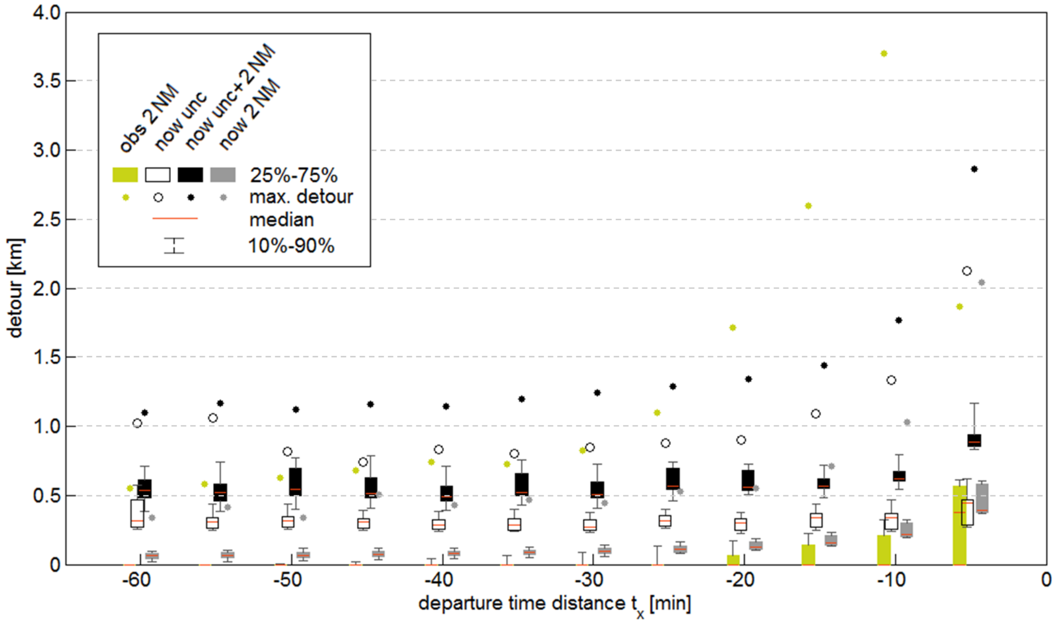

Figure A.13: Range (box-and-whisker plots) and maximum (points) of individual detours obtained by 563 simulations per departure flight time distance t_x between 5 and 60 minutes. Instantaneous proactive re-routing is based on risk areas defined by the latest weather information released at departure time t_0 and valid at time t_x, either as *perfect nowcast* provided by observational data in retrospect or given by the nowcast, both with 2 NM safety distance in green and grey, respectively. Additionally, when applying nowcast data the previously defined uncertainty can be considered, either purely (black) or with the safety distance on top (white).

Bibliography

Airbus, 2007: *Flight Operations Briefing Notes: Adverse Weather Operations – Optimum Use of the Weather Radar*. — Tech. Rep., Airbus Customer Services, Flight Operations Support and Services, Rev. 2, February 2007.

AMS, 2012a: Glossary of Meteorology. – Cloud drop. — *http://glossary.ametsoc.org/wiki/Cloud_drop* – Retrieved: 12.05.2015.

AMS, 2012b: Glossary of Meteorology. – Drizzle. — *http://glossary.ametsoc.org/wiki/Drizzle* – Retrieved: 12.05.2015.

Argüelles, P., M. Bischoff, P. Busquin, B. A. C. Droste, R. Evans, W. Kroll, J.-L. Lagardère, A. Lina, J. Lumsden, D. Ranque, S. Rasmussen, P. Reutlinger, R. Robins, H. Terho, A. Wittlöv, 2001: European Aeronautics: A Vision for 2020. — ACARE, 26 p.

Ashford, N., H. P. M. Stanton, C. A. Moore, 1984: *Airport Operations*. — John Wiley & Sons, Ltd, New York, 476 p.

Bailey, T., D. A. Barnett, M. Barth, W. B. Bendel, S. Douglas, T. Dye, G. Guay, M. Huncik, J. Irwin, D. Katz, S. Kendall, D. Lehrman, C. Lindsey, T. Lockhart, L. Militana, B. B. Murphey, K. L. Schere, N. Seaman, V. Thiermann, S. Vasa, J. White, A. Zak, 2000: Meteorological Monitoring Guidance for Regulatory Modeling Applications.

Bedka, K. M., 2011: Overshooting cloud top detection using MSG SEVIRI Infrared brightness temperatures and their relationship to severe weather over Europe. — *Atmos. Res.*, **99**, **2**, 175 – 189.

BFGoodrich Aerospace, 1997: WX-500 Stormscope: Series II Weather Mapping Sensor – User's Guide. — Rev. A.

Bilimoria, K., B. Sridhar, G. Chatterji, K. Sheth, S. Grabbe, 2001: FACET: Future ATM Concepts Evaluation Tool. — *Air Traffic Control Quarterly*, **9**, **1**, 1 – 20.

Bjerknes, J., 1938: Saturated-adiabatic ascent of air through dry-adiabatically descending environment. — *Q. J. Roy. Meteor. Soc.*, **64**, 325 – 330.

Bjerknes, V., 1904: Das Problem der Wettervorhersage, betrachtet vom Standpunkt der Mechanik und der Physik. — *Meteorol. Z.*, **21**, 1 – 7.

Bluestein, H. B., 2013: *Severe Convective Storms and Tornadoes: Observations and Daynamics*. — Springer-Verlag Berlin.

Boeing, 2011: Statistical summary of commercial jet airplane accidents worldwide operations 1959 – 2010, Aviation safety. — Boeing Inc., 27 p.

Bolić, T., Z. Sivčev, 2011: Eruption of Eyjafjallajökull in Iceland – Experience of European Air Traffic Management. — *Journal of the Transportation Research Board,* **, 2214**, 136 – 143.

Bowler, N., C. Pierce, A. Seed, 2006: STEPS: A probabilistic precipitation forecasting scheme which merges an extrapolation nowcast with downscaled NWP. — *Q. J. Roy. Meteor. Soc.*, **132, 620**, 2127 – 2155.

Brooks, H. E., J. W. Lee, J. P. Craven, 2003: The spatial distribution of severe thunderstorm and tornado environments from global reanalysis data. — *Atmos. Res.*, **67 - 68**, 73 – 94.

Browning, K. A., 1986: Morphology and Classification of Middle-Latitude Thunderstorms. — In: *Thunderstorm Morphology and Dynamics*, E. Kessler, edt., University of Oklahoma Press, Norman, Vol. 2 of *Thunderstorms: A Social, Scientific, and Technological Documentary*, pp. 133 – 152, 2nd ed.

Browning, K. A., F. H. Ludlam, 1960: *Radar Analysis of a Hailstorm.* — Tech. Note No.5, Imperial College of Science and Technology, London, 105 p., 109 p.

Budd, L., T. Ryley, 2012: An International Dimension: Aviation. — In: *Transport and Climate Change*, T. Ryley, L. Chapman, edts., Emerald Group Publishing Limited, Vol. 2 of *Transport and Sustainability*, pp. 35 – 64.

Byers, H. R., J. Braham, R. R., 1949: *The Thunderstorm – Report of the Thunderstorm Project.* — United States Department of Commerce, Weather Bureau, Washington D. C., Available at *babel.hathitrust/cgi/pt?id=uc1.31822010301570;view=1up;seq=5*, Retrieved: 28.10.2015.

Cheung, J., J.-L. Brenguier, J. Heijsteck, A. Marsman, H. Wells, 2014: Sensitivity of Flight Durations to Uncertainties in Numerical Weather Prediction. — In: *Proceedings of the SESAR Innovation Days*, D. Schaefer, edt., Eurocontrol, 8 p.

CoCoRaHS, n. Y.: *Weather Radar Basics.* — Community Collaborative Rain, Hail & Snow Network, *www.cocorahs.org/media/docs/radar_basics.pdf* – Retrieved: 15.05.2015.

Coiffier, J., 2011: *Fundamentals of Numerical Weather Prediction.* — Cambridge University Press.

ComplexWorld Network, 2014: ComplexWorld Position Paper. — Available at *http://complexworld.eu/wiki/Uncertainty_in_ATM#Definitions*, Retrieved: 27.08.2015.

Correll, N., 2014: *Introduction to Autonomous Robots.* — CreateSpace Independent Publishing Platform, first Ed.

Craig, G. C., 2012: Probabilistic Weather Forecasting. — In: *Atmospheric Physics, Research Topics in Aerospace*, U. Schumann, edt., Springer-Verlag, Heidelberg, pp. 661 – 673.

Davies-Jones, R., 2002: Linear and Nonlinear Propagation of Supercell Storms. — *J. Atmos. Sci.*, **59**, 3178 – 3205.

Davis, C. A., B. G. Brown, R. Bullock, J. Halley-Gotway, 2009: The Method for Object-Based Diagnostic Evaluation (MODE) Applied to Numerical Forecasts from the 2005 NSSL/SPC Spring Program. — *Wea. Forecasting*, **24, 5**, 1252 – 1267.

DeLaura, R., J. Evans, 2006: An Exploratory Study of Modeling Enroute Pilot Convective Storm Flight Deviation Behavior. — In: *12th Conference on Aviation, Range, and Aerospace Meteorology (ARAM)*, AMS, Atlanta, GA/USA.

Dixon, M., G. Wiener, 1993: TITAN: Thunderstorm Identification, Tracking, Analysis, and Nowcasting – A Radar-based Methodology. — *J. Atmos. Oceanic Technol.*, **10, 6**, 785 – 797.

DLR, n. Y.: DLR Rad-TRAM (Radar Tracking and Monitoring).

Doswell, C., 1985: The operational meteorology of convective weather. Vol. 2: Storm scale analysis. — NOAA Tech. Memo. ERL ESG-15.

Doswell, C., edt., **2001:** *Severe Convective Storms*, Vol. 28 of *Meteorological Monographs*, Boston, American Meteorological Society, pp. 561.

Douglas, R. D., 1990: The Stromy Weather Group (Canada). — In: *Radar in Meteorology*, D. Atlas, edt., Amer. Met. Soc., pp. 61 – 68.

Dougui, N. E., D. Delahaye, S. Puechmorel, M. Mongeau, 2011: Light Propagation algorithm for aircraft trajectory planning. — In: *American Control Conference*, San Francisco, CO/USA, pp. 2143 – 2147.

Drosdowsky, W., H. Zhang, 2003: Verification of Spatial Fields. — In: *Forecast Verification: A Practioner's Guide in Atmospheric Science*, I. T. Jolliffe, D. B. Stephenson, edts., John Wiley & Sons, Ltd, pp. 121 – 136.

DWD, 2011: Der Radarverbund des Deutschen Wetterdienstes.

DWD, 2012: COSMO-DE (früher LMK). — *http://www.dwd.de/bvbw/appmanager/bvbw/dwdwwwDesktop?_nfpb=true&_pageLabel=_dwdwww_aufgabenspektrum_vorhersagedienst&T186093184011521647016 85gsbDocumentPath=Navigation%2FOeffentlichkeit%2FAufgabenspektrum%2FNumerische__Modellierung%2FAS__NM__LMK__node.html%3F__nnn%3Dtrue*, Retrieved: 27.08.2015.

DWD, 2014: Zellerkennung und -Prognose (CellMOS). — *http://www.dwd.de/DE/forschung/wettervorhersage/met_fachverfahren/nowcasting/cellmos_cverfahren.html?nn=19768.html*, Retrieved: 28.10.2015.

DWD, 2015a: Regionalmodell COSMO-DE. — *http://www.dwd.de/DE/forschung/wettervorhersage/num_modellierung/01_num_vorhersagemodelle/regionalmodell_cosmo_de.html?nn=512942*, Retrieved: 05.11.2015.

DWD, 2015b: Weather Forecast Models. — *http://www.dwd.de/bvbw/appmanager/bvbw/dwdwwwDesktop?_nfpb=true&_pageLabel=dwdwww_result_page&portletMasterPortlet_i1gsbDocumentPath=Navigation %2FOeffentlichkeit%2FAufgabenspektrum%2FNumerische__Modellierung%2FAS__NM__intro__node.html%3F __nnn%3Dtrue*, Retrieved: 05.09.2015.

DWD, n. Y.: DWD Weather Radar Network.

Ebert, E. E., J. L. McBride, 2000: Verifcation of precipitation in weather systems: determination of systematic errors. — *J. Hydrol.*, **239**, 179 – 202.

Etling, D., 2008: *Theoretische Meteorologie.* — Springer-Verlag, Berlin, third Ed.

Eurocontrol, 2009: MET support to ATM. — In: *Aviation Meteorology (MET) Workshop No. 1*, Brussels, Belgium.,

Eurocontrol, 2013: Performance Review Report – An Assessment of Air Traffic Management in Europe during the Calendar Year 2012. — European Organisation for the Safety of Air Navigation, 137 p.

Eurocontrol, 2014: Performance Review Report – An assessment of Air Traffic Management in Europe during the calendar year 2013. — European Organisation for the Safety of Air Navigation, 141 p.

Eurocontrol, 2015: Base of Aircraft Data (BADA). — *https://www.eurocontrol.int/services/bada*, Retrieved: 29.08.2015.

FAA, 1983: Advisory Circular – Thunderstorms. AC No. 00-24B. — Federal Aviation Administration.

FAA, 2010: Weather-related aviation accident study 2003 – 2007. — Federal Aviation Administration, 71 p.

FAA, 2015: NextGen Weather – FAQ: Weather Delay. — *http://www.faa.gov/nextgen /programs/weather/faq/*, Retrieved: 26.08.2015.

Feynman, R., R. Leighton, M. Sands, 2013: *The Feynman Lectures on Physics – Volume I: Mainly Mechanics, Radiation, and Heat.* — Basic Books, eBook version available at *http://www.feynmanlectures.caltech.edu/I_toc.html*, Retrieved: 28.10.2015.

Forster, C., 2015: Personal contact on 02.11.2015.

Forster, C., A. Tafferner, 2012: Nowcasting Thunderstorms for Munich Airport. — In: *The DLR Project Wetter und Fliegen*, T. Gerz, C. Schwarz, edts., Deutsches Zentrum für Luft- und Raumfahrt, pp. 32 – 45, Forschungsbericht 2012-2.

Garz, S., 2012: "Wetter und Fliegen" – Summer Campaign 2012. — *www.pa.op.dlr.de/MUCSOMMER/2012*, Rerieved: 24.09.2015.

Gates, E. S., 1979: *Meteorology and Climatology for Sixth Forms and Beyond*. — Harrap, London, UK, 295 p.

Geçer, C., 2005: *Training Course on Weather Radar Systems – Module D: Radar Products and Operational Applications*. — Turkish State Meteorological Service, WMO, CIMO, Antalya, Turkey.

Georgii, W., 1927: *Flugmeteorologie*. — Akademische Verlagsgesellschaft M. B. H.

Gerz, T., 2014: Mitigating the impact of weather hazards on aviation. — In: *World Weather Open Science Conference*, Montréal, Canada.,

Gerz, T., C. Forster, A. Tafferner, 2012: *Atmospheric Physics*, Springer-Verlag, Heidelberg, Chap. Mitigating the Impact of Adverse Weather on Aviation. — pp. 645 – 658.

Gilleland, E., D. Ahijevych, B. G. Brown, R. Bullock, C. Davis, J. Halley-Gotway, L. Holland, 2007: Method for Object-based Diagnostic Evaluation (MODE). — Seminar, October 2007.

Gilleland, E., D. Ahijevych, B. G. Brown, E. E. Ebert, 2009: Intercomparison of spatial forecast verification methods. — *Wea. Forecasting*, **24, 5**, 1416 – 1430.

Glahn, H., D. Lowry, 1972: The use of model output statistics (MOS) in objective weather forecasting. — *J. Appl. Meteor.*, **11, 8**, 1203 – 1211.

Gräupl, T., B. Jandl, C.-H. Rokitansky, 2012: Simple and Efficient Integration of Aeronautical Support Tools for Human-In-the-Loop Evaluations. — In: *Proceedings of Integrated Communications Navigation and Surveillance Conference*, Herndon, VA/USA, pp. F4–1 – F4–9.

Hand, W. H., 1996: An object-oriented technique for nowcasting heavy showers and thunderstorms. — *Meteorol. Appl.*, **3**, 31 – 41.

Hauf, T., P. Hupe, M. Sauer, C.-H. Rokitansky, M. Kerschbaum, 2015: *Final Summary on the MET4ATM Project*. — Berichte des Instituts für Meteorologie und Kimatologie der Leibniz Universität Hannover, Band 79, Selbstverlag des Instituts für Meteorologie und Klimatologie.

Hauf, T., H. Leykauf, U. Schumann, 2004: *Luftverkehr und Wetter – Statuspapier 2004*. — No. Mitteilung 2004-02, Deutsches Zentrum für Luft- und Raumfahrt, 59 p.

Hauf, T., L. Sakiew, M. Sauer, 2013: Adverse weather diversion model DIVMET. — *Journal of Aerospace Operations*, **2, 3 - 4**, 115 – 133.

Heise, E., 2002: Parametrisierungen. — *Promet*, **27, 3/4**, 130 – 141.

Higdon, D., 2008 - 09: A Buyer's Guide: Weather Detection & Avoidance – Wx Worries? Several Sources Offer Graphic Help. — *Pilot's Guide to Avionics*, 36 – 42.

Hoffmann, J. M., 2008: *Entwicklung und Anwendung von statistischen Vorhersage-Interpretationsverfahren für Gewitternowcasting und Unwetterwarnungen unter Einbeziehung von Fernerkundungsdaten.* — PhD thesis, FU Berlin, Germany, 205 p.

Honeywell, 2006: *Honeywell Primus 880 Digital Weather Radar System – Pilot's Guide.* — Honeywell International Inc. Commercial Electronic Systems, Glendale, AZ/USA, Pub. No. A28-1146-102-03, 1996, revised January 2006.

Hupe, P., 2015: *Simulation und Analyse des Flugverkehrs im Fall eines Squall-Line-Ereignisses über Österreich – Untersuchungen zur Vorhersagbarkeit der wetterbedingten Verschiebung von Sektorbelastungen.* — Bachelor thesis, Leibniz Universität Hannover, Germany, 104 p.

Hupe, P., T. Hauf, C.-H. Rokitansky, 2014: Case Study of Adverse Weather Avoidance Modelling. — In: *Proceedings of the SESAR Innovation Days*, D. Schaefer, edt., Eurocontrol, 7 p.

Hwang, Y., A. J. Clark, V. Lakshmanah, S. E. Koch, 2015: Improved Nowcasts by Blending Extrapolation and Model Forecasts. — *Wea. Forecasting*, **30, 5**, 1201 – 1217.

Israël, H., 1964: *Probleme der Gewitterforschung: 1. Das Gewitter in heutiger Sicht.* — Forschungsberichte des Landes Nordrhein-Westfalen No. 1408, Köln.

Jarque, C. M., A. K. Bera, 1987: A test for normality of observations an regression residuals. — *International Statistical Review*, **55, 2**, 163 – 172.

Jolliffe, I. T., D. B. Stephenson, 2003: *Forecast Verification – A Practioner's Gude in Atmospheric Science.* — John Wiley & Sons, Ltd.

Jones, D. M. A., 1956: Raindrop Size Distribution and Radar Reflectivity. — *Illinois State Water Survey, Research Report No. 8.*

Joss, J., J. C. Thams, A. Waldvogel, 1970: The Variation of Raindrop Size Distribution at Locarno. — *Wissenschaftliche Mitteilungen der Eidgenössischen Kommission zum Studium der Hagelbildung und der Hagelabwehr*, , **64**, Zurich, Switzerland.

Keil, C., G. C. Craig, 2009: A Displacement and Amplitude Score Employing an Optical Flow Technique. — *Wea. Forecasting*, **24, 5**, 1297 – 1308.

Klingle-Wilson, D., J. Evans, 2005: *Description of the Corridor Integrated Weather System (CIWS) Weather Products.* — MIT Lincoln Laboratory, Lexington, MA/USA, Project Report ATC-317.

Kober, K., 2006: *Verfolgung von Gewitterzellen mittels Fernerkundungsdaten von Radar und Satellit.* — Diploma thesis, Ludwig-Maximilians-Universität München, Germany, 81 p.

Kober, K., G. C. Craig, C. Keil, A. Dörnbrack, 2012: Blending a probabilistic nowcasting method with a high-resolution numerical weather prediction ensemble for convective precipitation forecasts. — *Q. J. Roy. Meteor. Soc.*, **138**, 755 – 768.

Kober, K., A. Tafferner, 2009: Tracking and nowcasting of convective cells using remote sensing data from radar and satellite. — *Meteorol. Z.*, **1, 18**, 75 – 84.

Kroese, D. P., T. Brereton, T. Taimre, Z. I. Botev, 2014: Why the Monte Carlo method is so important today. — *WIREs Comput. Stat.*, **6**, 386 – 392.

Kulesa, G., 2002: Weather and aviation: How does weather affect the safety and operations of airport and aviation, and how does FAA work to manage weather-related effects? — In: *The Potential Impacts of Climate Change on Transportation Workshop*, Washington, D.C., Washington, D.C./USA.

Lankford, T. T., 2000: *Aviation weather handbook.* — McGraw-Hill Companies, first Ed.

Lau, A., 2012: Econiomic Assessment of Enhanced Information on Convective Weather. — In: *The DLR Project Wetter und Fliegen*, T. Gerz, C. Schwarz, edts., Deutsches Zentrum für Luft- und Raumfahrt, pp. 107 – 116, Forschungsbericht 2012-02.

Li, P. W., W. K. Wong, K. Y. Chan, E. S. T. Lai, 2000: SWIRLS – An Evolving Nowcasting System. — Hong Kong Observatory, Technical Note No. 100.

Luchkova, T., R. Vujasinovic, A. Lau, M. Schultz, 2015: Analysis of Impacts an Eruption of Volcano Stromboli could have on European Air Traffic. — *Eleventh USA/Europe Air Traffic Management Research and Development Seminar (ATM2015)*, 7 p.

Manzato, A., G. J. Morgan, 2003: Evaluating the sounding instability with the Lifted Parcel Theory. — *Atmos. Res.*, **67 - 68**, 455 – 473.

Markovic, D., U. Spehr, T. Hauf, 2008: A statistical study of the weather impact on punctuality at Frankfurt Airport, Germany. — *Meteorol. Appl.*, **15, 2**, 293 – 303.

Markowski, P., Y. Richardson, 2010: *Mesoscale Meteorology in Midlatitudes.* — John Wiley & Sons, Ltd, 407 p.

Marwitz, J. D., 1972: The structure and motion of severe hailstorms. Part 2: Multicell storms. — *J. Appl. Meteorol.*, **11, 1**, 180 – 188.

Matthews, M., R. DeLaura, 2010: Assessment and Interpretation of En Route Weather Avoidance Fields from the Convective Weather Avoidance Model. — In: *10th AIAA Aviation Technology, Integration, and Operations Conference*, MIT Lincoln Laboratory, Fort Worth, TX/USA, 19 p., Fort Worth, TX/USA.

Maularie, W. M., 2000: *Department of Defense World Geodetic System 1984 – Its Definition and Relationships with Local Geodetic Systems.* — Tech. Rep. 8350.2, National Imagery and Mapping Agency, third Ed.

Mazalevskis, M., T. Zinner, A. Los, 2013: Minutes-ahead solar resource forecasting based on sky camera imagery. — In: *Presentation held on Fachtagung Energiemeteorologie*, Grainau, Germany, *http://googl/Drg2nZ*, Retrieved: 03.09.2015.

McNally, D., K. Sheth, C. Gong, J. Love, C. H. Lee, S. Sahlman, J.-H. Cheng, 2012: Dynamic Weather Routes: A Weather Avoidance System for near-term Trajectory-based Operations. — In: *28th International Congress of the Aeronautical Sciences*, 18 p., Brisbane, Australia.

McNally, D., K. Sheth, C. Gong, M. Sterenchuk, S. Sahlman, S. Hinton, C. Lee, F.-T. Shih, 2015: Dynamic Weather Routes: Two Years of Operational Testing at American Airlines. — In: *Eleventh USA/Europe Air Traffic Management Research and Development Seminar (ATM2015)*, 10 p., Lisbon, Portugal.

Mirza, K., A. C. Pagé, S. Geindre, 2008: FLYSAFE – an approach to safety – unsing GML/XML objects to define hazardous volumes of aviation space. — In: *13th Conference on Aviation, Range and Aerospace Meteorology, AMS*, New Orleans, LA/USA.,

Mooney, C. Z., 1997: *Monte Carlo Simulation.* — No. 07-116 in Sage University Paper series on Quantitative Applications in the Social Sciences, Sage Publications, Thoussand Oaks, CA/USA.

NATS, 2010: *The effect of thunderstorms and associated turbulence on aircraft operations – Technical Note AIC: P 056/2010.* — Aeronautical Information Service, Hounslow, Middlesex, UK, pp. 10.

Pearson, K., 1905: The Problem of the Random Walk. — *Nature*, **72, 1865**, 294 p.

Pierce, C., P. J. Hardaker, C. G. Collier, C. M. Haggett, 2000: GANDOLF: a system for generating automated nowcasts of convective precipitation. — *Meteorol. Appl.*, **7**, 341 – 360.

Pinto, J., W. Dupree, S. Weygandt, M. Wolfson, S. Benjamin, M. Steiner, 2010: Advances in the Consolidated Strom Prediction for Aviation (CoSPA). — In: *14th Conference on Aviation, Range and Aerospace Meteorology, AMS*, Atlanta, GA/USA., January.

Rauber, R. M., J. E. Walsh, D. J. Charlevoix, 2005: *Severe and Hazardous Weather – An Introduction to High Impact Meteorology.* — Kendall/Hunt, Dubuque, IA/USA, second Ed.

Rippel, E., A. Bar-Gill, N. Shimkin, 2005: Fast Graph-Search Algorithms for General-Aviation Flight Trajectory Generation. — *J. Guid. Control. Dynam.*, **28, 4**, 801 – 811.

Rokitansky, C.-H., 2009: NAVSIM: Detailgenaue Simulation des heutigen/zukünftigen Flugverkehrs (Europa/weltweit) zur Bewertung von SESAR Konzepten und Wetterszenarien. — Presentation. Stuttgart, Germany, 16 January.

Romero, R., M. Gayà, C. A. Doswell, 2007: European climatology of severe convective storm environmental parameters: A test for significant tornado events. — *Atmospheric Research*, **83, 2-4**, 389 – 404.

Sauer, M., C. Forster, T. Hauf, 2015a**:** The Uncertainty of Thunderstorm Nowcasting and its Use in Weather Avoidance Modeling. — In: *17th Conference on Aviation, Range and Aerospace Meteorology*, AMS, Phoenix, AZ/USA.,

Sauer, M., T. Hauf, C. Forster, 2014: Uncertainty Analysis of Thunderstorm Nowcasts for Utilization in Aircraft Routing. — In: *Proceedings of the SESAR Innovation Days*, D. Schaefer, edt., Eurocontrol, 8 p.

Sauer, M., T. Hauf, L. Sakiew, P. W. Chan, S.-M. Tse, P. Hupe, 2015b**:** On the Identification of Weather Avoidance Routes in the TMA of Hong Kong International Airport. — Accepted by *Journal of Zhejiang University. Science. A.*

Sauer, M., P. Hupe, L. Sakiew, T. Hauf, C.-H. Rokitansky, M. Kerschbaum, 2013: Sector Occupancy Analysis with the Adverse Weather Diversion Model DIVMET. — In: *16th Conference on Aviation, Range and Aerospace Meteorology*, AMS, Austin, TX/USA., Vol. 16th,

Scharf, K., 2013: Implementation of Rad-TRAM Nowcast Data in the Adverse Weather Diversion Model DIVMET. — Bachelor thesis, Leibniz Universität Hannover, Germany, 33 p.

Schmetz, J., P. Pili, S. Tjemkes, D. Just, J. Kerkmann, S. Rota, A. Ratier, 2002: An Introduction to Meteosat Second Generation (MSG). — *Bull. Amer. Meteor. Soc.*, **83**, 977 – 992.

SESAR Joint Undertaking, 2012: The Roadmap for Sustainable Air Traffic Management – European ATM Master Plan. — European Union and Eurocontrol, 2nd ed., 100 p.

SESAR Joint Undertaking, 2014: SESAR Demonstration Initial 4D trajectory. — European Union and Eurocontrol, 8 p.

SKYbrary Aviation Safety, 2013: Weather Radar: Storm Avoidance. — *http://www.skybrary.aero/index.php/Weather_Radar:_Storm_Avoidance*, Retrieved: 04.05.2015.

Spitzer, F., 1976: *Principles of Random Walk*, Vol. 34 of *Graduate Texts in Mathematics*. — Springer-Verlag, New York, second Ed.

Sridhar, B., K. Sheth, P. Smith, W. Leber, 2005: Migration of FACET from Simulation Environment to Dispatcher Decision Support System. — In: *Proceedings of 24th Digital Avionics Systems Conference*, Washington, D. C./USA, 30 October - 03 November.

Statistische Ämter des Bundes und der Länder, 2015: Gebiet und Bevölkerung – Fläche und Bevölkerung. — *http://www.statistik-portal.de/statistik-portal/de_jb01_jahrtab1.asp*, Retrieved: 15.10.2015.

Stich, D., 2012: *Convection Initiation – Detection and Nowcasting with multiple data sources.* — PhD thesis, Ludwig-Maximilians-Universität München, Germany, 131 p.

Stich, D., C. Forster, A. Tafferner, M. Köhler, I. Sölch, T. Gerz, 2013: Information on thunderstorm initiation, nowcast and forecast for aviation safety and efficiency. — 1st ECATS Conference on technical challenges for aviation in a changing environment, Berlin, Germany.

Tafferner, A., C. Forster, 2012: Weather Nowcasting and Short Term Forecasting. — In: *Atmospheric Physics – Research Topics in Aerospace*, U. Schumann, edt., Springer-Verlag, Berlin, pp. 363 – 380.

The COMET Program, 2015: Tropical Cyclone Forecast Uncertainty. — Available at *https://www.meted.ucar.edu/training_module.php?id=1191#.VjKCmCsXt-k*, Retrieved: 29.10.2015.

Trammell, A., 2010: The Mysterious 'Gain' Knob. — *Business & Commercial Aviation*, 58 – 60.

University of Wyoming, 2012: Soundings. — *http://weather.uwyo.edu/upperair/sounding.html*, Retrieved: 13.09.2015.

University of Wyoming, n.Y.: Sounding Station Parameters and Indices. — *http://weather.uwyo.edu/upperair/indices.html*, Retrieved: 13.09.2015.

Weisman, M. L., R. Rotunno, 2000: The Use of Vertical Wind Shear versus Helicity in Interpreting Supercell Dynamics. — *J. Atmos. Sci.*, **57**, 1452 – 1472.

Wilks, D. S., 2011: *Statistical methods in the atmospheric sciences*, Vol. 100 of *International Geophysics Series*. — Elsevier, third Ed.

Wilson, J. W., N. A. Crook, C. K. Mueller, J. Sun, M. Dixon, 1998: Nowcasting Thunderstorms: A Status Report. — *Bull. Amer. Meteor. Soc.*, **79**, 2079 – 2099.

WMO, 2012: *Guidelines on Ensemble Prediction Systems and Forecasting*. — World Meteorological Organization, WMO-No. 1091.

WMO, 2015: Nowcasting. — *https://www.wmo.int/pages/prog/amp/pwsp/Nowcasting.htm*, Retrieved: 02.09.2015.

Wolfson, M. M., W. J. Dupree, R. M. Rasmussen, M. Steiner, S. G. Benjamin, S. S. Weygandt, 2008: Consolidated storm prediction for aviation (CoSPA). — In: *Integrated Communications, Navigation and Surveillance Conference (ICNS)*, pp. 1 – 19, Bethesda, MD/USA.

Zimmer, M., G. C. Craig, C. Keil, H. Wernli, 2011: Classification of precipitation events with a convective response timescale and their forecasting characteristic. — *Geophys. Res. Lett.*, **38**, 6 p.

Zinner, T., H.-D. Betz, 2009: Validation of Meteosat Storm Detection and Nowcasting Based on Lightning Network Data. — In: *EUMETSAT Meteorological Satellite Conference*, Bath, UK.25 September.

Zinner, T., P. Groenemeijer, 2012: Thunderstorms: Thermodynamics and Organization. — In: *Atmospheric Physics – Research Topics in Aerospace*, U. Schumann, edt., Springer-Verlag Berlin, pp. 101 – 114.

Zinner, T., H. Mannstein, A. Tafferner, 2008: Cb-TRAM: Tracking and monitoring severe convection from onset over rapid development to mature phase using multi-channel Meteosat-8 SEVIRI data. — *Meteorol. Atmos. Phys.*, **101**, 191 – 210.

Acknowledgements

The present thesis and related studies were performed under supervision of Prof. Dr. Thomas Hauf, whom I like to thank very much. His professional guidance and readiness for scientific discussions was outstanding. I also acknowledge Prof. Dr. Dieter Etling for acting as co-referee.

I like to thank all those responsible in SESAR's WP-E ComplexWorld PhD programme – for funding this PhD and also for establishing the network. The provided opportunity to attend a lot of meetings and conferences enabled to get in touch with experts in the wide range of aviation applications and triggered discussions as well as new ideas how to orientate the own research.

Special acknowledgement goes to Marc Bourgois at EUROCONTROL for having reviewed all my deliverables and giving supportive feedback throughout the years. I also thank Alexander Heidt, Soufiane Bouarfa, Nataliya Mogles and Pablo Fleurquin for the enjoyable time around the meetings.

I thank Caroline Forster and her colleagues at DLR Oberpfaffenhofen and WxFUSION for provision of a Rad-TRAM data set and their responsiveness for supportive information.

Special thanks are addressed to the present and former colleagues and final year students in our group at IMUK – especially to Ludmila Sakiew for having forwarded the DIVMET development to me while remaining a supportive contact whenever a question arised.

In this context I also acknowledge Patrick Hupe, Alina Fiehn and Katrin Scharf for their great support in making good progress on the further development of DIVMET by having implemented whole sections of new features.

I acknowledge the many hours that Rick Austin, Patrick Hupe and Kevin Borck spent in careful reading of this manuscript. Thanks also to Henrike Gümmer for reading it in parts.

Finally, I like to thank my family and especially Kevin Borck who supported me throughout the whole studies and kept me up the last weeks. Thank you. ♡

Curriculum Vitae

PERSONAL DETAILS

Name:	Manuela Sauer
Date of Birth	27 December 1986
Place of Birth	Hannover, Germany
Marital Status	unmarried

ACADEMIC CAREER

01/2012 - 09/2015	Research associate at Institute of Meteorology and Climatology, Leibniz Universität Hannover, Germany, under auspices of the SESAR WP-E research network ComplexWorld and co-financed by Eurocontrol on behalf of the SESAR Joint Undertaking

POSTGRADUATE STUDIES

since 2012	PhD student at Leibniz Universität Hannover, Germany
10/2010 - 11/2011	Master thesis: *Konzeption zur Implementierung winterlicher Wetterereignisse in Schnellzeitsimulationsmodelle des Luftverkehrs* at German Aerospace Center (DLR) in Brunswick, Germany
10/2009 - 11/2011	M. Sc. Meteorology at Leibniz Universität Hannover, Germany

UNDERGRADUATE STUDIES

2009	Bachelor thesis: *Analyse regionaler Klimaszenarien für Niedersachsen*
10/2006 - 09/2009	B. Sc. Meteorology at Leibniz Universität Hannover, Germany

Publications

Sauer, M., T. Hauf, L. Sakiew, P.W. Chan, S.-M. Tse, P. Hupe, 2015: On the Identification of Weather Avoidance Routes in the TMA of Hong Kong International Airport. – Accepted by *Journal of Zhejiang University – Science A*

Hauf, T., P. Hupe, M. Sauer, C.-H. Rokitansky, M. Kerschbaum, 2015: *Final Summary on the MET4ATM Project.* — Berichte des Instituts für Meteorologie und Klimatologie der Leibniz Universität Hannover, Band 79, Selbstverlag des Instituts für Meteorologie und Klimatologie, 121 p. – ISBN 3-923624-53-0

Sauer, M., T. Hauf, C. Forster, 2014: Uncertainty Analysis of Thunderstorm Nowcasts for Utilization in Aircraft Routing. — In: *Proceedings of the SESAR Innovation Days*, Schaefer, D. (Editor), EUROCONTROL, 8 p. – ISBN 978-2-87497-077-1

Sauer, M., T. Gerz, 2014: Wettereinfluss auf Sicherheit und Effzienz im Luftverkehr – Analysen und Miniierungskonzepte, pro*met* Meteorologische Fortbildung, Jahrg. 38, Nr. 3/4, pp. 157 - 165.

Hauf, T., L. Sakiew, M. Sauer, 2013: Adverse weather diversion model DIVMET. *Journal of Aerospace Operations* **2**, pp. 115 - 133. – DOI 10.3233/AOP-130037

Conference Contributions

Sauer, M., C. Forster, T. Hauf, 2015: The Uncertainty of Thunderstorm Nowcasting and its Use in Weather Avoidance Modeling. *95th AMS Annual Meeting, 17th Conference on Aviation, Range, and Aerospace Meteorology (ARAM)*, Phoenix, AZ/USA.

Hupe, P., T. Hauf, M. Sauer, C.-H. Rokitansky, J. Lang, 2014: Real-time Flugverkehrssimulation der Gewitterumfliegung basierend auf dem Wetterausweichmodell DIVMET und dem Luftverkehrsmodell NAVSIM, *Sitzung 2/2014 der DGON – Luftfahrtkommission, Thema "Flugmeteorologie"*, Offenbach, Germany.

Sauer, M., L. Sakiew, A. Fiehn, T. Hauf, C.-H. Rokitansky, M. Kerschbaum, 2013: Simulation des Ausweichverhaltens von Flugzeugen in Schlechtwettersituationen mit DIVMET – Anwendung auf ein Squall Line Ereignis über Österreich. *DACH Meteorologentagung 2013*, Innsbruck, Austria.

Sauer, M., L. Sakiew, T. Hauf, P. Hupe, 2013: Some applications of the adverse weather diversion model DIVMET. *93th AMS Annual Meeting, 16th ARAM*, Austin, TX/USA, 9 p.

Sauer, M., L. Sakiew, T. Hauf, P. Hupe, 2013: The Adverse Weather Diversion Model DIVMET – Concept and Applications. *93th AMS Annual Meeting, 16th ARAM*, Austin, TX/USA.

Sauer, M., P. Hupe, L. Sakiew, T. Hauf, C.-H. Rokitansky, M. Kerschbaum, 2013: Sector Occupancy Analysis with the Adverse Weather Diversion Model DIVMET. *93th AMS Annual Meeting, 16th ARAM*, Austin, TX/USA.

Sauer, M., Sakiew, L., Hupe, P., 2013: Studie mit DIVMET zur Sektorbelastung bei Gewittern, *DFS – 10. Nutzerkonferenz Wetterdaten*, Langen, Germany.

Sauer, M., T. Hauf, 2013: Intelligent Modeling the Impact of Unpredictable Adverse Weather on ATM Performance, ComplexWorld Workshop 1 "Uncertainty in ATM", Naples, Italy.

Sauer, M., L. Sakiew, P. Hupe, 2012: A theoretical sector capacity analysis with DIVMET, *2nd SESAR Innovation Days*, Braunschweig, Germany.

Sauer, M., L. Sakiew, T. Hauf, P. Hupe, J. Siedler, 2012: Intelligent Modeling the Impact of Unpredictable Adverse Weather on ATM Performance, Poster, *2nd SESAR Innovation Days*, Braunschweig, Germany.

Schneider, O., M. Sauer, 2012: Integration of Winter Weather in Simmod *PRO!. European Simmod User Group (ESUG) Meeting*, München, Germany.

Sauer, M., L. Sakiew, T. Hauf, 2011: Intelligent Modeling the Impact of Unpredictable Adverse Weather on ATM Performance, Poster, *1st SESAR Innovation Days*, Toulouse, France.